

DYNAMIC MODELLING, IDENTIFICATION AND SIMULATION OF INDUSTRIAL ROBOTS

– FOR OFF-LINE PROGRAMMING OF ROBOTISED LASER WELDING –

Rob Waiboer



Netherlands Institute
for Metals Research

This research was carried out under the project number MC8.00073 in the framework of the Strategic Research Programme of the Netherlands Institute for Metals Research in the Netherlands (<http://www.nimr.nl/>).

Dynamic Modelling, Identification and Simulation of Industrial Robots
– for Off-line Programming of Robotised Laser Welding –
Waiboer, Rob
ISBN 978-90-77172-25-4
© 2007 R.R. Waiboer, Veldhoven, the Netherlands.
Printed by PrintPartners Ipskamp.

DYNAMIC MODELLING, IDENTIFICATION AND SIMULATION OF INDUSTRIAL ROBOTS

– FOR OFF-LINE PROGRAMMING OF ROBOTISED LASER WELDING –

PROEFSCHRIFT

ter verkrijging van
de graad van doctor aan de Universiteit Twente,
op gezag van de rector magnificus,
prof.dr. W.H.M. Zijm,
volgens besluit van het College voor Promoties
in het openbaar te verdedigen
op woensdag 14 februari 2007 om 15.00 uur

door

Robert Rens Waiboer

geboren op 14 november 1972
te Noordoostpolder

**Dit proefschrift is goedgekeurd door
prof.dr.ir. J.B. Jonker, promotor
dr.ir. R.G.K.M. Aarts, assistent-promotor**

Voorwoord

In dit proefschrift zijn de resultaten van vier en een half jaar onderzoek vastgelegd. Het onderzoek is uitgevoerd binnen het Netherlands Institute for Metals Research (NIMR) en de vakgroep Werktuigbouwkundige Automatisering (WA) van de Universiteit Twente.

Als eerste wil ik het NIMR bedanken voor de mogelijkheid om het onderzoek uit te voeren. Bij het NIMR heb ik bijzonder fijn gewerkt en ik wil graag iedereen bedanken voor deze plezierige periode.

Verder wil ik mijn promotor Prof. Ben Jonker danken voor zijn steun en vertrouwen en de plezierige manier van samenwerken. In het bijzonder dank ik Ronald Aarts voor zijn ogenschijnlijke onvermoeibare inspanning en voor de fijne samenwerking.

Binnen de vakgroep WA was altijd een zeer prettige en ongedwongen atmosfeer, zowel tijdens het werk als ook tijdens de broodnodige koffiepauzes. Martina, Jeroen (JOB), Gert-Willem, Erwin, Sjoerd, Ingmar, Johannes, Hiddo, Menno, Benno, Tjeerd, Jeroen (JvT), Max, Dimitrios, Jonathan, Frits, Tyrone, Bertus, Jilles, Leo en Jan: hartelijk dank!

Natuurlijk wil ik ook de afstudeerders bedanken die een substantiële bijdrage geleverd hebben aan de inhoud van dit proefschrift: Ilse, Arjan, Jan, Susanne, Wim en natuurlijk Toon en Wouter.

Hans Stam en Geert Slootweg wil ik bedanken voor hun steun en het leggen van het eerste contact met Stäubli. Verder wil ik Luc Joly en Jean-Michel Bonnet van Stäubli Faverges bedanken voor hun support.

Vooral wil ik ook mijn ouders en zussen bedanken voor hun geduld en steun tijdens mijn onderzoek en het voltooien van mijn proefschrift. Tot slot wil ik Wendy danken voor haar onvoorwaardelijke steun tijdens de laatste loodjes.

Rob Waiboer,
Veldhoven, 1 januari 2007.

Contents

Voorwoord	i
1 Introduction	1
1.1 Principle of laser welding	2
1.2 Robotised laser welding	5
1.3 Off-line programming and dynamic simulation	6
1.4 Objective	8
1.5 Contributions	9
1.6 Outline of the thesis	10
2 The Stäubli RX90B robot	13
2.1 Robot system overview	13
2.2 Overview of the closed-loop robot model	16
2.3 The motion controller	17
2.4 The driving system	19
2.5 Discussion	22
3 Joint friction	23
3.1 Introduction	23
3.2 Friction modelling at system level	26
3.2.1 Classic friction models	26
3.2.2 Stribeck curve measurement	28
3.3 Friction modelling at contact level	32
3.3.1 Two lubricated discs in a rolling–sliding contact	32
3.3.2 Friction forces in the lubrication regimes	34
3.4 Friction models of elementary components	41
3.4.1 Friction model of a helical gear pair	42
3.4.2 Friction model of a prestressed roller bearing	45
3.5 The joint friction model	48

3.5.1	Friction model for the first four robot joints	49
3.5.2	Friction model of the wrist assembly	50
3.6	Friction parameter estimation	52
3.7	Temperature influence on friction behaviour	56
3.8	Pre-sliding friction	58
3.8.1	Kinematic pre-sliding modelling	58
3.8.2	Dynamic pre-sliding modelling	59
3.8.3	Kinematic vs. dynamic pre-sliding friction	61
3.9	Discussion	63
4	Robot arm	65
4.1	Introduction	65
4.2	Finite element model of the robot arm	67
4.2.1	Kinematic analysis	68
4.2.2	Dynamic analysis	70
4.3	Experimental parameter identification	76
4.3.1	The linear least squares problem	77
4.3.2	Solving the LS problem by singular value analysis	79
4.3.3	Error analysis of the LS problem	82
4.3.4	Scaling of the least squares problem	84
4.4	Identification experiments	87
4.4.1	Experiment design	87
4.4.2	Identification of the Stäubli RX90B	92
4.4.3	Validation of the identification experiments	97
4.4.4	Identification of the Stäubli RX90B with a payload	103
4.5	Discussion	104
5	Dynamic simulation	109
5.1	Introduction	109
5.2	Closed-loop dynamic robot model	109
5.3	Application of a perturbation method	111
5.4	Simulation experiment	115
5.4.1	Simulation results obtained with the nonlinear robot model	116
5.4.2	Simulation results obtained with the perturbation method	123
5.5	Off-line programming and dynamic simulations	125
5.5.1	Straight line motion	125

5.5.2	90° corner, the orientation of the welding head follows the orientation of the seam	127
5.5.3	90° corner, fixed welding head orientation	130
5.6	Discussion	132
6	Conclusions & Discussion	135
6.1	Conclusions	135
6.2	Discussion and suggestions for future research	137
A	Friction behaviour of a helical gear pair	141
B	Spatial finite elements	147
B.1	Spatial slider truss element	147
B.2	Lambda element	148
B.3	Spatial hinge element	149
B.4	Spatial beam element	150
C	Simulation results	153
C.1	Straight line motion	153
C.2	90° corner, welding head orientation follows the seam . . .	158
C.3	90° corner, constant welding head orientation	164
	Publications	169
	Bibliography	170
	Summary	179
	Samenvatting	181

Chapter 1

Introduction

The increasing demands for the automotive industry to manufacture high quality, safe, light-weight and environmentally more friendly automobiles necessitate the application of new metallic materials such as high-strength steels, aluminium and magnesium. Aluminium is applied to inner and outer panels, wheels and heat exchangers, for example. Magnesium finds its application in—amongst other things—transmission casings, instrument panels, intake manifolds, cylinder head covers and steering components. Automotive steels are used for space frames and body panels, for example, and come in a large variety of compositions; from zinc coated sheets for better corrosion resistance to special alloys for better formability of high-strength steels.

The employment of these automotive steels imposes challenging demands on production and joining techniques. Laser welding is a joining technique that is increasingly being applied in the automotive industry. It enables innovative techniques such as tailor-made blanks and tubes which are introduced in order to provide extra strength at only those locations where it is needed, e.g. near the hinges in car doors. A laser welded tailor-made blank (LWTB) is a flat assembly of metal sheets of dissimilar thickness, alloy or surface finish, yielding a new sheet with the appropriate properties at specific locations.

These tailored blanks and tubes are semi-manufactures that need further processing; tailored blanks are pressed into final shapes, e.g. car body panels, doors and roofs, while tubular blanks are hydro-formed—for example—into space frame parts. An example of an LWTB is given in figure 1.1. It shows the outer side body panel of the demonstration vehicle which is part of the Ultralight Steel Auto Body (ULSAB) pro-

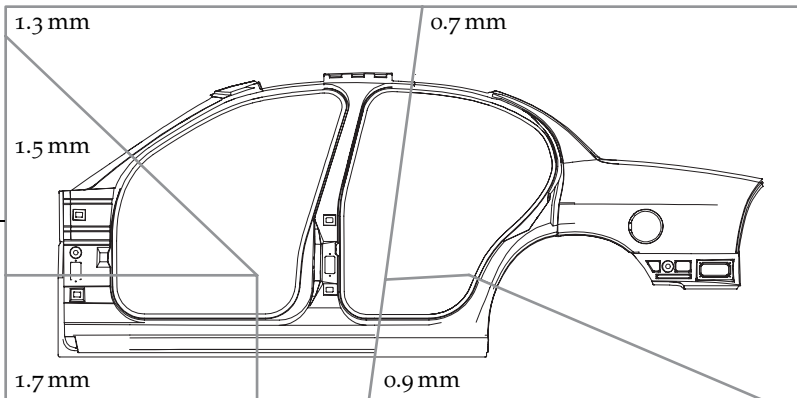


Figure 1.1: Laser welded tailored blank for the ULSAB outer side body panel (Porsche Engineering Services Inc., 1998). The tailored blank is assembled from five sheets of dissimilar thickness, ranging from 0.7 mm to 1.7 mm.

gram (International Iron & Steel Institute, 1998). A large group of steel manufacturers have started the ULSAB program to “demonstrate steel’s capability to reduce substantially the weight of a vehicle’s body structure and, at the same time, ensure safety with improved comfort and driving performance, all at affordable cost”.

The example of figure 1.1 shows that only linear weld seams are used. In view of subsequent manufacturing steps more optimal solutions may be found wherein nonlinear seams can be welded, e.g. to obtain a weld along an iso-strain path. Even more complicated seam geometries are found for the assembly of parts, e.g. the welding of hydro-formed tubes into a space frame. Seams are encountered that are along a complex three-dimensional path in space with a varying orientation.

1.1 Principle of laser welding

The principle of laser welding is to move a focussed laser beam over a seam. The laser beam is focussed on the material by means of a collection of optical devices such as lenses and mirrors assembled in a laser welding head. The laser radiation is absorbed by the metal and due to the high energy the metal changes locally from a solid state to a liquid state and a melt pool is formed. Due to the complex flow in the melt pool both

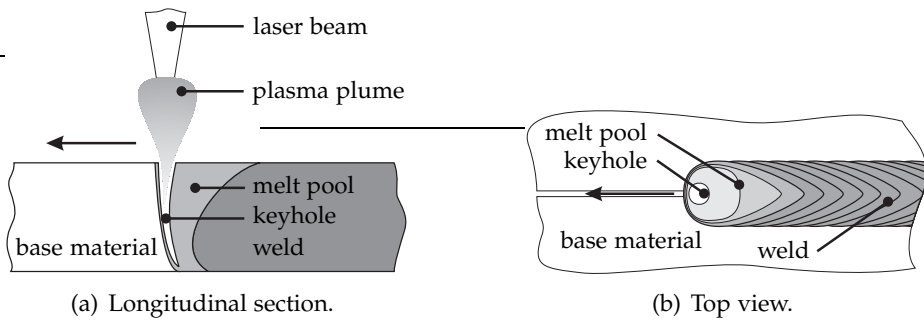


Figure 1.2: Illustration of the principle of keyhole laser welding.

metals are mixed and during solidification the metals are joined. Two different laser welding modes are distinguished: conduction mode welding and keyhole mode welding. In conduction mode welding the metal is only melted at the surface and the heat is transported into the material just by heat conduction. In this way, welding seams of a few tenth of a millimetre deep are formed. In figure 1.2, the keyhole laser welding mode is illustrated. In keyhole laser welding, the intensity of the laser radiation is sufficiently high to evaporate the molten metal at the focus of the laser beam. The recoil pressure of the metal vapour pushes the molten metal aside in a way so that it creates a capillary, known as the keyhole, which is filled with metal plasma. The keyhole can extend over the full thickness of the material. Figure 1.2(a) shows that some of the plasma escapes from the keyhole, forming a plasma plume above the material. The welding seam is usually protected from a reaction (oxidation) with the air by means of a shielding gas.

The great advantage of (keyhole) laser welding over conventional welding is the high welding speed that can be achieved while maintaining full penetration depth. Furthermore, laser welding requires few to no finish, making it an efficient joining technique. Another advantage of (keyhole) laser welding is the ability to join components where only one side is accessible, referred to as overlap welds.

Process windows, see figure 1.3, indicate the laser welding quality that is achieved when specific combinations of laser power and welding speed are applied. Too much laser power at low welding speed will result in excessive heat input and the molten metal may flow out of the seam,

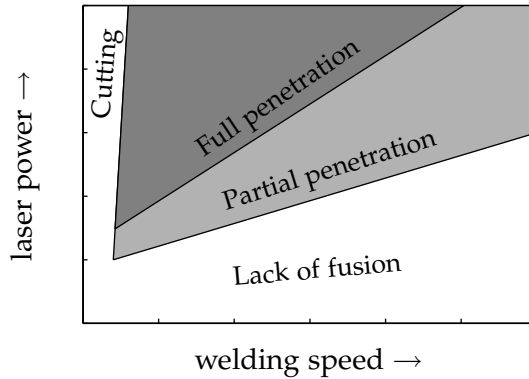


Figure 1.3: A typical process window for laser welding. The different areas indicate the quality of the weld at a certain combination of laser power and welding speed.

resulting in a cutting effect. On the other hand, a welding speed which is too high will result in insufficient heat input which leads to lack of fusion.

The process window illustrated in figure 1.3 shows sharp boundaries between the different areas of weld quality. However these boundaries are not as sharp as indicated here. Small differences in the process conditions—e.g. shielding gas flow, focus position and workpiece preparation—will influence the boundaries of the process windows. Variables that influence the laser welding process are, amongst others:

- type of metal alloy,
- surface condition of the metal, e.g. oxidation, protective coatings,
- thickness of the material,
- edge preparation of the metal,
- weld type, e.g. butt weld, overlap weld,
- orientation of the weld,
- welding optics and
- shielding gas.

Changing one of these variables may give rise to a modified process window and eventually a process window has to be determined that fits specifically with the new configuration.

For the welding of linear welds, as in tailor-made blanks, one process window can be considered along the weld seam as the weld conditions are more or less invariant. For the welding of complex three-dimensional products such as space frames, the orientation of the weld constantly changes along the weld seam. As the process window changes as a function of the orientation, the welding conditions change as well (Su, 2000). Hence, the optimal settings of the welding parameters may vary along the seam.

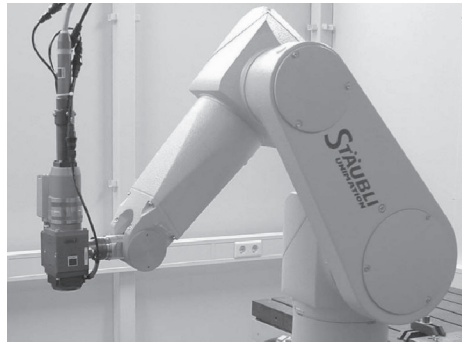
The required path tracking accuracy is mainly determined by the working range of the beam; a function of wavelength, diameter of the unfocused beam, and focal length of the focus lens. As there is a selection of different focal lengths that may be used, a single set of values for the path tracking accuracy in either lateral and focal direction does not exist. In this work a rather demanding example has been chosen. For laser welding of steel sheets using a diameter of the laser at the focal point of 0.3 mm and a focal length of 100 mm, it was found (Römer, 2002) that a lateral tolerance of ± 0.1 mm has to be satisfied in order to avoid weld quality degradation. The requirements for the vertical tolerance are less strict in general, although for these welds changes in the vertical position in the order of 0.1 mm give rise to quality changes as well. Hence, tolerances of ± 0.1 mm in both directions will be taken as typical values.

1.2 Robotised laser welding

The manipulation of the laser welding head with respect to the seam is done with robotic manipulators. For the laser welding of nonlinear seams in tailored blanks, gantry manipulators are being used, see figure 1.4(a). Such manipulators have a good dynamic performance as is needed for such welds. A drawback of such systems is the high investment costs, which makes them only economically affordable for large product series. Furthermore, the accessibility of welds in three-dimensional assemblies is poor for these gantry manipulators. Six-axis robotic manipulators, see figure 1.4(b), on the other hand, are cheaper and can reach more complicated seams, thus opening a wider range of applications. However, their accuracy is less, so a tradeoff has to be made between the complexity of



(a) Five-axis gantry robot. Courtesy of TRUMPF GmbH + Co. KG.



(b) Six-axis robot arm with a laser welding head attached.

Figure 1.4: Two typical robot systems for laser welding applications.

the seams and the required weld quality. In this thesis the focus is placed on the six-axis robotic manipulators and, in particular, a prediction of the achievable accuracy.

Welding nonlinear seams is not a trivial extension of laser welding of linear seams. The capabilities of the manipulator used for the welding task have to be taken into account. The manipulator may have a limited performance regarding the tracking accuracy of the focal point of the laser beam with respect to the seam, which should stay within strict boundaries. In addition, the accessibility of the seam can also be a problem in complex three-dimensional products. Testing on the real equipment should be avoided as it is expensive. Hence an investigation of the ability to weld such nonlinear seams with a robotic manipulator has to be carried out already during the planning of a laser welding job.

1.3 Off-line programming and dynamic simulation

To include the behaviour of the manipulator in the planning of a laser welding job, off-line programming (OLP) can be used to determine *a priori* the optimal weld trajectory and process settings needed to meet product specifications. This OLP should involve a realistic simulation of the welding process. These simulations must be capable of predicting the weld quality that will be obtained for a specific material, seam geometry and manipulator. Knowledge of the process window is an important pre-

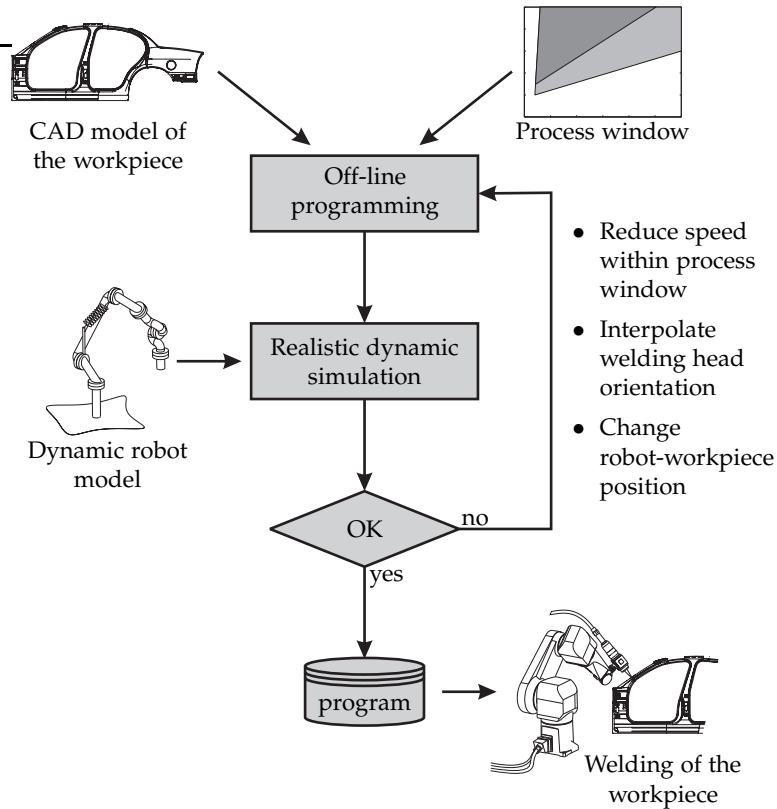


Figure 1.5: Overview of the process of off-line programming, integrated with realistic dynamic simulations, of a laser welding job.

requisite, e.g. optimal welding speed and laser power combinations and minimum required welding speed. Furthermore, an accurate simulation of the motion of the robot or manipulator is needed to investigate the extent to which performance limitations affect the weld quality.

Figure 1.5 illustrates the work flow of the off-line programming process using realistic dynamic simulations of the robot motion. The first step is to import the workpiece as a 3D-CAD geometry into the off-line programming system. Then, the geometrical motion paths (welding seams and intermediate points) are specified at the workpiece. Attributes such as welding speed and process parameters are assigned by selecting a proper combination of welding speed and laser power from the process

window. Furthermore, the motion parameters, e.g. interpolation type, are set. In this stage it is already possible to take both process and kinematic limitations into account (Backes, 1999).

If the workpiece programming is finished the question is always whether or not the program is executable. The selected robot with its tool (the laser welding head) must conduct the program collision-free, without leaving the joint travel ranges, without exceeding the joint velocities and joint accelerations in the planned or already existing work cell. In addition, the problem of accessibility and possible occurrence of nearly singular robot positions must be addressed. Professional off-line programming systems, such as TopLas3D[®] (Mebitec, 2006), have a 3D simulation section, in which robots, tool, workpiece and working environment are present. The pre-developed program can be executed in the 3D simulation directly and examined for collision etc. Problems that have been detected during the kinematic simulation are indicated along the trajectory and can be solved by moving trajectory points or changing orientation, for example. A further possibility is to shift the robot basis or the location of the workpiece to the robot, until the entire program is executed successfully.

Keeping in mind the limited dynamic performance of the robotic manipulator, a second step is proposed in figure 1.5. In this second step, a realistic dynamic simulation of the laser welding job is performed in order to check the path tracking accuracy of the robot with the required path tracking accuracy. If the path tracking accuracy appears to be insufficient, it is necessary to modify the laser welding job in such a way that it becomes feasible. This is an iterative process in which welding speed, orientation and location of the workpiece, etc. are optimised. After the optimisation, the laser cell can be set up properly and the robot program is downloaded on the robot and the welding operation can start.

1.4 Objective

The off-line programming process as was outlined in the previous section includes the step in which a realistic dynamic simulation of the laser welding job is carried out. Present off-line programming systems do not include such a feature; they are only capable of kinematic simulations of the robotic manipulator (Waiboer, 2000). As laser welding is highly demanding with respect to welding speed and required path tracking

accuracy, realistic dynamic simulations are needed in the process of off-line programming in order to *a priori* detect problems. From these two facts the following objective has been formulated:

The development of a realistic dynamic simulation model of an industrial robot in order to support off-line programming of laser welding jobs with a prediction of the dynamic performance of the robot's motion.

Developing a realistic dynamic simulation model of an industrial robot involves three major steps:

1. Build a model structure with a set of dynamic equations that describe the relevant physical phenomena of the industrial robot correctly.
2. Determine the model parameters, either from manufacturers data or by means of model identification techniques.
3. Validate the dynamic robot model by means of performing several typical motion experiments with both the real robot and the model.

In this thesis, these three steps will be carried out for a Stäubli RX90B industrial robot.

1.5 Contributions

The modelling and identification of industrial robots has already been covered extensively in literature as will become clear in the next chapters. In this thesis several contributions have been made to this subject which can be summarised as follows:

- The modelling of joint friction with commonly used so-called classic friction models is evaluated. It will be shown that these models are not able to describe joint friction accurately. A new friction model is developed that relies on insights from sophisticated tribological models. The new friction model accurately describes the friction behaviour in the sliding regime with a minimal and physically sound parametrisation.
- This thesis shows the application of a finite element representation for the modelling of the robot arm. The equations of motion are determined in terms of the joint degrees of freedom (Lagrange formulation).

- The parameter identification method commonly used in robotics is reconsidered and the model parameters are compared with manufacturer's data. By means of a singular value analysis and a scaling operation, the identifiability of the model parameters is discussed. Additionally, a method is presented which enables verification of an identified reduced parameter set with a full set of model parameters, for instance manufacturer's data.
- Finally, closed-loop dynamic simulations are carried out with the identified robot model. A perturbation method is applied which makes the simulations significantly more time efficient. A series of motion experiments is done both with the actual robot and the simulation model. Motion experiments clearly show the ability to *a priori* detect welding defects as a result of path tracking errors. Furthermore, they illustrate typical difficulties that arise in robotised laser welding.

1.6 Outline of the thesis

In chapter 2 the general layout of the Stäubli RX90B robot is discussed. It includes the description of the robot controller and the driving system. Chapter 3 discusses the modelling and parameter identification of the friction torques that arise in the robot joints. The application of phenomenological friction models for the modelling of friction in the sliding regime will be evaluated. Furthermore, a new friction model will be developed that relies on insights from tribological models. The friction model is then incorporated into a so-called pre-sliding model in order to sufficiently describe friction torques at zero velocity and at velocity reversals.

The modelling and identification of the inertia properties of the robotic arm will be covered in chapter 4. First, the nonlinear finite element formulation will be introduced. This formulation is used to derive the dynamic model of the robot. Secondly, the dynamic model of the robot is written in a parameter linear form so that linear regression techniques can be applied to identify the unknown model parameters. Then the identification technique will be discussed, including the experimental design. Finally, the unknown inertia parameters of the robot will be identified. The identified parameters are validated experimentally and they are compared with manufacturer's data.

In chapter 5, the models of the robot subsystems that were derived in the first chapters are assembled into a complete model of the closed-loop robot system. A perturbation method will be introduced in order to improve the computational efficiency of the dynamic simulations. With both the nonlinear and the perturbation models, motion experiments will be carried out. The simulation results are then validated by means of measurements done on the actual robot while performing the motion experiments. Subsequently, the applicability of realistic dynamic simulations for off-line programming will be demonstrated by means of motion experiments regarding typical laser welding trajectories. Finally, concluding remarks and recommendations for future research are given in chapter 6.

Chapter 2

The Stäubli RX90B robot

2.1 Robot system overview

The Stäubli RX90B industrial robot, illustrated in figure 2.1, is a so-called *robotic manipulator* which bears a strong resemblance to the human arm. The robotic arm, an articulated mechanical structure, is an assembly of links interconnected by joints. The base and joints 1 and 2 form the shoulder of the robot. Joint 3 is the elbow and joint 4 attaches the forearm. Joints 5 and 6 make up the robot wrist.

The role of the articulated structure is to move and/or manipulate the end-effector which is attached at the end of the wrist, at link 6. The end-effector may be a gripper device intended to manipulate objects. In this thesis, the end-effector is the laser welding head which was shown in figure 1.4(b), page 6.

A general overview of the robotic system hierarchy is shown in figure 2.2. The robotic system is divided into six layers. Starting at the first and bottom layer, there is the mechanical manipulator arm, which consists of stiff and lightweight aluminium robot links that are interconnected by means of six revolute joints. The manipulator arm also includes a gravity compensating spring, mounted inside link 2, which balances the unloaded arm. The first 4 joints are equipped with the so-called Stäubli Combined Joints (JCS), which contain both the joint transmission and the joint bearing assembly. The remaining two joints of the wrist assembly are coupled due to the fact that the motors for joint 5 and 6 are both mounted inside link 4 and the fact that joint 6 is driven via joint 5. The driving system will be discussed in detail in section 2.4.

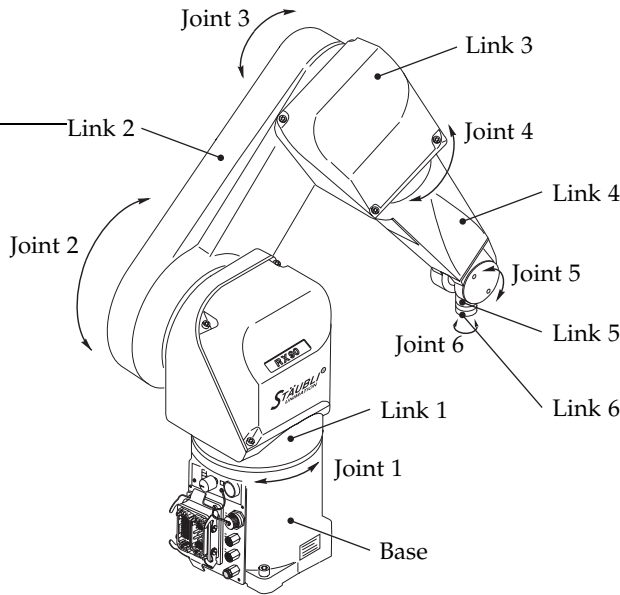


Figure 2.1: The Stäubli RX90B six-axis RRR-RRR industrial robot. Courtesy of Stäubli, Faverges, France.

The second layer involves the three-phase servo motors that drive the joints via dedicated transmissions. Resolvers on the motor axis measure its position and velocity. The types of actuators determines the maximum amount of power that can be supplied to the robot joints. The resolution of the resolvers determine the theoretical upper bound for the robot's accuracy.

The third layer provides the electronic interfaces. It contains the six integrated servo amplifiers that drive the servo motors. Furthermore, it provides the hardware for the robot's safety system, such as emergency stops and power supply of servo amplifiers, including the motor brakes.

The fourth layer encompasses the motion control. Although the motion control is integrated within the servo amplifier hardware, it is considered a separate layer. These servo amplifiers are equipped with a DSP (Digital Signal Processor) on which a SISO (Single Input, Single Output) motion control algorithm is running. The control algorithm will be discussed in section 2.3. The interface to the fifth layer is provided by a dedicated SERCOS bus (SERCOS, 1998). The SERCOS interface is an open

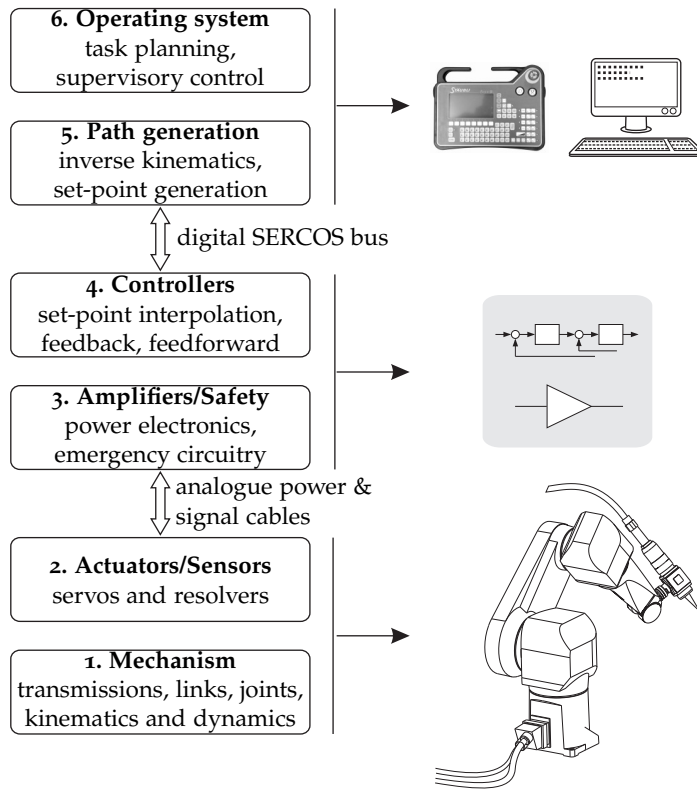


Figure 2.2: General system overview of the Stäubli RX90B robot.

interface specification for the communication between a master controller and intelligent digital servo drives and is based on an optical ring topology with a time-triggered master-slave communication.

The fifth layer involves the robot's kinematic and inverse kinematic models and the motion generator. It provides the joint set-points to the fourth layer via the SERCOS bus. Finally, the sixth and top layer provides the supervisory control of the robot. It governs the task planning and it provides interfaces to the operator and programmer. Furthermore, it can interface via ethernet and/or field busses with external devices, such as sensors, laser sources and analogue or digital inputs and outputs.

The fifth and sixth layers are implemented within software which runs on an industrial PC equipped with the VxWorks operating system (Wind-River, 2004). A SERCOS master controller card provides the communica-

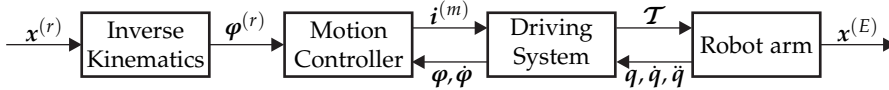


Figure 2.3: Block diagram of the closed-loop robot model.

tion between the PC and the SERCOS bus. A teach pendant is connected to the industrial PC and functions as the main interface between the operator and the system controller.

2.2 Overview of the closed-loop robot model

For the dynamic modelling of the robot system, only the layers 1 through 5 will be considered and the supervisory control of the robot will not be included in the robot model. The block diagram of the closed-loop robot system that will be modelled is shown in figure 2.3.

The input of the block diagram is the reference trajectory $x^{(r)}(t)$. With the inverse kinematic model, the values of the joint angles as a function of the desired tip position and orientation are computed. In this case the transformations of the joint axes to the motor axes are also included in the inverse kinematic model in such a way that the motor positions $\varphi^{(r)}$ become the output of the block.

Note that the inverse kinematic model of the Stäubli RX90B generally has eight different solutions, yielding eight different robot poses. Furthermore, there are reference points $x^{(r)}$ for which the inverse kinematic solution has an infinite number of solutions. These points are known as singular positions. An example of a singular position is the case wherein the angular position of axis 5 equals zero resulting in joint 4 and joint 6 being aligned. The inverse kinematic solution then includes any value $q_6 = -q_4 \in \mathbb{R}$. For further reading on inverse kinematics the reader is referred to e.g. Khalil and Dombre (2002).

The next block is the motion controller block, which governs the motion of the servo motors by measuring their position φ and velocity $\dot{\varphi}$ and by regulating the output current $i^{(m)}$. The motion controller will be discussed in section 2.3.

The third block encompasses the joint driving system. The servo motors mounted inside the drives convert the electrical current $i^{(m)}$ to a me-

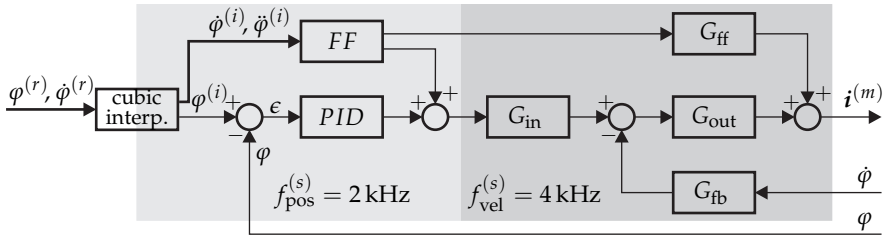


Figure 2.4: Block diagram of the motion controller for a single servo.

chanical motor torque. The motor torques are transformed to joint torques \mathcal{T} by the joint transmissions. Inversely, the joint angles \mathbf{q} and their time derivatives are transformed into motor angles and their time derivatives. The driving system will be discussed in section 2.4.

The final block is the block denoted by *robot arm*. This block encompasses the forward dynamic model of the robot arm. It computes the motion of the robot arm as a function of the joint torques \mathcal{T} . The motion of the robot arm is expressed in terms of a set of generalised degrees of freedom \mathbf{q} , being the six joint angles, and their time derivatives $\dot{\mathbf{q}}$ and $\ddot{\mathbf{q}}$. The modelling of the robot arm will be discussed extensively in chapter 4.

The robot arm block also includes the kinematic model of the robot that computes the actual Cartesian position and orientation, and time derivatives, of the robot tip $(\mathbf{x}^{(E)}, \dot{\mathbf{x}}^{(E)})$ as a function of the joint positions \mathbf{q} and velocities $\dot{\mathbf{q}}$.

2.3 The motion controller

The Stäubli robot is equipped with so-called independent *PID* feedback controllers. The term independent refers to the fact that every servo motor is equipped with a Single Input Single Output (SISO) controller. The controllers are implemented in customised digital amplifiers/controllers of the type “ServoStar”, manufactured by Kollmorgen (2004a). In figure 2.4, the block scheme of a single motion controller is depicted.

The inputs of the motion controller are the motor reference position $\varphi^{(r)}$ and velocity $\dot{\varphi}^{(r)}$, which are presented at a rate of 250 Hz via the SERCOS bus. A so-called micro-interpolator interpolates the reference position and velocity commands by means of a cubic polynomial. The

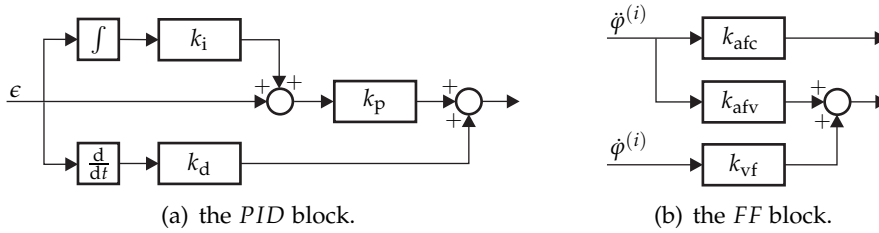


Figure 2.5: Block diagrams of the position loop and the acceleration and velocity feed forwards of the motion controller.

output position, velocity and acceleration ($\varphi^{(i)}$, $\dot{\varphi}^{(i)}$, $\ddot{\varphi}^{(i)}$) are computed at a rate of 2 kHz.

The interpolated reference position $\varphi^{(i)}$ is compared to the actual motor position φ , and the difference is the position error ϵ . The position error is the input of the *PID* controller block, illustrated in figure 2.5(a). The proportional control action (*P*) is obtained by multiplying the position error ϵ with the proportional gain k_p , yielding a motor torque which is proportional to the position error. An integrating action, denoted by *I*, is introduced in the controller to reduce the steady-state position error that is caused by joint friction. The position error is integrated by the \int -block and multiplied with the integrator gain k_i , yielding the motor torque of the *I*-action.

In order to provide stability, a damping term *D* can be added to the *P*-controller, where the time derivative $\dot{\epsilon}$ of the position error is numerically derived by the $\frac{d}{dt}$ -block. Multiplication with the derivative gain k_d yields the motor torque associated with the *D*-action. For motion control, however, the numerical derivation of the error velocity is not preferable as it generally yields high frequency noise on the velocity signal. Since the servo motors are equipped with resolvers, a high quality velocity signal is available. This velocity signal will be used to provide the damping action in a separate velocity loop. Consequently, the *PID* controller is configured as *PI* controller by setting the derivative gain to zero, $k_d = 0$. The resulting *PI* position loop is running at 2 kHz. The velocity loop is added to the motion controller as depicted in figure 2.4. The velocity loop is built up with three filters; an input filter G_{in} , a velocity feedback filter G_{fb} and an output filter G_{out} . The velocity loop is running at 4 kHz.

In order to improve the trajectory tracking performance of the controller, a feed-forward block is added to the controller. The velocity $\dot{\varphi}^{(i)}$

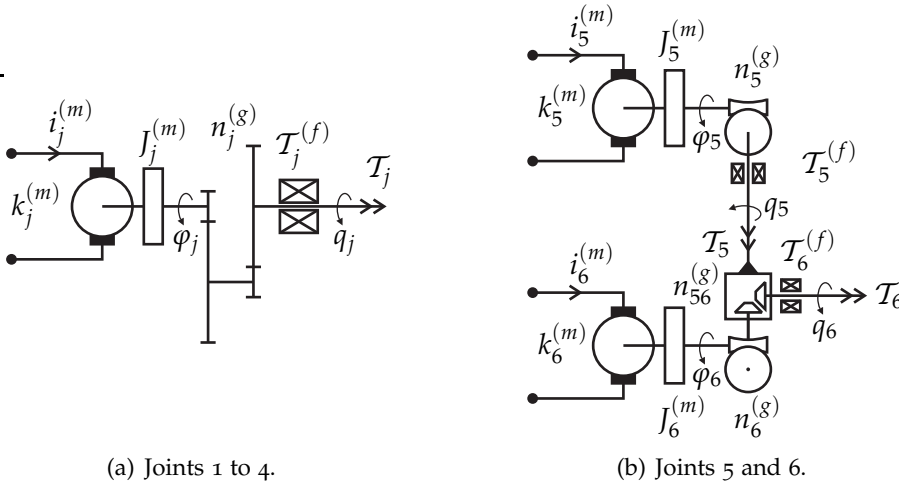
and acceleration $\ddot{\varphi}^{(i)}$, which have been computed by the micro interpolator, are fed into the feed-forward block, see figure 2.5(b). Multiplying the acceleration $\ddot{\varphi}^{(i)}$ with the constant gain k_{af} provides a feed-forward torque which is proportional to the motor torque required for the acceleration of the specific motor and load. Observe that a feed forward error is introduced because the acceleration feed-forward gain k_{af} is constant, while the inertial load changes with the robot's configuration. The acceleration feed-forward can either be fed to the current output via the low-pass filter G_{ff} by setting k_{afc} , or be fed to the input of the velocity loop by setting k_{afv} . Multiplying the velocity $\dot{\varphi}^{(i)}$ with a gain k_{vf} provides a torque signal that is applied for compensation of the viscous friction torque generated inside the robot joints.

The output of the velocity loop, the current signal $i^{(m)}$, is the input for the current control loop which provides both the power amplification and the commutation; it computes the three-phase currents needed for the servos as a function of both the angular position of the rotor and the sign of the requested current $i^{(m)}$. In the model, the commutation is omitted and the three-phase currents are replaced by the equivalent current $i^{(m)}$. Furthermore, it is assumed that the current loop behaves as an ideal amplifier with unity gain.

The controller model has been derived from the Servostar documentation (Kollmorgen, 2004c,b) and with the support of the Stäubli factory. In those instances wherein the documentation was unclear concerning the exact locations of a filter or the occurrence of quantisation, for example, assumptions have been made regarding these aspects. The controller model has been verified by means of system identification tools. The ultimate verification of the closed-loop behaviour of the dynamic robot model will be performed in chapter 5.

2.4 The driving system

The layout of the driving system of the Stäubli robot is illustrated in figure 2.6. For each of the first four joints of the Stäubli robot, figure 2.6(a) is a schematic representation of the JCS (Stäubli Combined Joint), which is a sophisticated assembly that includes both a cycloidal transmission and the joint bearing support (Gerat, 1994). The cycloidal transmission is driven by a servo motor via a helical gear pair. The last two joints in the robot's wrist, see figure 2.6(b), are driven via a worm and wheel gear



(a) Joints 1 to 4.

(b) Joints 5 and 6.

Figure 2.6: Layout of the driving system of the Stäubli RX90B robot.

(Gerat and Palau, 1998). Furthermore, joint six includes a (spiral) bevel gear pair.

The servo motors are brushless three-phase servo motors. In this thesis, the three-phase currents are replaced by one equivalent DC current for simplification. The motor constant is assumed to be fixed, while in reality it may vary as a function of the angular velocity. This is caused by the fact that the servo behaves as a low pass filter for the three-phase currents. Here it is assumed that this effect will arise only at very high angular velocities, close to the velocity limits of the joints. The servo motor transfers the electrical current i_j into a torque delivered at the motor axis:

$$\mathcal{T}_j^{(\varphi)} \equiv i_j^{(m)} k_j^{(m)} - J_j^{(m)} \ddot{\varphi}_j, \quad (2.1)$$

where $k_j^{(m)}$ is the motor constant and $J_j^{(m)}$ is the rotor inertia. Note that the rotor inertia $J_j^{(m)}$ also includes part of the rotational inertia of the gears. The motor axis angular position is denoted by φ_j . From equation (2.1) it is clear that the acceleration of the rotor inertia is already accounted for in the computation of the motor torque $\mathcal{T}_j^{(\varphi)}$.

The relations between the vector of motor axis positions φ and joint

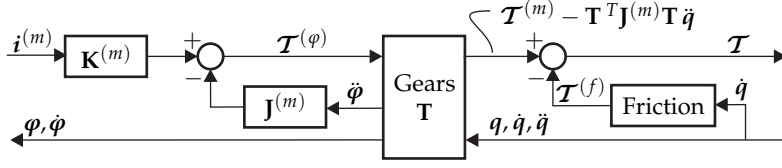


Figure 2.7: Block diagram of the driving system.

positions q and their time derivatives are given as:

$$\varphi = \mathbf{T}q, \quad (2.2a)$$

$$\dot{\varphi} = \mathbf{T}\dot{q}, \quad (2.2b)$$

$$\ddot{\varphi} = \mathbf{T}\ddot{q}, \quad (2.2c)$$

where the matrix \mathbf{T} contains the gear ratios and is defined as:

$$\mathbf{T} = \begin{bmatrix} n_1^{(g)} & 0 & 0 & 0 & 0 & 0 \\ 0 & n_2^{(g)} & 0 & 0 & 0 & 0 \\ 0 & 0 & n_3^{(g)} & 0 & 0 & 0 \\ 0 & 0 & 0 & n_4^{(g)} & 0 & 0 \\ 0 & 0 & 0 & 0 & n_5^{(g)} & 0 \\ 0 & 0 & 0 & 0 & n_{56}^{(g)} & n_6^{(g)} \end{bmatrix}. \quad (2.3)$$

It is assumed that the transmission is ideal, i.e. \mathbf{T} is constant and no backlash or other nonlinear behaviour is present. Furthermore, all losses due to friction are gathered in a single vector $\mathcal{T}^{(f)}$ of joint friction torques. The input–output equation of the complete drive system is then

$$\mathbf{T}^T(\mathbf{K}^{(m)}\mathbf{i}^{(m)} - \mathbf{J}^{(m)}\ddot{\varphi}) - \mathcal{T}^{(f)} = \mathcal{T}, \quad (2.4)$$

where $\mathbf{K}^{(m)} = \text{diag}(k_1^{(m)}, k_2^{(m)}, \dots, k_6^{(m)})$ is a matrix with the motor constants on its diagonal and $\mathbf{J}^{(m)} = \text{diag}(J_1^{(m)}, J_2^{(m)}, \dots, J_6^{(m)})$ is a diagonal matrix with the motor rotor inertias. The vector of output joint torques is defined as \mathcal{T} . Rearranging and substitution of equation (2.2c) yields

$$\mathcal{T}^{(m)} - \mathbf{T}^T \mathbf{J}^{(m)} \mathbf{T} \ddot{q} - \mathcal{T}^{(f)} = \mathcal{T}, \quad (2.5)$$

where

$$\mathcal{T}^{(m)} = \mathbf{T}^T \mathbf{K}^{(m)} \mathbf{i}^{(m)} \quad (2.6)$$

is defined as the vector of motor torques.

2.5 Discussion

In this chapter, the Stäubli RX90B industrial robot was introduced. Its main elements, the robot arm, the driving system including friction and the robot controller were pointed out. The general robot set-up was discussed first. Then, the control system was explained. Finally, the driving system was presented and the joint friction torques were separated from the driving model.

Note that several modelling assumptions have been made in this chapter; the transmission is assumed to be ideal and the joint friction torques are assumed to be single friction torques acting on the robot joints. Consequently, it needs to be verified and validated whether or not these assumptions are justified. This will become clear in three steps:

1. In chapter 3, joint friction modelling and identification will be discussed. This will be the first opportunity to test if it is correct to include joint friction as single friction torques acting on the robot joints.
2. The second test will be the identification of the robot arm. Since the joint torques can only be measured indirectly via the motor currents, it is required that the models of the drives and joint friction are included accurately. This will be discussed in chapter 4, where the modelling and identification of the robot arm is discussed.
3. The final test will be carried out in chapter 5, where typical robot trajectory motions are simulated using the complete dynamic closed-loop robot model. The verification of the simulation results by means of measurements on the robot will then demonstrate whether or not the modelling assumptions were justified and if the dynamic model can predict the trajectory tracking capabilities of the robot for specific laser welding jobs with sufficient accuracy.

Chapter 3

Joint friction

3.1 Introduction

Robotic manipulators are subject to joint friction which arises in the bearings, transmissions and seals, in other words at every point where two surfaces are in relative motion and in contact. Numerous factors, such as surface roughness and topology, lubricant viscosity, load, (local) temperature and velocity influence the friction forces at the contacting surfaces. In order to gain an understanding of friction in the six joints of the Stäubli RX90B robot, a closer look is taken at the joint construction and the contacts between the components.

The first four joints of the Stäubli RX90B robot, see figure 3.1(a), are equipped with a so-called JCS (Stäubli Combined Joint), which is a sophisticated assembly that includes both a cycloidal transmission and the joint bearing support (Gerat, 1994). The cycloidal transmission is driven by a servo motor via a helical gear pair. The gears and bearings in the cycloidal transmission are prestressed in order to eliminate any backlash. Both the cycloidal transmission and the helical gear pair are constantly lubricated in order to reduce friction losses and to minimise wear. The remaining two joints in the robot's wrist, see figure 3.1(b), are driven via a worm and wheel gear (Gerat and Palau, 1998). Furthermore, joint six includes a (spiral) bevel gear pair.

Accurate modelling of the friction behaviour of the robot joints requires that the friction model is based on the physics of friction. The science of the physics of friction is known as tribology. Documented tribology research dates back to the work of Leonardo da Vinci (1452-1519).

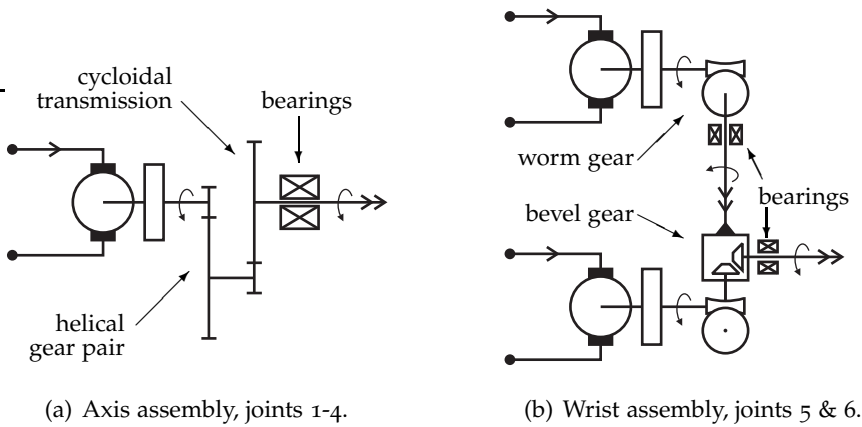


Figure 3.1: Schematic overview of the components in the robot drives that are subject to friction.

The engaging work of Dowson (1998), entitled “History of Tribology”, illuminates the 3000-year history of man’s attempts to understand and modify friction. Today, tribology research is largely focussed on the issues of wear and machine life on one hand, and on surface chemistry and physics on the other. However, for the control of machines the main interest in friction phenomena lies in the field of frictional dynamics; the way in which friction influences the dynamic behaviour of the machine. A comprehensive survey paper by Armstrong-Hélouvry et al. (1994) discusses the studies carried out in the field of frictional dynamics during the past few decades.

In this thesis, the focus will be on the friction characteristics of the main components in the robot’s joints and transmissions: bearings and gears. In friction research applied to robotics, it is common to distinguish between the so-called sliding regime and the pre-sliding regime. In the sliding regime, the friction forces that arise at nonzero surface velocities are studied. In the pre-sliding regime, friction forces are evaluated for states where the surface velocities are zero or close to zero.

Joint friction in both the sliding and the pre-sliding regimes is quite important for dynamic robot modelling employed for laser welding; due to the nonlinear kinematic nature of the robot, straightforward welding trajectories may require fast motions and rapid reversals of the robot’s

axes velocity. The velocities at which the axes operate is roughly in between -4 rad/s and 4 rad/s . Taking into account that the transmission ratio is of the order of 100, the velocity of the servo axis may reach 400 rad/s . Furthermore, during a reversal of the joint velocity, the pre-sliding regime is applied. Consequently, a friction model has to be able to describe both regimes with sufficient accuracy with respect to the dynamic modelling and identification of the complete robot.

Commonly, friction modelling in tribology is based mainly on physical principles; friction phenomena are often observed at the level of a single sliding or rolling surface contact. The model parameters are then directly related to the physical properties of the surfaces and the applied lubricant. A friction model of a complete system, such as a roller bearing or gear pair, evaluates the friction forces at every single contact and—since there are many contacts—this generally yields elaborate friction models that are computationally very expensive (Spikes, 2001).

Therefore, many authors have developed phenomenological friction models that describe the essential friction phenomena arising in servo-controlled mechanical systems. Olsson et al. (1998) have given an elaborate overview of—mostly phenomenological—friction models known in control systems literature. Model parameters for these phenomenological models generally do not have a direct relation with the physical properties of the contacts in the system at which the friction forces arise.

Outline

In this chapter, the modelling and identification of joint friction will be discussed. The focus is on the sliding regime, initially. First, in section 3.2, the applicability of phenomenological friction models that are commonly used in control literature is investigated. A brief overview is given of the phenomena that are covered by these phenomenological models. Based on the overview, a phenomenological joint friction model will be formulated. Subsequently, the model parameters are obtained by means of experiments. It will be shown that the phenomenological models are inadequate to describe the friction behaviour for the full velocity range with sufficient accuracy.

A new joint friction model will be proposed that relies on insights from sophisticated tribological models. The basic friction model of two lubricated discs in a rolling-sliding contact is used to analyse viscous friction and friction caused by asperity contacts inside gears and roller

bearings of robot joints and drives. The sub-models that describe viscous friction and friction due to asperity contacts are combined into two friction models: one for gears and one for prestressed roller bearings. The development of these friction models is covered in sections 3.3 to 3.5. In this way a new friction model is developed that accurately describes the friction behaviour observed in the Stäubli RX90B robot. Next, in section 3.6, the joint friction model parameters will be identified by means of experiments. It will be shown in section 3.7 that the model is linear in parameters that depend on the temperature of the robot drives, which makes it very suitable to include the friction model in the identification experiments carried out for obtaining the inertia parameters. Finally, in section 3.8, the model is extended in such a way that it can describe the joint friction behaviour in the pre-sliding regime during reversals of the joint velocity.

3.2 Friction modelling at system level

3.2.1 Classic friction models

Most (phenomenological) friction models in control literature are combinations of the classic friction models, see figure 3.2. Friction normally is described as the product of a coefficient of friction and a normal force. For modelling of friction in robots with revolute joints, friction is mostly considered to be load independent. Therefore, friction is usually modelled as a joint torque $\mathcal{T}_j^{(f)}$ that is a function of its angular joint velocity \dot{q}_j . The subscript j denotes the joint number.

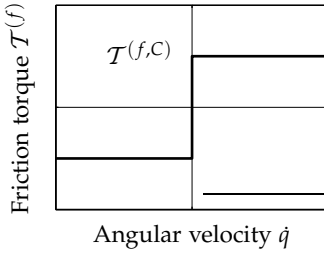
The model that is shown in figure 3.2(a) is known as the Coulomb friction model. The Coulomb friction model is given as

$$\mathcal{T}^{(f)} = \text{sign}(\dot{q}) \mathcal{T}^{(f,C)}, \quad (3.1)$$

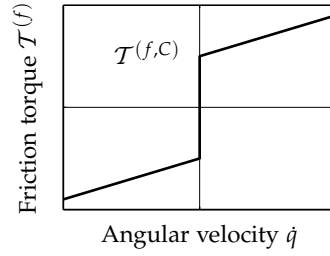
where $\mathcal{T}^{(f,C)}$ is the Coulomb friction torque and \dot{q} is the angular velocity. The Coulomb friction model originates from the friction between sliding dry surfaces which generally produce large friction forces. Note that $\text{sign}(\dot{q})$ is not defined for zero velocities. This means that the model is not able to describe the friction torque for a velocity equal to zero.

The application of a lubricant results in the addition of a viscous term in the friction model

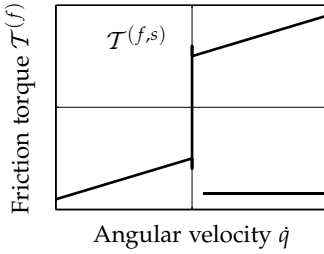
$$\mathcal{T}^{(f)} = \text{sign}(\dot{q}) \mathcal{T}^{(f,C)} + c^{(v)} \dot{q}, \quad (3.2)$$



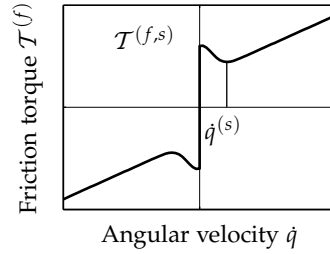
(a) Coulomb friction, Da Vinci (1452-1519), Amontons (1699) and Coulomb (1785), equation (3.1).



(b) Coulomb & viscous friction, Newton (1642-1727), equation (3.2).



(c) Coulomb, viscous and static friction, Euler (1707-1783), equation (3.3).



(d) The Stribeck effect, Armstrong-Hélouvy (1991), equation (3.5).

Figure 3.2: Classic friction models.

where $c^{(v)}$ is the viscous friction parameter. Viscous friction is taken in this model as a linear function of the angular joint velocity, see figure 3.2(b).

The Swiss scientist Euler (1707-1783) found that a higher force was needed to bring the surfaces in a sliding motion than is needed to keep the surfaces in motion, see figure 3.2(c). This so-called static friction effect is taken into account as

$$\mathcal{T}^{(f)} = \begin{cases} |\mathcal{T}^{(f)}| \leq \mathcal{T}^{(f,s)} & \text{if } \dot{q} = 0, \\ \text{sign}(\dot{q}) \mathcal{T}^{(f,C)} + c^{(v)} \dot{q} & \text{if } \dot{q} \neq 0, \end{cases} \quad (3.3)$$

where $\mathcal{T}^{(f,s)}$ is the static friction torque and $\mathcal{T}^{(f,C)} < \mathcal{T}^{(f,s)}$. Note that this model gives a non-unique solution for the friction torque for zero

velocities and that it shows discontinuous behaviour in a transition from zero velocity to nonzero velocity.

Stribeck (1902) discovered that the drop from static friction to Coulomb friction is not discontinuous for lubricated surfaces but that it is a continuous function of the velocity (Jacobson, 2003), see figure 3.2(d). Therefore, the graph representing the relationship between friction and velocity will hereafter be referred to as the Stribeck curve. Bo and Pavlescu (1982) developed a well-known model describing the Stribeck effect, which displays an exponentially decrease from the static friction to the Coulomb friction:

$$\mathcal{T}^{(f)} = \text{sign}(\dot{q}) \left(\mathcal{T}^{(f,C)} + (\mathcal{T}^{(f,s)} - \mathcal{T}^{(f,C)}) e^{-|\dot{q}/\dot{q}^{(s)}|^{\delta^{(s)}}} \right), \quad (3.4)$$

where $\dot{q}^{(s)}$ is known as the Stribeck velocity, which indicates the velocity range in which the Stribeck effect occurs. According to Bo and Pavlescu (1982) the empirical exponent $\delta^{(s)}$ ranges from 0.5 to 1 for different material combinations.

Armstrong-Hélouvry (1991) adopted this Stribeck model and added the viscous term $c^{(v)}\dot{q}$:

$$\mathcal{T}^{(f)} = \text{sign}(\dot{q}) \left(\mathcal{T}^{(f,C)} + (\mathcal{T}^{(f,s)} - \mathcal{T}^{(f,C)}) e^{-|\dot{q}/\dot{q}^{(s)}|^{\delta^{(s)}}} \right) + c^{(v)}\dot{q}. \quad (3.5)$$

This friction model has been applied by many authors, e.g. Canudas De Wit et al. (1995); Olsson et al. (1998); Swevers et al. (2000); Hensen et al. (2002), for the modelling of sliding friction in robotic systems. Consequently, it is logical to investigate the applicability of this model to the modelling of joint friction in the Stäubli RX90B robot. In order to use the model, the values of the five unknown parameters, $\mathcal{T}^{(f,C)}$, $\mathcal{T}^{(f,s)}$, $\dot{q}^{(s)}$, $\delta^{(s)}$ and $c^{(v)}$, need to be determined experimentally for each joint.

3.2.2 Stribeck curve measurement

In order to evaluate the applicability of the friction model presented in equation (3.5), Stribeck curve measurements of the friction behaviour of the first joint of the Stäubli RX90B are carried out. The robot's first joint is moved with a trapezoidal velocity profile at different velocities. Experimentally, it appears that the friction torque also depends on the temperature of the joints and the joint angle, for example. To have an

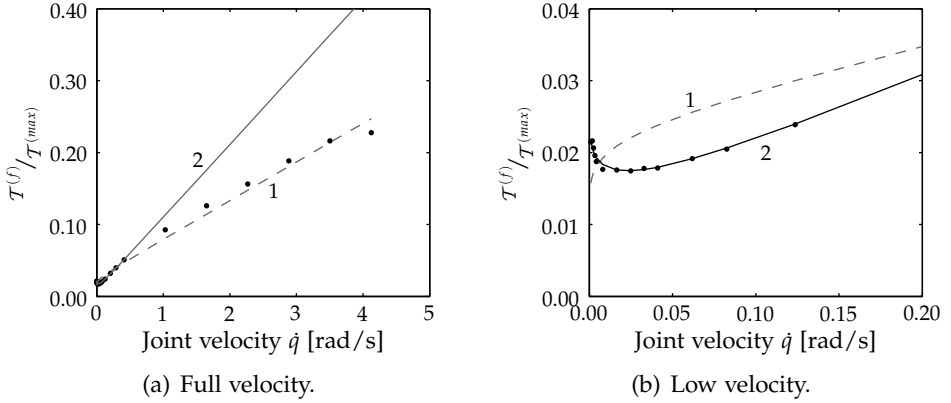


Figure 3.3: Stribeck curve for joint 1, where the dots (\bullet) denote the velocities at which the measurements were carried out. Note the nonlinear viscous behaviour at high velocity. Model 1 (—) is estimated in the full range whereas model 2 (—) is estimated in the range from 0 to 0.5 rad/s.

identical temperature during the experiments an initial warmup motion is executed before the actual measurements are done. The influence of the position and noise are minimised by averaging the measured joint torques during the constant velocity part of a trapezoidal velocity profile. The joint torques are plotted as a function of the joint velocity \dot{q} , see figures 3.3. The joint torque is normalised with the maximum joint torque. The Stribeck effect is clearly visible in the detailed figure 3.3(b). Note that the Stribeck velocity parameter $\dot{q}^{(s)}$ does not necessarily coincide with the joint velocity where the friction torque has its minimum.

The friction model is a nonlinear function of two of the unknown parameters, namely $\dot{q}^{(s)}$ and $\delta^{(s)}$. In order to estimate all five parameters at once, one has to rely on nonlinear optimisation techniques. It is commonly known that nonlinear optimisation techniques may lead to local optima in which non-physical parameter values are found. nonlinear optimisation techniques can be applied successfully in cases wherein the model agrees with the observed behaviour combined with a proper first estimate of the parameter values.

To prevent difficulties with nonlinear estimation techniques, a linear least squares optimisation technique is used to obtain the values for parameters $\mathcal{T}^{(f,C)}$, $\mathcal{T}^{(f,s)}$ and $c^{(v)}$ which are linear in the model. Values for

the parameters $\dot{q}^{(s)}$ and $\delta^{(s)}$ are selected manually and are assumed to be constant. Using this method, the parameters are identified in three steps. In the first step, the parameters for the Stribeck effect $\dot{q}^{(s)}$ and $\delta^{(s)}$ are given a reasonable value. In step two, the remaining model parameters $\mathbf{p}^{(f)} = [\mathcal{T}^{(f,s)} \quad \mathcal{T}^{(f,c)} \quad c^{(v)}]^T$ are estimated with a linear least square optimisation, which implies minimising the ℓ^2 -norm

$$\hat{\mathbf{p}}^{(f)} = \arg \min_{\mathbf{p}^{(f)}} \left\| \mathcal{T}^{(f)} - \mathbf{A}^{(f)} \mathbf{p}^{(f)} \right\|_2^2, \quad (3.6)$$

where $\mathcal{T}^{(f)} = [\mathcal{T}_1^{(f)} \quad \dots \quad \mathcal{T}_n^{(f)}]^T$ is the vector of measured friction torques and matrix $\mathbf{A}^{(f)}$ is defined as

$$\mathbf{A}^{(f)} = \begin{bmatrix} e^{-|\dot{q}_1/\dot{q}^{(s)}|^{\delta^{(s)}}} & 1 - e^{-|\dot{q}_1/\dot{q}^{(s)}|^{\delta^{(s)}}} & \dot{q}_1 \\ \vdots & \vdots & \vdots \\ e^{-|\dot{q}_n/\dot{q}^{(s)}|^{\delta^{(s)}}} & 1 - e^{-|\dot{q}_n/\dot{q}^{(s)}|^{\delta^{(s)}}} & \dot{q}_n \end{bmatrix}, \quad (3.7)$$

for n measured velocity values. The least squares estimates $\hat{\mathbf{p}}^{(f)}$ from equation (3.6) can be found by setting the partial derivative of the right hand side with respect to $\mathbf{p}^{(f)}$ at zero, which yields the so-called *normal equations*:

$$\mathbf{A}^{(f)T} (\mathbf{A}^{(f)} \hat{\mathbf{p}}^{(f)} - \mathcal{T}^{(f)}) = \mathbf{0}. \quad (3.8)$$

Solving the normal equations leads to

$$\hat{\mathbf{p}}^{(f)} = (\mathbf{A}^{(f)T} \mathbf{A}^{(f)})^{-1} \mathbf{A}^{(f)T} \mathcal{T}^{(f)}. \quad (3.9)$$

Note that $(\mathbf{A}^{(f)T} \mathbf{A}^{(f)})^{-1}$ only exists if $\mathbf{A}^{(f)}$ has full rank, which is the case for the optimisation problem at hand. Solving linear least squares problems will be discussed in detail in section 4.3.

The last and third step is to fine-tune the manually chosen values for $\delta^{(s)}$ and $\dot{q}^{(s)}$. This is an iterative process wherein the chosen values are changed slightly before the second step is repeated. By inspection of the fit between the modelled Stribeck curve and the measured Stribeck curve the values $\delta^{(s)} = 0.33$ and $\dot{q}^{(s)} = 0.024$ rad/s are obtained.

Using this technique, two different parameter sets are estimated; one for the full range from 0 to 4 rad/s and one for a low velocity range

from 0 to 0.5 rad/s. As can be observed from figure 3.3(a), models 1 and 2 show different behaviour for the low velocities (below 0.5 rad/s) and high velocities (above 0.5 rad/s) range.

Model 1 is estimated for the full velocity range and shows better performance at higher velocities. The low velocity behaviour is clearly not modelled correctly, because a value for the static friction torque has been found which is lower than the value for the Coulomb friction. This is caused by the fact that, for higher velocities, a lower viscous friction parameter shows a better fit. The mismatch for the viscous friction at low velocity is compensated by a negative Stribeck effect.

Model 2, on the other hand, proves to be quite accurate for the low velocity range and the Stribeck effect is described accurately. However, the extrapolation into the high velocity range is now poor. It appears that linear viscous behaviour of the model in equation (3.5) does not correspond with the actual viscous behaviour of the robot joint.

From the fact that a poor fit is obtained, it can be concluded that the model is not capable of describing friction phenomena for the full velocity range in the sliding regime. The friction model can be improved ad hoc by including additional (nonlinear) terms with extra parameters (Grotjahn, 2003). However, the physical meaning of such modifications is unclear. Furthermore, an increase in the number of model parameters does not necessarily improve the consistency of the parameter fit and may lead to over-fit.

Experiments have shown that the magnitude of the friction torque significantly changes due to temperature variations on the robot joints. Therefore, it is essential that the temperature dependent friction parameters are also included in the parameter set of the identification procedure for the inertia parameters, see chapter 4. With this in mind, the friction model needs to be able to accurately describe the actual friction behaviour of the robot joints. An incorrect friction model will lead to friction modelling errors which then give rise to large errors in the inertia parameter estimation. Furthermore, it is desired that the friction model is parameterised in such a way that it is physically sound and that it has a minimal number of parameters.

Lubricated bearings and gears in the robot joints are accompanied by rolling–sliding contacts between many surfaces. Therefore, a new friction model will be developed in the remainder of this chapter that is based on an analysis of the physical behaviour of two lubricated surfaces in a rolling-sliding contact.

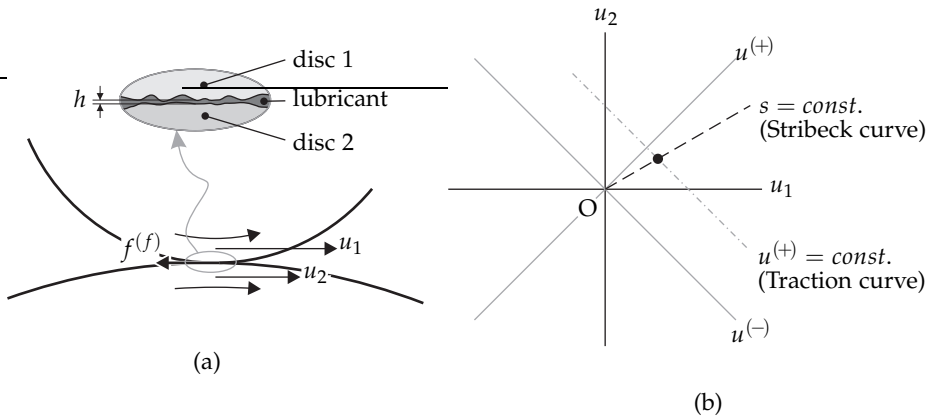


Figure 3.4: Two lubricated discs in a rolling–sliding contact (a) and the velocity diagram (b) in which the velocity state (•) of a lubricated contact can be indicated (Gelinck, 1999).

3.3 Friction modelling at contact level

In this section, the friction phenomena of a single lubricated contact are studied. On system level, the friction is accounted for as a torque $\mathcal{T}^{(f)}$. On contact level, it is more convenient to consider friction as a force $f^{(f)}$. Analogously, the surface velocity u is considered instead of the joint velocity \dot{q} .

The main components of a robot joint are bearings and gears. In tribology, friction inside gears and bearings is often represented by two lubricated discs in a rolling–sliding contact (Dowson and Higginson, 1977; Bhushan, 1999). The motivation for this representation is that friction in both the roller–raceway contact in roller bearings and the contact between two teeth in a helical or spur gear wheel pair may be represented by the friction behaviour of two lubricated discs in a rolling–sliding contact.

3.3.1 Two lubricated discs in a rolling–sliding contact

In figure 3.4(a), an illustration of two lubricated discs in a rolling–sliding contact is given. The friction force between both discs is defined as $f^{(f)}$. The surface velocities of both discs are defined as u_1 and u_2 , respectively. The velocity state of the lubricated contact can be expressed as a function of these surface velocities. It is, however, more convenient to express the

velocity state of the contact as a function of the sliding velocity and the sum velocity, see the velocity diagram in figure 3.4(b). The sliding velocity is the difference between both velocities

$$u^{(-)} = u_1 - u_2 \quad (3.10)$$

and the sum velocity $u^{(+)}$ is defined as

$$u^{(+)} = u_1 + u_2. \quad (3.11)$$

Another frequently used quantity to express the velocity state is the slip ratio s , which is defined as the ratio between the sum and the sliding velocity

$$s = \frac{u^{(-)}}{u^{(+)}}. \quad (3.12)$$

With these definitions, three typical situations for the velocity state can be distinguished:

- i. Perfect rolling. Both velocities, u_1 and u_2 , are equal in magnitude and direction. Then the sliding velocity $u^{(-)}$ equals zero and, consequently, there is zero slip. This velocity state is indicated by the $u^{(+)}$ -line.
- ii. Full sliding. Both velocities, u_1 and u_2 , are equal in magnitude and opposite in direction. Then the sum velocity $u^{(+)}$ equals zero, resulting in infinite slip. This velocity state is indicated by the $u^{(-)}$ -line.
- iii. Constant slip. The ratio s between the sum and sliding velocity remains constant. This velocity state is indicated by the dashed line in figure 3.4(b), for example. In fact, it may be any line that crosses the origin O.

Next, the friction behaviour will be considered in terms of the above mentioned velocity states. In figure 3.4(b) two typical states are depicted, the constant sum velocity state and the constant slip ratio state. These states are represented by the traction curve and the Stribeck curve, respectively.

In section 3.4 it will be demonstrated that the frictional behaviour of contacts inside gear transmissions and roller bearings may be characterised by a constant slip ratio and therefore it is logical to look at the Stribeck behaviour for modelling the friction forces. Since the Stribeck

curve is defined for a constant slip ratio, the curve is plotted as a function of the sum velocity $u^{(+)}$. Schipper (1988) defines a lubrication number

$$\mathcal{L} = \frac{\eta u^{(+)}}{p_{av} R_a}, \quad (3.13)$$

where η is the inlet viscosity, p_{av} is the average pressure and R_a is the combined surface roughness. Plotting the Stribeck curve as a function of this lubrication number \mathcal{L} yields a so-called generalised Stribeck curve, see figure 3.5.

The Stribeck curve is characterised by three lubrication regimes: Boundary Lubrication (BL), Mixed Lubrication (ML) and Elasto-Hydrodynamic Lubrication (EHL). In figure 3.5, these lubrication regimes are indicated in a typical Stribeck curve for an arbitrary lubricated contact. In the BL regime, at very low velocity, the friction force is mainly caused by the contact between the surface asperities. As the velocity increases, the lubricant film grows and less asperities are in contact, resulting in a reduction of the friction force caused by the surface summits. On the other hand, viscous friction caused by the lubricant is increasing. This regime is known as the ML regime. Finally, in the EHL regime, the lubricant film has grown to such an extent that the surfaces are fully separated. The friction force is the force needed to shear the lubricant film. In figure 3.5 three different Stribeck curves are plotted at logarithmic scales. The curves range from Newtonian behaviour to full non-Newtonian behaviour of the lubricant. It appears that the rheological properties of the lubricant play a central role with regard to the friction behaviour in the EHL regime.

3.3.2 Friction forces in the lubrication regimes

In the boundary lubrication regime, the friction force is mainly determined by the friction force due to the asperity contacts, denoted by $f^{(a)}$. On the other hand, in the elasto-hydrodynamic lubrication regime, the friction force $f^{(v)}$ due to the viscosity of the lubricating film is dominant. In the mixed lubrication regime both the asperity contacts and the lubricant viscosity determine the total friction force.

With this in mind, the total friction force $f^{(f)}$ is assumed to be the sum of the friction force due to the asperity contacts $f^{(a)}$ and a friction force due to hydrodynamic component $f^{(v)}$ (Gelinck and Schipper, 2000). This

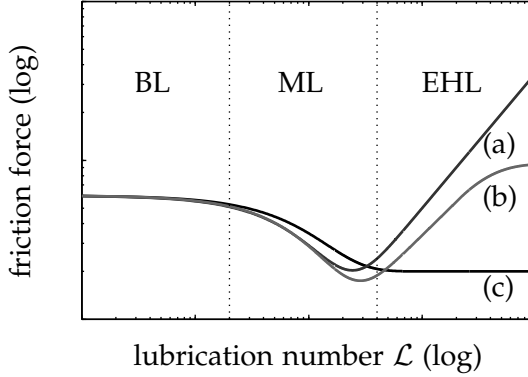


Figure 3.5: A typical Stribeck curve for an arbitrary lubricated contact: the transition from boundary lubrication (BL) via mixed lubrication (ML) to elasto-hydrodynamic lubrication (EHL) as a function of the lubrication number \mathcal{L} . Note that the curves are plotted at logarithmic scales. Curve (a) shows typical Newtonian behaviour of the lubricant at high velocity. In curve (b) the lubricant is mainly Newtonian, but at high velocity the lubricant shows non-Newtonian behaviour. Curve (c) corresponds with full non-Newtonian behaviour.

leads to the expression for the total friction force

$$\begin{aligned}
 f^{(f)} &= f^{(a)} + f^{(v)} \\
 &= \sum_{i=1}^{n^{(a)}} \iint_{A_i^{(a)}} \tau_i^{(a)} dA_i^{(a)} + \iint_{A^{(H)}} \tau^{(s)} dA^{(H)}, \quad (3.14)
 \end{aligned}$$

where $n^{(a)}$ is the number of asperities in contact, $A_i^{(a)}$ denotes the area of contact of a single asperity i , $\tau_i^{(a)}$ represents the shear stress at the asperity contact i , $A^{(H)}$ is the effective area of contact of the hydrodynamic component and $\tau^{(s)}$ is the shear stress of the hydrodynamic component. In order to describe the total friction force, both the expressions for the friction force due to the asperity contacts $f^{(a)}$ and the friction force due to hydrodynamic component $f^{(v)}$ will be investigated in more detail in the next subsections.

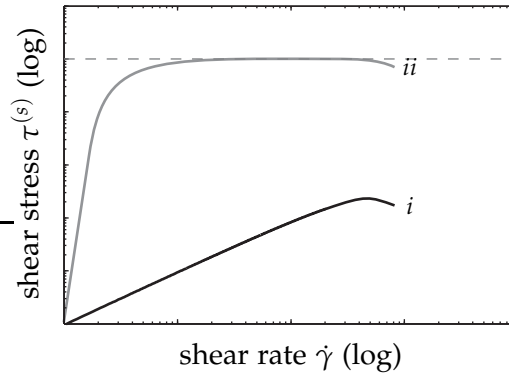


Figure 3.6: Traction curve: the shear stress as a function of the shear rate at constant sum velocity. Two typical curves for fluids which differ in their rheological behaviour are depicted. Note that at high slip ratios the friction force decreases as a function of the slip ratio due to shear heating of the fluid.

Friction force due to the hydrodynamic component

The force needed to shear a fluid film resembles the sliding friction between two lubricated surfaces. The assumption that a force is needed to shear a fluid film was first proposed by Sir Isaac Newton (1642-1727). Newton states that the shear stress $\tau^{(s)}$ is proportional to the shear rate $\dot{\gamma}$ in the film

$$\tau^{(s)} = \eta \dot{\gamma}, \quad (3.15)$$

where η is known as the viscosity. Lubricant behaviour is called Newtonian when the shear stress–shear rate relationship is according to equation (3.15) and consequently the lubricant has a viscosity which is shear rate independent.

Many lubricants, however, show non-Newtonian behaviour at increasing shear rates and show a limiting shear stress for high shear rates. This can be represented graphically in a so-called traction curve, see figure 3.6, where the different rheological behaviour of two lubricants is depicted (Evans, 1983). Curve *i* represents the Newtonian behaviour of the lubricant, according to equation (3.15). The second curve *ii* describes the full non-Newtonian behaviour of lubricants. At low slip ratios the friction behaviour is isothermal. At high slip ratios, however, the friction force decreases as a function of the slip ratio due to shear heating of the fluid.

In this thesis the effect of shear heating will not be included in the friction models. Note that for zero slip situations, i.e. in a pure rolling contact, the shear stress appears to be zero. However, due to the rolling motion there is still some pressure flow in the lubricant which gives rise to nonzero shear stress.

The Newtonian model of equation (3.15) will be used to model the linear viscous behaviour expressed by curve *i*. The model of Bair and Winer (1979a) is adopted to describe curve *ii*, the shear stress as a function of the shear rate for a full non-Newtonian fluid,

$$\tau^{(s)} = \tau_l^{(s)} \left(1 - e^{-\frac{\eta_0 \dot{\gamma}}{\tau_l^{(s)}}} \right), \quad (3.16)$$

where η_0 is the viscosity at reference temperature and pressure and $\tau_l^{(s)}$ is the limiting shear stress. Assuming that the sliding velocity $u^{(-)}$ is a continuous function of the height h of the lubricating film and that there is no slip at the interface between the fluid film and the solid surfaces, the shear rate $\dot{\gamma}$ in the lubricating film can be approximated by

$$\dot{\gamma} = \frac{u^{(-)}}{h}. \quad (3.17)$$

Equations (3.15) and (3.16) imply that the shear stress $\tau^{(s)}$ may be considered constant when the shear rate $\dot{\gamma}$ is given and the film thickness h is constant. Consequently, the friction force $f^{(v)}$ due to the hydrodynamic component can be approximated by considering a constant average film height h over a certain hydrodynamic area of contact $A^{(H)}$, yielding

$$f^{(v)} = \iint_{A^{(H)}} \tau^{(s)} dA^{(H)} \approx \tau^{(s)} A^{(H)}. \quad (3.18)$$

For the Newtonian case, substitution of equations (3.15) and (3.17) into equation (3.18), yields the following expression for the friction force due to the hydrodynamic component:

$$f^{(v)} = \eta A^{(H)} \frac{u^{(-)}}{h}. \quad (3.19)$$

For non-Newtonian situations, substitution of the equations (3.16) and (3.17) into equation (3.18) yields

$$f^{(v)} = A^{(H)} \tau_l^{(s)} \left(1 - e^{-\frac{\eta_0 u^{(-)}}{\tau_l^{(s)} h}} \right). \quad (3.20)$$

Inspection of these relationships show a dependency of the hydrodynamic friction force on the height h of the lubricating film. It appears that h strongly depends on the sum velocity $u^{(+)}$, as will be outlined hereafter in more detail.

Height of the lubricating film

The calculation of the lubricant film height has been studied intensively in Elasto–Hydrodynamic Lubrication (EHL) research (Grubin and Vinogradova, 1949; Crook, 1961; Dowson and Higginson, 1977; Dowson, 1995; Spikes, 1999). It has been found that the film height depends on six independent variables:

- R the radius of the roller pair,
- E the elastic modulus of a roller pair,
- η_0 the viscosity,
- $\alpha^{(l)}$ the pressure exponent of the lubricant;
 $\eta = \eta_0 e^{\alpha^{(l)} p}$, with pressure p ,
- w the load per unit width,
- $u^{(+)}$ the sum velocity.

The film height is then expressed as a function

$$\frac{h}{R} = f \left(\frac{w}{ER}, \frac{u^{(+)}\eta_0}{ER}, \alpha^{(l)} E \right), \quad (3.21)$$

where the above variables are grouped into four dimensionless parameters. These dimensionless parameters are:

$$\text{the relative film height} \quad H = \frac{h}{R}, \quad (3.22)$$

$$\text{the load parameter} \quad W = \frac{w}{ER}, \quad (3.23)$$

$$\text{the velocity parameter} \quad U = \frac{u^{(+)}\eta_0}{ER}, \quad (3.24)$$

$$\text{the material parameter} \quad G = \alpha^{(l)} E. \quad (3.25)$$

It has been found analytically by Dowson and Higginson (1977) that the minimum film thickness could fairly accurately be represented by

$$H_{\min} = \frac{1.6G^{0.6}U^{0.7}}{W^{0.13}}. \quad (3.26)$$

The equation shows that the influence of the material parameter G is quite large. However, G can be considered to be constant for a specific combination of materials and lubricant. Furthermore, it can be observed that the load parameter W only weakly influences the film height. The velocity parameter U is clearly the most significant parameter. From expression (3.26), there follows a proportionality between the lubricant film height and the sum velocity, expressed as

$$h \propto (u^{(+)})^{0.7}. \quad (3.27)$$

However, according to experimental results by Crook (1961), the lubricant film height shows a proportionality to the sum velocity $u^{(+)}$ given by

$$h \propto (u^{(+)})^{0.5}. \quad (3.28)$$

This indicates that the power in which the film height relates to the sum velocity does not have an unique value, but varies between 0.5 and 0.7 depending on the details of the specific contact. Therefore, its precise value has to be determined for the specific application at hand.

With these observations, it is possible to express the film height h as a function of the sum velocity $u^{(+)}$ as

$$h = h^{(s)} \left(\frac{u^{(+)}}{u^{(s)}} \right)^\delta, \quad (3.29)$$

where the proportionality constant $h^{(s)}$ represents the reference height of the lubricant film, which is a function of the load parameter W , the material parameter G and the radius R . In order to keep proper dimension, a scaling velocity $u^{(s)}$ is introduced, which relates to the lubricant viscosity η , the elastic modulus E and the radius R . From equations (3.27) and (3.28) it follows that the power δ is expected to range from 0.5 to 0.7.

With the simplified expression for the height of the lubricant film and the equations for the viscous friction forces derived in section 3.3.2, the viscous friction forces $f^{(v)}$ can be described as a function of both the sum velocity $u^{(+)}$ and the sliding velocity $u^{(-)}$. Substitution of the expression for the film height, equation (3.29), into equation (3.19) yields

$$f^{(v)} = \frac{\eta A^{(H)} u^{(-)}}{h^{(s)}} \left(\frac{u^{(s)}}{u^{(+)}} \right)^\delta, \quad (3.30)$$

which is the viscous friction force in the case of Newtonian behaviour of the lubricant.

Friction force due to asperity contacts

In this section, an equation for the friction force due to the asperity contacts in the boundary lubrication regime will be derived. The normal load acting on a lubricated contact is shared between the hydrodynamic component and the interacting asperities of the surfaces. Therefore, as the carrying capacity due to the hydrodynamic action increases as a function of the film height, the load carried by the asperities decreases.

Greenwood and Williamson (1966) have introduced an approach to model the contacts between the asperities which is based on the statistics of the surface roughness of the surfaces in contact. The height distribution of the surface summits can be considered Gaussian, but—according to Greenwood and Williamson (1966)—an exponential distribution proves to be a fair approximation for the uppermost 25% of the asperities of most surfaces. Using the exponential distribution has the advantage that a fairly simple expression for the number of asperities $n^{(a)}$ in contact can be used (Greenwood and Williamson, 1966). The expression is given by

$$n^{(a)} = d^{(a)} A^{(a)} e^{-\lambda^{(s)}}, \quad (3.31)$$

where $d^{(a)}$ is the asperity density and $A^{(a)}$ denotes the total area of contact. Exponent $\lambda^{(s)}$ is known as the separation which is the ratio between the film height h and the standard deviation $\sigma^{(s)}$ of the height distribution of the surface summits, defined as

$$\lambda^{(s)} = \frac{h}{\sigma^{(s)}}. \quad (3.32)$$

Using the lubricant film height given by equation (3.29), the separation can be written as a function of the sum velocity $u^{(+)}$

$$\lambda^{(s)} = \frac{h^{(s)}}{\sigma^{(s)}} \left(\frac{u^{(+)}}{u^{(s)}} \right)^\delta. \quad (3.33)$$

Note that the expression for the lubricant film height of equation (3.29) does not hold true for cases wherein the height of the lubricating film is in the order of the surface roughness. The separation expressed in equation (3.33) predicts a zero separation for a zero sum velocity, where in fact the separation will approach a constant value towards zero sum velocity, as there will always be some lubricant between the asperities.

The total friction force due to all $n^{(a)}$ asperities can be approximated as

$$f^{(a)} = \sum_{i=1}^{n^{(a)}} \iint_{A_i^{(a)}} \tau_i^{(a)} dA_i^{(a)} \approx n^{(a)} f^{(a,BL)}, \quad (3.34)$$

where $f^{(a,BL)}$ is the average friction force due to a single asperity in the BL regime. Substitution of expression (3.31) for the number of asperities and the separation given by equation (3.33) into equation (3.34) yields the expression for the friction force $f^{(a)}$ due to the asperity contacts as a function of the sum velocity

$$f^{(a)} = f^{(a,BL)} d^{(a)} A^{(a)} \exp\left(-\frac{h^{(s)}}{\sigma^{(s)}} \left(\frac{u^{(+)}}{u^{(s)}}\right)^\delta\right). \quad (3.35)$$

Note the correspondence of equation (3.35) with the model of Bo and Pavelescu (1982), as in equation (3.4) from section 3.2.1 with $\mathcal{T}^{(f,C)} = 0$.

According to Greenwood and Williamson (1966), an exact proportionality between the load and the number of asperities in contact exists. This implies that the separation is a function of the load, which is, at first sight, contradictory to the statements in section 3.3.2, where the load dependency of the film height and thus the separation is minimal. This contrast can be explained by the fact that the equations for the film height from section 3.3.2 only apply to the elasto-hydrodynamic lubrication regime. In the boundary lubrication regime, the lubricant film is not completely developed and the friction force is still largely dependent on the contact load. However, for components running in the ML and EHL regimes, such as helical or spur gears and prestressed roller bearings, the effect of load dependency within the BL regime is small. For contacts running mainly in the BL and the ML regimes, such as worm gears, the influence of the magnitude of the transmitted force on the friction force in the BL regime might not be negligible, as will be shown in section 4.4.4.

3.4 Friction models of elementary components

In sections 3.3.2 and 3.3.2, expressions for the friction force due to lubricant viscosity and due to the asperities for a lubricated contact between two rolling–sliding discs have been presented. In this section, these expressions are applied to describe the friction forces arising in two elementary components; a helical gear-pair and a prestressed roller bearing.

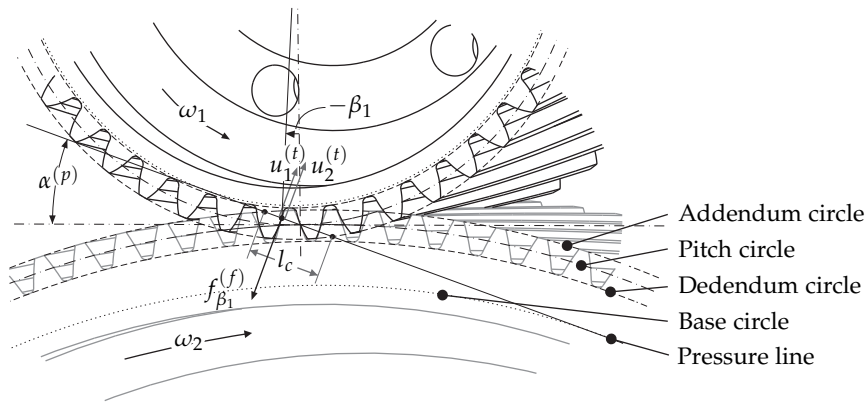


Figure 3.7: A helical gear pair.

3.4.1 Friction model of a helical gear pair

In figure 3.7 a helical gear pair is depicted. Here, the upper gear wheel drives the lower gear wheel. The figure shows that several teeth are in contact with each other at the same instance in a gear pair. Furthermore, since the gear pair is of the helical type, a single tooth remains in contact over the full width of the gear wheel along the path of contact l_c on the pressure line.

The two surface velocities $u_1^{(t)}$ and $u_2^{(t)}$ are depicted in the teeth contact illustrated in the figure 3.7. At the point where the pressure line crosses the pitch circle, the velocities $u_1^{(t)}$ and $u_2^{(t)}$ are equal in magnitude which results in a pure rolling motion ($u^{(-)} = 0$). However, at all other points $\beta_1 \neq 0$. Thus, the velocities are not equal in magnitude, leading to a nonzero sliding velocity. At the moment of interconnection of the teeth, the surface velocity $u_1^{(t)}$ associated with the driving gear is lower in magnitude as compared to $u_2^{(t)}$. Towards the pitch circle, they become gradually equal in magnitude. After the moment of pure rolling, $u_1^{(t)}$ becomes larger in magnitude in comparison with $u_2^{(t)}$. Consequently, there is a large part during the interconnecting phase where there is a nonzero sliding velocity. Considering the exact analytical expressions for both the sum and the sliding velocities will lead to a complex friction model. However, it is possible to simplify the expressions for the velocities, see

Appendix A, in such a way that a practical friction model can be derived without loss of generality.

The angular velocity ω_1 of the driving gear is taken as being equal to the angular velocity of the servo motor, so that $\omega_1 = n^{(g)}\dot{q}$, where $n^{(g)}$ is the gear ratio of the complete transmission. Using the velocity expression (A.8) as is derived in Appendix A, the sum velocity $u^{(+)}$ can then be approximated as

$$u^{(+)} = r^{(g)}\dot{q}, \quad (3.36)$$

where $r^{(g)}$ represents a kinematic factor which is given by

$$r^{(g)} = n^{(g)}R_1^{(p)} \sin(\alpha^{(p)}), \quad (3.37)$$

with $R_1^{(p)}$ the radius of the pitch circle and pressure angle $\alpha^{(p)}$. Using the average slip ratio s_0 from equation (A.11) in Appendix A, the expression for the sliding velocity becomes

$$\bar{u}^{(-)} = s_0 r^{(g)}\dot{q}. \quad (3.38)$$

Application of the average slip ratio s_0 implies that the viscous friction force inside gear transmissions may be approximated by a Stribeck curve.

The helical gear pair inside the joint transmission is operating at the servo side of the transmission at high velocities and relatively small loads. Combined with the fact that the contacts between the gear teeth are line contacts, the contact pressures in the helical gear pair are considered to be sufficiently low in order to allow the assumption that the lubricant behaviour will be Newtonian. According to equation (3.14), the friction force is taken as the sum of the friction force due to the asperity contacts and the (averaged) viscous friction force. Summation of the viscous friction force for the Newtonian case, equation (3.30), and the friction force due to the asperities, equation (3.35), leads to the combined (averaged) friction force for two teeth in contact

$$\begin{aligned} \bar{f}^{(f)} &= f^{(a)} + \bar{f}^{(v)} \\ &= f^{(a,BL)} d^{(a)} A^{(a)} \exp\left(-\frac{h^{(s)}}{\sigma^{(s)}} \left(\frac{u^{(+)}}{u^{(s)}}\right)^\delta\right) + \frac{\eta A^{(H)} \bar{u}^{(-)}}{h^{(s)}} \left(\frac{u^{(s)}}{u^{(+)}}\right)^\delta. \end{aligned} \quad (3.39)$$

The total friction torque $\mathcal{T}^{(f)}$ can be derived by multiplying the averaged friction force $\bar{f}^{(f)}$ with the radius of the base circle $R_1^{(b)}$ and the

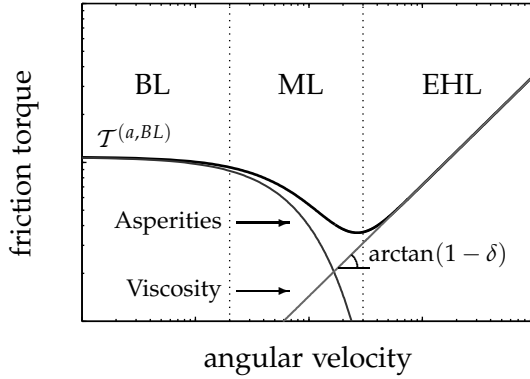


Figure 3.8: A typical Stribeck curve for a helical gear pair. The contributions to the friction torque from the asperity contacts and the hydrodynamic component are depicted separately.

number of teeth k in contact. Accordingly, substitution of equations (3.37), (3.36) and (3.38) into equation (3.39) results in the friction model of a helical gear pair

$$\mathcal{T}^{(f)} = \mathcal{T}^{(a)} + \mathcal{T}^{(v)} = \underbrace{\mathcal{T}^{(a,BL)} e^{-(\dot{q}/\dot{q}^{(s)})^\delta}}_{\text{asperities}} + \underbrace{c^{(v)} \dot{q}^{(1-\delta)}}_{\text{viscosity}}, \quad (3.40)$$

with the parameters

$$\mathcal{T}^{(a,BL)} = kR_1^{(b)} f^{(a,BL)} d^{(a)} A^{(a)}, \quad (3.41a)$$

$$\dot{q}^{(s)} = \frac{u^{(s)}}{r^{(g)}} \left(\frac{\sigma^{(s)}}{h^{(s)}} \right)^{1/\delta}, \quad (3.41b)$$

$$c^{(v)} = \frac{kR_1^{(b)} s_0 \eta A^{(H)}}{h^{(s)}} \left(\frac{u^{(s)}}{r^{(g)}} \right)^\delta. \quad (3.41c)$$

A typical Stribeck curve for a helical gear pair, represented by the model in equation (3.40) with an arbitrary parameter set, is illustrated in figure 3.8. It clearly shows that the asperity contacts are responsible for the friction force in the BL regime and that the hydrodynamic component dominates the friction force in the EHL regime.

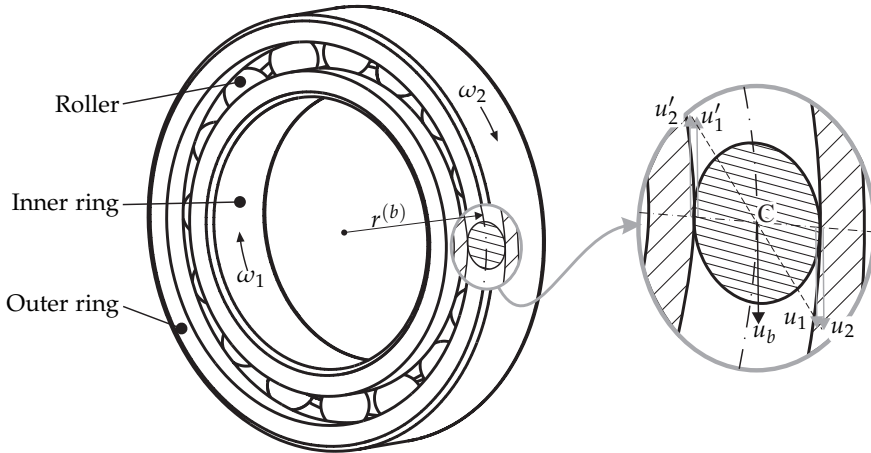


Figure 3.9: Schematic representation of a roller bearing.

3.4.2 Friction model of a prestressed roller bearing

In figure 3.9, a roller bearing is depicted. The bearing is an assembly of two concentric circular raceways, the inner ring and the outer ring. For elimination of backlash, the bearings in the robot joints are prestressed. The difference in velocity between the inner ring and the outer ring is covered by the rolling motion of the rollers in between these raceways. Small differences between the velocities (u_1, u_2) , and also between the velocities (u'_1, u'_2) cause friction forces in the contact surfaces between a roller and both the inner and outer rings. These friction forces form a torque that sets the roller in motion. This process, known as traction, was introduced in section 3.3.1. Since the bearing is highly prestressed, it is assumed that the lubricant behaviour will be non-Newtonian and it will start to behave like a solid, even for small slip ratios (Bair and Winer, 1979b).

The friction force can be computed as the sum of the viscous friction and the friction force caused by the asperities. Due to the non-Newtonian behaviour of the lubricant in the bearing, equation (3.20) is used to compute the viscous friction force.

Equation (3.35) will account for the friction force due to the asperity contact. Combining these equations yields an expression for the friction

force in a single contact between a roller and a raceway inside a bearing

$$\begin{aligned} f^{(f)} &= f^{(a)} + f^{(v)} \\ &= f^{(a,BL)} d^{(a)} A^{(a)} \exp\left(-\frac{h^{(s)}}{\sigma^{(s)}} \left(\frac{u^{(+)}}{u^{(s)}}\right)^\delta\right) + A^{(H)} \tau_l^{(s)} \left(1 - e^{-\frac{\eta_0 u^{(-)}}{\tau_l^{(s)} h}}\right). \end{aligned} \quad (3.42)$$

The velocity u_b of a rolling element, see figure 3.9, is expressed as

$$u_b = \frac{r^{(b)}}{2} (\omega_1 - \omega_2), \quad (3.43)$$

where $r^{(b)}$ is the average raceway radius and ω_1 and ω_2 denote the angular velocity of the inner and outer raceway, respectively. By assuming a constant—but very small—average slip ratio s_0 , the local surface velocities become respectively

$$u_1 = u_b, \quad (3.44a)$$

$$u_2 = (1 - s_0)u_b. \quad (3.44b)$$

With $\dot{q} = \omega_1 - \omega_2$, the velocities $u^{(+)}$ and $u^{(-)}$ can be expressed as follows

$$u^{(+)} \approx r^{(b)} \dot{q}, \quad (3.45a)$$

$$u^{(-)} \approx r^{(b)} s_0 \dot{q}. \quad (3.45b)$$

The total friction torque $\mathcal{T}^{(f)}$ generated by a prestressed roller bearing is considered as the sum of all torques generated by the friction forces at all roller–raceway contacts, which is acquired by multiplying the friction force in equation (3.42) with radius $r^{(b)}$ and the number of rolling elements k . Substitution of the velocity expressions (3.45) into equation (3.42) yields the expression for the friction torque of a prestressed roller bearing

$$\mathcal{T}_{bearing}^{(f)} = \mathcal{T}^{(a)} + \mathcal{T}^{(l)} = \underbrace{\mathcal{T}^{(a,BL)} e^{-(\dot{q}/\dot{q}^{(s)})^\delta}}_{\text{asperities}} + \underbrace{\mathcal{T}^{(v,l)} (1 - e^{-\dot{q}/\dot{q}^{(l)}})}_{\text{viscosity}}, \quad (3.46)$$

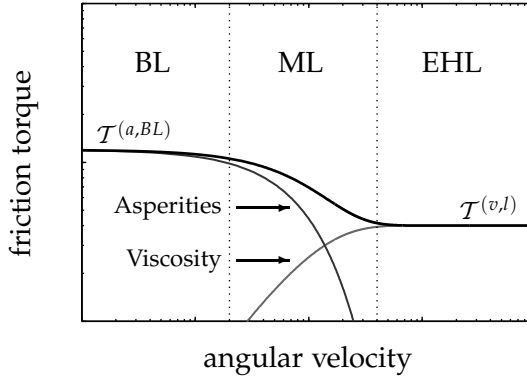


Figure 3.10: A typical Stribeck curve for a prestressed roller bearing. Note that the friction torque decreases from the asperity friction torque $\mathcal{T}^{(a,BL)}$ towards the (limiting shear stress) viscous friction torque $\mathcal{T}^{(v,l)}$.

with the parameters

$$\mathcal{T}^{(a,BL)} = r^{(b)} k_f^{(a,BL)} d^{(a)} A^{(a)}, \quad (3.47a)$$

$$\dot{q}^{(s)} = \frac{u^{(s)}}{r^{(b)}} \left(\frac{\sigma^{(s)}}{h^{(s)}} \right)^{1/\delta}, \quad (3.47b)$$

$$\mathcal{T}^{(v,l)} = r k \tau_l^{(s)} A^{(H)}, \quad (3.47c)$$

$$\dot{q}^{(l)} = \frac{\tau_l^{(s)} h_l}{r s_0 \eta_0}. \quad (3.47d)$$

A typical Stribeck curve for a prestressed roller bearing represented by the model in equation (3.46) is illustrated in figure 3.10. The curves for the friction torque generated by the asperity contacts and the friction torque due to lubricant viscosity are also plotted separately. Note that the friction torque decreases from the asperity friction torque $\mathcal{T}^{(a,BL)}$ towards the (limiting shear stress) viscous friction torque $\mathcal{T}^{(v,l)}$.

The film height h is not included as a function of the rolling velocity in the expression for the viscous friction force in equation (3.46). This simplification is introduced since the dependency of the film height on the

rolling velocity only influences the shape of the exponential function associated with the non-Newtonian behaviour. Furthermore, in the velocity region where the exponential function has an effect, the friction torque is dominated by the friction torque due to the asperity contacts. Therefore, the film height h for the viscous part can in this case be approximated by a constant film height h_l .

In sections 3.4.1 and 3.4.2, friction models for both a gear pair and a prestressed roller bearing have been derived. The models are based on physical models from tribology literature in which elementary variables such as lubricant viscosity, contact topology and material properties have been taken into account. These elementary variables have been combined into a new set of parameters, some of which are constant for a specific contact, while others may change during operation, e.g. due to temperature variations. In the next section, the two models will be used to construct the joint friction models for the Stäubli RX90B.

3.5 The joint friction model

The next step is to combine the models derived in the previous section into friction models that account for the friction that arises in a single robot joint. The first four robot joints are constructed in a similar way according to the schematic representation given in figure 3.1(a). The joints include a helical gear pair, a cycloidal transmission and a joint bearing support (Gerat, 1994). The remaining two joints in the robot's wrist, see figure 3.1(b), are driven via a worm and wheel gear (Gerat and Palau, 1998) and joint six includes a spiral bevel gear. Naturally, the wrist assembly is equipped with roller bearings as well.

The joint friction model can be considered as a combination of the friction models associated with the joint transmission components. However, summation of all sub-models will lead to a large friction model which includes many parameters. Instead, only the friction characteristics of the components will be evaluated and only the most significant effects will be taken into account. The contributions to the friction torques of elements such as seals are assumed to be less significant and are not taken into account. First, the friction model for the joints 1 through 4 is discussed and next, the friction model for the wrist assembly is dealt with.

3.5.1 Friction model for the first four robot joints

The first four robot joints are constructed according to the schematic representation given in figure 3.1(a). The assembly contains three main components: a helical gear pair, a cycloidal transmission and the joint bearings. The joint bearings are highly prestressed and therefore it is expected that the bearings are responsible for the main part of the asperity friction torque. The viscous friction torque of the bearings, however, is much lower than its asperity friction torque, as can be observed from the Stribeck curve of the roller bearing, see figure 3.10. Taking into account that the helical gear pair in the joint is operating at a high angular velocity due to the high transmission ratio, it can be expected that its viscous friction torque will be dominant with respect to the viscous friction torque of the bearing. The cycloidal gears are operating at a low angular velocity and are prestressed as well. This will result in a small viscous friction torque in comparison with the helical gear pair. Furthermore, the friction behaviour at low velocity will be similar to the asperity friction behaviour of a roller bearing. The final joint friction model will be a combination of the asperity part of the model of a roller bearing, equation (3.46), and the viscous part of the model of a helical gear pair, equation (3.40). This then yields the combined friction model for joint j :

$$\mathcal{T}_j^{(f)} = \mathcal{T}_j^{(a,BL)} e^{-\left(\dot{q}_j/\dot{q}_j^{(s)}\right)^{\delta_j^{(a)}}} + c_j^{(v)} \dot{q}_j^{(1-\delta_j^{(v)})}. \quad (3.48)$$

Note the different values for $\delta_j^{(a)}$ and $\delta_j^{(v)}$ as the friction torque from the asperities and the viscous friction torque are generated at different elements and may therefore show a different film thickness–velocity behaviour.

For each joint j , there are five unknown parameters; the asperity friction torque $\mathcal{T}_j^{(a,BL)}$, the Stribeck velocity $\dot{q}_j^{(s)}$, the Stribeck velocity power $\delta_j^{(a)}$, the viscous friction coefficient $c_j^{(v)}$ and the viscous friction power $\delta_j^{(v)}$. The parameters $\delta_j^{(a)}$, $\delta_j^{(v)}$ and the Stribeck velocity $\dot{q}_j^{(s)}$ depend on the configuration of the friction contacts. Since the configuration of these contacts is assumed to be time-invariant, these parameters are assumed to be constant. The viscous friction coefficient $c_j^{(v)}$ depends on the lubricant viscosity η and, as a result, it depends on temperature. The values for all unknown parameters will be obtained by means of experimental

identification. It appears that the static asperity friction torque $\mathcal{T}_j^{(a,BL)}$ depends only slightly on temperature, see section 3.7.

Comparing the friction model in equation (3.48) with the “classical” friction model of Armstrong-Hélouvry (1991) as is presented in equation (3.5), two main differences can be noticed. The first difference is shown in the viscous friction part, where the new model shows a nonlinear velocity-viscous friction relation in terms of $c^{(v)}\dot{q}^{(1-\delta^{(v)})}$, as opposed to a linear velocity relation expressed by $c^{(v)}\dot{q}$. The second aspect in which the new model differs from the standard model is that the Coulomb friction term has disappeared. This is due to the fact that the new friction model is derived for lubricated surfaces and that Coulomb friction generally is associated with dry contacts.

3.5.2 Friction model of the wrist assembly

The wrist assembly includes both the fifth and the sixth joint of the robot. As the servos are mounted inside the fourth link of the robot, a gear transmission transfers the motion from servo 6 through the fifth joint to joint 6. This causes a kinematic coupling between motor 5 and joint 6, see figure 3.11. The angular velocity of servo 5 is directly proportional to \dot{q}_5 . However, the angular velocity of servo 6 is related to the difference between \dot{q}_5 and \dot{q}_6 . Hence an extra friction model is needed. The velocity \dot{q}_7 associated with the extra friction model is defined as

$$\dot{q}_7 = \dot{q}_5 + \dot{q}_6. \quad (3.49)$$

In figure 3.11, the three friction models are indicated by a , b and c and represent the friction models of the worm and wheel gear of servo 5, the joint bearing of joint 6 and the worm and wheel gear of servo 6, respectively. The friction models a , b and c for the whole wrist assembly model are given by

$$\mathcal{T}_a^{(f)} = \mathcal{T}_5^{(a,BL)} e^{-\left(\dot{q}_5/\dot{q}_5^{(s)}\right)^{\delta_5^{(a)}}} + c_5^{(v)} \dot{q}_5^{(1-\delta_5^{(v)})}, \quad (3.50a)$$

$$\mathcal{T}_b^{(f)} = \mathcal{T}_6^{(a,BL)} e^{-\left(\dot{q}_6/\dot{q}_6^{(s)}\right)^{\delta_6^{(a)}}} + \mathcal{T}_6^{(v,l)} (1 - e^{-\dot{q}_6/\dot{q}_6^{(l)}}), \quad (3.50b)$$

$$\mathcal{T}_c^{(f)} = \mathcal{T}_7^{(a,BL)} e^{-\left(\dot{q}_7/\dot{q}_7^{(s)}\right)^{\delta_7^{(a)}}} + c_7^{(v)} \dot{q}_7^{(1-\delta_7^{(v)})}. \quad (3.50c)$$

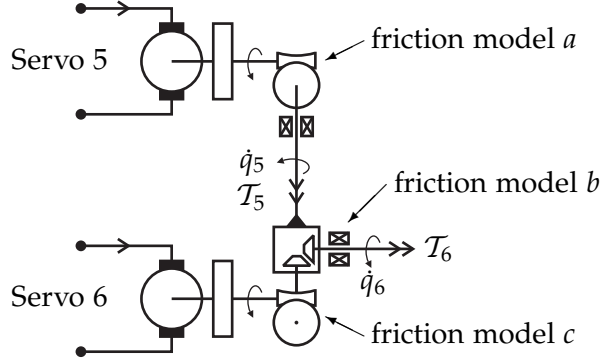


Figure 3.11: Schematic overview of the location of the friction models a , b and c in the wrist assembly.

The friction torques $\mathcal{T}_a^{(f)}$, $\mathcal{T}_b^{(f)}$ and $\mathcal{T}_c^{(f)}$ are transferred to friction torques at joint level as follows:

$$\mathcal{T}_5^{(f)} = \mathcal{T}_a^{(f)} + \mathcal{T}_c^{(f)}, \quad (3.51)$$

$$\mathcal{T}_6^{(f)} = \mathcal{T}_b^{(f)} + \mathcal{T}_c^{(f)}. \quad (3.52)$$

The friction models a , b and c can be identified separately by a proper selection of the joint velocities. Let $\dot{q}(k)$ be the set of velocities at which the Stribeck curve is evaluated. The identification experiments are then given by

$$\left. \begin{array}{l} \dot{q}_5 = \dot{q}(k) \\ \dot{q}_6 = -\dot{q}(k) \end{array} \right\} \Rightarrow \mathcal{T}_5^{(f)} = \mathcal{T}_a^{(f)}, \quad \mathcal{T}_6^{(f)} = \mathcal{T}_b^{(f)}, \quad \mathcal{T}_c^{(f)} = \text{const.}, \quad (3.53a)$$

$$\left. \begin{array}{l} \dot{q}_5 = \dot{q}(k) \\ \dot{q}_6 = \dot{q}(k) \end{array} \right\} \Rightarrow \mathcal{T}_5^{(f)} = \mathcal{T}_a^{(f)} + \mathcal{T}_c^{(f)}, \quad \mathcal{T}_6^{(f)} = \mathcal{T}_b^{(f)} + \mathcal{T}_c^{(f)}, \quad (3.53b)$$

from which the Stribeck curves for the friction models a , b and c can be obtained. Note that in equation (3.53a) the friction torque $\mathcal{T}_c^{(f)}$ may be anywhere in between $-\mathcal{T}_7^{(a,BL)}$ and $\mathcal{T}_7^{(a,BL)}$ as \dot{q}_7 equals zero.

3.6 Friction parameter estimation

The values of the parameters are estimated based on the measured values of the Stribeck curve. The measured values are the mean friction torques at constant joint speed. Three measurement series are used in which the measurements at each robot joint are carried out after an initial warmup motion of the robot, see section 3.2.2.

The friction models 1 to 4 and a and c are nonlinear functions of the parameters $\delta^{(a)}$, $\dot{q}^{(s)}$ and $\delta^{(v)}$ and linear functions of the parameters $\mathcal{T}^{(a,BL)}$ and $c^{(v)}$. The friction model b is a nonlinear function of the parameters $\delta^{(a)}$, $\dot{q}^{(s)}$ and $\dot{q}^{(l)}$ and is a linear function of the parameters $\mathcal{T}^{(a,BL)}$ and $\mathcal{T}^{(v,l)}$. Estimating these parameters in a single optimisation requires a nonlinear optimisation technique. However, nonlinear optimisation techniques may lead to local optima in which non-physical parameter values are found, as was already concluded in section 3.2.2. To prevent difficulties with nonlinear estimation techniques, the values are obtained in four steps by means of linear least squares techniques. These steps are described concisely below.

The first step of the identification process is to determine the power $1 - \delta^{(v)}$ and the magnitude $c^{(v)}$ of the viscous part. Taking the natural logarithms of the joint torques and the joint velocities allows for the application of a linear least squares estimation technique to find the viscous friction parameters. Since only the high velocity region, from 0.5 to 4.5 rad/s, is considered, the influence of the asperity friction torques may be neglected. The optimisation problem is defined as

$$\hat{\mathbf{p}}^{(f,v)} = \arg \min_{\mathbf{p}^{(f,v)}} \left\| \ln(\mathcal{T}^{(f,v)}) - \mathbf{A}^{(f,v)} \mathbf{p}^{(f,v)} \right\|_2^2, \quad (3.54)$$

with the parameter vector

$$\mathbf{p}^{(f,v)} = [1 - \delta^{(v)} \quad \ln(c^{(v)})]^T \quad (3.55)$$

and the torque vector

$$\mathcal{T}^{(f,v)} = [\mathcal{T}_1^{(f,v)} \quad \dots \quad \mathcal{T}_n^{(f,v)}]^T. \quad (3.56)$$

The matrix $\mathbf{A}^{(f,v)}$ is then defined as

$$\mathbf{A}^{(f,v)} = \begin{bmatrix} \ln(\dot{q}_1) & 1 \\ \vdots & \vdots \\ \ln(\dot{q}_n) & 1 \end{bmatrix}. \quad (3.57)$$

Both $\mathcal{T}^{(f,v)}$ and $\mathbf{A}^{(f,v)}$ are evaluated at $n = 6$ measured velocity values in the range from 0.5 to 4.5 rad/s.

The linear least squares solution is found by computing

$$\hat{\mathbf{p}}^{(f,v)} = \left(\mathbf{A}^{(f,v)T} \mathbf{A}^{(f,v)} \right)^{-1} \mathbf{A}^{(f,v)T} \mathcal{T}^{(f,v)}, \quad (3.58)$$

and the unknown viscous friction parameters are then obtained by

$$\delta^{(v)} = 1 - \hat{p}_1^{(f,v)}, \quad (3.59a)$$

$$c^{(v)} = \exp\left(\hat{p}_2^{(f,v)}\right). \quad (3.59b)$$

The second step involves the selection of a proper value for the power $\delta^{(a)}$. As a logical first estimate, a value equal to $\delta^{(v)}$ is taken. Additionally, as the value $\dot{q}^{(s)}$ for the Stribeck velocity needs to be chosen. A good first estimate is a value close to the joint velocity where the friction torque is at its minimum.

During the third step, the magnitude of the static asperity friction $\mathcal{T}^{(a,BL)}$ is determined by means of a least squares estimation analogous to the estimation technique described in section 3.2.2. For best model fits, the magnitude of the viscous friction $c^{(v)}$ will again be included in the estimation, which can be done because $c^{(v)}$ is linear in the model. The optimisation problem is now defined as

$$\hat{\mathbf{p}}^{(f)} = \arg \min_{\mathbf{p}^{(f)}} \left\| \mathcal{T}^{(f)} - \mathbf{A}^{(f)} \mathbf{p}^{(f)} \right\|_2^2, \quad (3.60)$$

with the parameter vector

$$\mathbf{p}^{(f)} = [\mathcal{T}^{(a,BL)} \quad c^{(v)}]^T \quad (3.61)$$

and the torque vector is

$$\mathcal{T}^{(f)} = [\mathcal{T}_1^{(f)} \quad \dots \quad \mathcal{T}_n^{(f)}]^T. \quad (3.62)$$

The matrix $\mathbf{A}^{(f)}$ is then

$$\mathbf{A}^{(f)} = \begin{bmatrix} e^{-|\dot{q}_1/\dot{q}^{(s)}|^{\delta^{(a)}}} & \dot{q}_1^{(1-\delta^{(v)})} \\ \vdots & \vdots \\ e^{-|\dot{q}_n/\dot{q}^{(s)}|^{\delta^{(a)}}} & \dot{q}_n^{(1-\delta^{(v)})} \end{bmatrix}. \quad (3.63)$$

Model	$\mathcal{T}^{(a,BL)}$	$\dot{q}^{(s)}$	$\delta^{(a)}$	$c^{(v)}$	$\delta^{(v)}$	$\mathcal{T}^{(v,l)}$	$\dot{q}^{(l)}$
1	0.0255	0.0249	0.5	0.0911	0.3338	-	-
2	0.0448	0.0280	0.5	0.0853	0.5214	-	-
3	0.0093	0.0300	0.5	0.0241	0.4383	-	-
4	0.0332	0.0250	0.5	0.0646	0.4520	-	-
<i>a</i>	0.0115	0.0750	0.5	0.0280	0.2214	-	-
<i>b</i>	0.0194	0.3500	0.5	-	-	0.0098	0.900
<i>c</i>	0.0300	0.2250	0.5	0.0499	0.3156	-	-

Table 3.1: Estimated friction parameters for the friction models of joints 1 through 4 and for the friction models *a*, *b* and *c* of the robot wrist. Note that the values for $\mathcal{T}^{(a,BL)}$, $c^{(v)}$ and $\mathcal{T}^{(v,l)}$ are normalised using the maximum joint torques $\mathcal{T}^{(max)}$.

In this case, both $\mathcal{T}^{(f)}$ and $\mathbf{A}^{(f)}$ are evaluated at $n = 20$ measured velocity values in the full velocity range. The least squares estimate is obtained by computing

$$\hat{\mathbf{p}}^{(f)} = \left(\mathbf{A}^{(f)T} \mathbf{A}^{(f)} \right)^{-1} \mathbf{A}^{(f)T} \mathcal{T}^{(f)}. \quad (3.64)$$

During the fourth and final step, the hand picket values for $\delta^{(a)}$ and $\dot{q}^{(s)}$ are manually fine-tuned using an iterative process. The resemblance between the modelled Stribeck curve and the measured Stribeck curve is inspected visually and by slightly modifying the values for $\delta^{(a)}$ and $\dot{q}^{(s)}$ a set of appropriate vales is obtained. The identified values for the friction parameters are given in table 3.1. The magnitudes $\mathcal{T}^{(a,BL)}$, $c^{(v)}$ and $\mathcal{T}^{(v,l)}$ have been normalised with respect to $\mathcal{T}^{(max)}$.

Figure 3.12 shows the measured mean Stribeck curve for $\overline{\mathcal{T}}^{(f)}$ as well as the estimated Stribeck curve. Note that the measured Stribeck curve is obtained by averaging the joint friction torques $\mathcal{T}^{(f)}$ from $n = 3$ measurements at each joint velocity. In figure 3.12(a) the full velocity range is shown and in figure 3.12(b) a detail of the low (Stribeck) velocity range is shown. In both figures the sampled standard deviation s_n of the measurements is also plotted. The sample standard deviation is computed by

$$s_n = \sqrt{\frac{1}{n} \sum_{i=1}^n \left(\mathcal{T}_i^{(f)} - \overline{\mathcal{T}}^{(f)} \right)^2}. \quad (3.65)$$

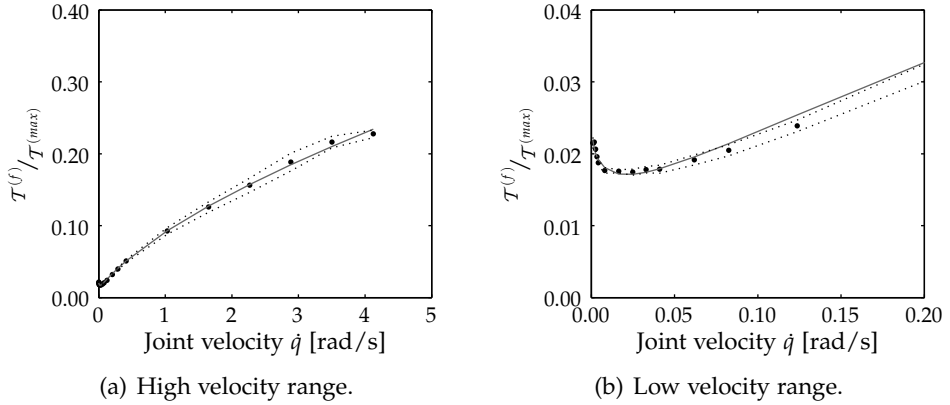


Figure 3.12: Measured (\bullet) and modelled (—) Stribeck curve for joint 1. The sample standard deviation s_n of the measured values is indicated by (\cdots).

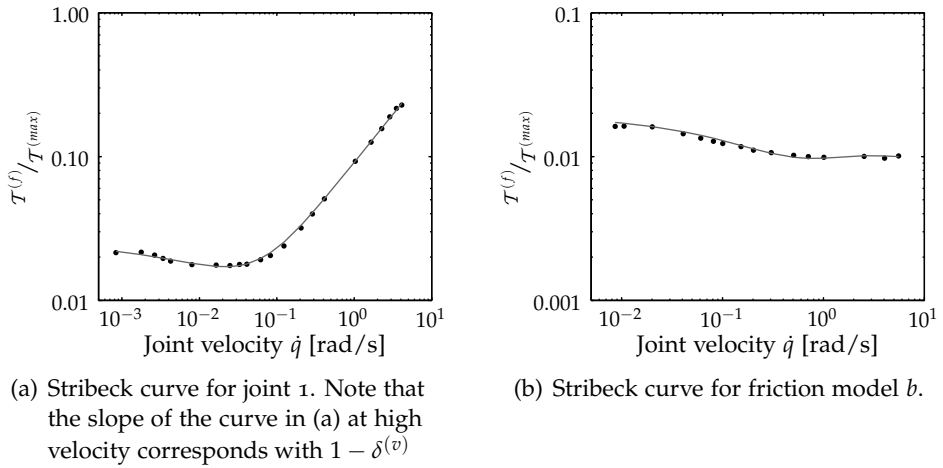


Figure 3.13: Measured and modelled Stribeck curves plotted at logarithmic scales.

In figures 3.13(a) and 3.13(b), both the measured and modelled Stribeck curves for $\mathcal{T}_1^{(f)}$ and for $\mathcal{T}_b^{(f)}$ are plotted on logarithmic scales. It shows that the relative errors between the models and the measurements are equally small across the full velocity range. Consequently, the model accurately describes joint friction for both the low and the high velocity ranges.

3.7 Temperature influence on friction behaviour

The lubricant viscosity strongly depends on the temperature of the lubricant. As the temperature may vary significantly during operation, it needs further attention. An expression for the temperature dependency of the lubricant viscosity has been given by Bhushan (1999):

$$\eta = \eta_0 \exp\left(\frac{\beta}{T} - \frac{\beta}{T_0}\right), \quad (3.66)$$

where η and η_0 are the viscosity at temperature T and reference temperature T_0 , respectively, and β is the temperature–viscosity coefficient. For Newtonian behaviour of the lubricant, the viscosity is the significant temperature dependent variable in modelling the friction torque. For cases wherein the behaviour of the lubricant is non-Newtonian, the limiting shear stress is the temperature dependent variable although its temperature dependency is small.

The parameter $c^{(v)}$ in the joint friction model, equation (3.48), depends on the lubricant viscosity in a linear way. Taking into account the relationship between lubricant viscosity and temperature from equation (3.66), the following proportionality arises

$$c^{(v)} \propto e^{\frac{\beta}{T}}, \quad (3.67)$$

where T is the lubricant temperature. An increase in temperature will lead to a decrease in viscous friction torque. Note that the power $\delta^{(v)}$ in the viscous friction part does not depend on the temperature.

The temperature dependency of the magnitude of the asperity friction torque $\mathcal{T}^{(a,BL)}$ is discussed next. In line with Greenwood and Williamson (1966), the asperity density $d^{(a)}$ from equation (3.31) is considered constant. Consequently, the magnitude of the asperity friction $\mathcal{T}^{(a,BL)}$, which is proportional to the density of the asperities, can also be assumed to

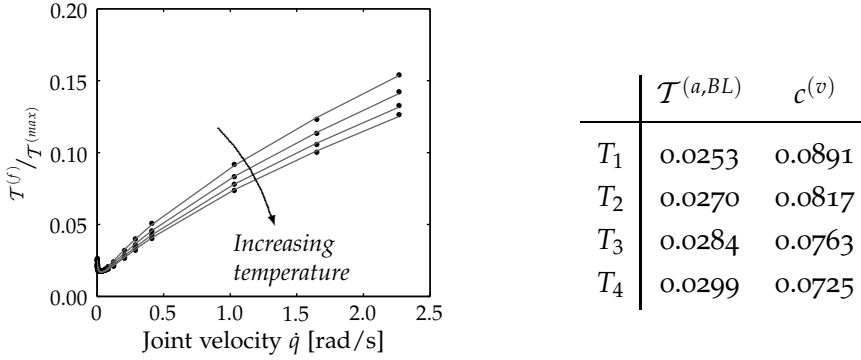


Figure 3.14: Temperature influence on the Stribeck curve and the estimated friction model parameters at increasing temperature ($T_1 < T_2 < T_3 < T_4$) for joints 1. The values for the magnitudes $\mathcal{T}^{(a,BL)}$ and $c^{(v)}$ are normalised with $\mathcal{T}^{(max)}$.

be constant. This assumption implies that the asperity friction force is independent of the lubricant viscosity and the temperature.

Four Stribeck curve measurements for joint 1 are carried out in order to investigate the influence of temperature on the friction torque. The temperature of the drives is influenced by the number of warmup cycles that is performed. During a single warmup cycle the joint is moved from -0.5π to 0.5π and back. Then only the parameters $\mathcal{T}^{(a,BL)}$ and $c^{(v)}$ are identified by means of linear least squares while the other parameters are kept constant. The results are shown in figure 3.14.

Obviously, the friction torque due to the asperities increases slightly at higher temperatures whereas the viscous friction parameter decreases. The temperature dependency of the parameters $\mathcal{T}^{(a,BL)}$ and $c^{(v)}$ has been verified experimentally for all robot joints by Ransijn (2005). It appeared that the model is linear in the parameters that are temperature dependent, which allows the estimation of these parameters in a straightforward way by means of linear least squares. The experiments also indicate that the magnitude of $\mathcal{T}^{(a,BL)}$ can indeed be considered invariant for changes of lubricant temperature as it only changes slightly as a function of the rising temperature.

3.8 Pre-sliding friction

The models discussed in the previous section accurately describe joint friction in the sliding regime. However, for velocities equal to zero, the friction model is not defined and transitions from negative velocity to positive velocity and vice versa cannot be described. So, in order to use the friction model in dynamic robot simulations, which do include reversals in the joint velocity, the model has to be extended in such a way that it can cope with the so-called pre-sliding regime.

Pre-sliding friction characteristics can be added both kinematically and dynamically. The kinematic solution is to define a function that describes the transition of the friction torque through zero as a function of the joint velocity \dot{q} . Dynamic pre-sliding models have an internal state variable. This state variable resembles the elastic behaviour of the connection asperities at zero velocity, which yields a friction torque that is position dependent (Dahl, 1968, 1977).

3.8.1 Kinematic pre-sliding modelling

A very commonly applied kinematic friction model is the switching friction model:

$$\mathcal{T}^{(f,S)} = \begin{cases} \mathcal{T}^{(f)}(\dot{q}) & \text{if } \dot{q} > 0, \\ 0 & \text{if } \dot{q} = 0, \\ -\mathcal{T}^{(f)}(-\dot{q}) & \text{if } \dot{q} < 0, \end{cases} \quad (3.68)$$

where $\mathcal{T}^{(f)}(\dot{q})$ denotes the friction models that have been derived in section 3.5. The friction model is suitable for inverse dynamic modelling, where the joint velocity is accurately known as a function of time. However, in forward dynamic simulations of the controlled robot system, the discontinuous nature of the friction model may cause integration difficulties. Furthermore, small velocity variations around zero will cause rapid changes between the positive $\mathcal{T}^{(a,BL)}$ and negative $-\mathcal{T}^{(a,BL)}$ asperity friction torques, which is clearly non-physical behaviour.

An improved solution would be the use of a smooth, but rapid, transition between the maximum and minimum asperity friction torque by means of a continuous function. A convenient function is the inverse tangent function, which yields

$$\mathcal{T}^{(f,K)} = \frac{2}{\pi} \arctan(c \dot{q}) \mathcal{T}^{(f)}(|\dot{q}|), \quad (3.69)$$

where the superscript K denotes the kinematic friction model. The variable c is used to scale the velocity range in which the function is effective. The effective velocity range is usually between -10^{-4} rad/s and 10^{-4} rad/s, which requires c to be in the order of 10^6 .

3.8.2 Dynamic pre-sliding modelling

A well known dynamic pre-sliding friction model that incorporates an internal state is the LuGre model (Canudas De Wit et al., 1995). In the LuGre model, the pre-sliding regime is interpreted as bending bristles, wherein a state z is a measure for the deflection of the bristles. At zero joint velocity, the bending of the bristles is related to the relative joint (micro) rotation q . The LuGre model is defined by a differential equation for the state z and an output equation for the dynamic friction torque $\mathcal{T}^{(f,D)}$

$$\frac{dz}{dt} = \dot{q} - \frac{c^{(0)}|\dot{q}|}{g(\dot{q})}z, \quad (3.70a)$$

$$\mathcal{T}^{(f,D)} = c^{(0)}z + c^{(1)}\frac{dz}{dt} + f(\dot{q}), \quad (3.70b)$$

where the function $g(\dot{q})$ describes the Stribeck effect, the function $f(\dot{q})$ describes the viscous friction, $c^{(0)}$ denotes the stiffness of the bristles and $c^{(1)}$ is the damping coefficient.

In a steady state situation, $\frac{dz}{dt} = 0$, at nonzero velocities $\dot{q} > 0$, the expression for the friction torque is reduced to

$$\mathcal{T}^{(f,D)} = g(\dot{q}) + f(\dot{q}). \quad (3.71)$$

Remembering the friction models from section 3.5, it is straightforward to apply the following substitutions for the functions $g(\dot{q})$ and $f(\dot{q})$:

$$g(\dot{q}) = \mathcal{T}^{(a)}(\dot{q}) \quad \text{for the asperity friction,} \quad (3.72a)$$

$$f(\dot{q}) = \mathcal{T}^{(v)}(\dot{q}) \quad \text{for the viscous friction in gears, and} \quad (3.72b)$$

$$f(\dot{q}) = \mathcal{T}^{(l)}(\dot{q}) \quad \text{for the viscous friction in bearings.} \quad (3.72c)$$

The steady-state pre-sliding behaviour of the LuGre model is analysed by solving the differential equation (3.70a). For near zero positive

velocities \dot{q} , the following approximations may be introduced:

$$\begin{aligned} f(\dot{q} \approx 0) &= 0, & g(\dot{q} \approx 0) &= \mathcal{T}^{(a,BL)}, \\ |\dot{q}| &= \dot{q}, & \mathcal{T}^{(f,D)} &= c^{(0)}z. \end{aligned} \quad (3.73)$$

Substitution of equations (3.73) in (3.70a), rewriting \dot{q} as $\frac{dq}{dt}$ and some rearranging yields

$$\frac{dz}{dt} = \frac{dq}{dt} \left(1 - \frac{c^{(0)}}{\mathcal{T}^{(a,BL)}}z \right), \quad (3.74)$$

which is simplified into the differential equation

$$dq = \left(\frac{\mathcal{T}^{(a,BL)}}{\mathcal{T}^{(a,BL)} - c^{(0)}z} \right) dz. \quad (3.75)$$

Solving the differential equation (3.75) yields

$$q_1 - q_0 = \frac{-\mathcal{T}^{(a,BL)}}{c^{(0)}} \ln \left(\mathcal{T}^{(a,BL)} - c^{(0)}z \right) \Bigg|_{z_0}^{z_1}, \quad (3.76)$$

leading to

$$\Delta q = \frac{\mathcal{T}^{(a,BL)}}{c^{(0)}} \ln \left(\frac{\mathcal{T}^{(a,BL)} - c^{(0)}z_0}{\mathcal{T}^{(a,BL)} - c^{(0)}z_1} \right). \quad (3.77)$$

Introducing the boundary conditions $q_0 = 0$ and $q_1 = q$, combined with the substitutions $c^{(0)}z_0 = \mathcal{T}_0^{(f,D)}$ and $c^{(0)}z_1 = \mathcal{T}^{(f,D)}$, yields—after some rearranging—the steady-state pre-sliding friction torque $\mathcal{T}^{(f,D)}$ as a function of the relative displacement q

$$\mathcal{T}^{(f,D)} = \mathcal{T}^{(a,BL)} + \left(\mathcal{T}_0^{(f,D)} - \mathcal{T}^{(a,BL)} \right) e^{-q \frac{c^{(0)}}{\mathcal{T}^{(a,BL)}}}. \quad (3.78)$$

It shows that the steady-state pre-sliding behaviour is expressed as an exponential function, as is illustrated in figure 3.15(a). The figure shows that the pre-sliding friction torque exponentially increases towards the breakaway torque, which is the asperity friction torque $\mathcal{T}^{(a,BL)}$.

The behaviour of the LuGre friction model at small displacements is studied by applying a small sinusoidal torque to the friction model of joint 1. The resulting behaviour shows a hysteresis loop, which is illustrated in figure 3.15(b). The hysteresis behaviour is of particular interest for applications where a high positioning accuracy is required.

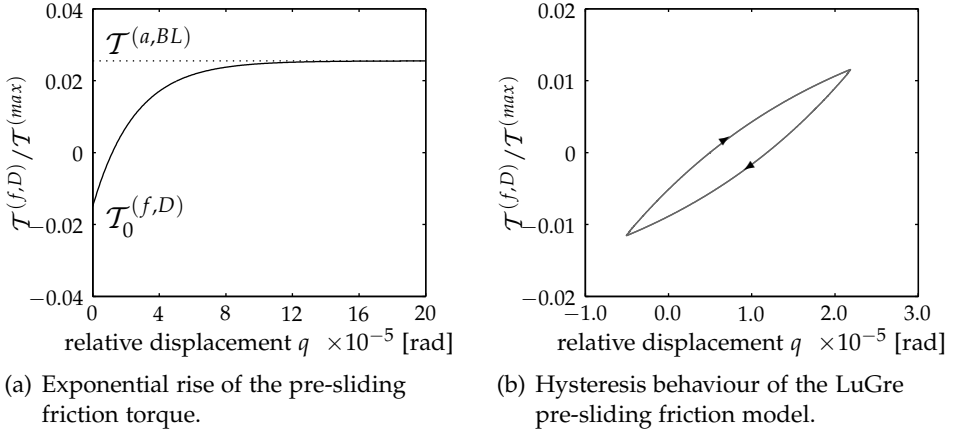


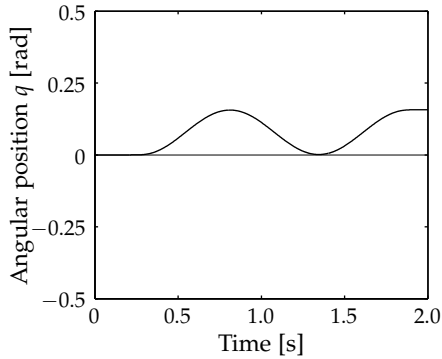
Figure 3.15: Pre-sliding characteristics of the LuGre model for joint 1. The friction torque $\mathcal{T}^{(f,D)}$ as a function of the relative angular displacement q .

3.8.3 Kinematic vs. dynamic pre-sliding friction

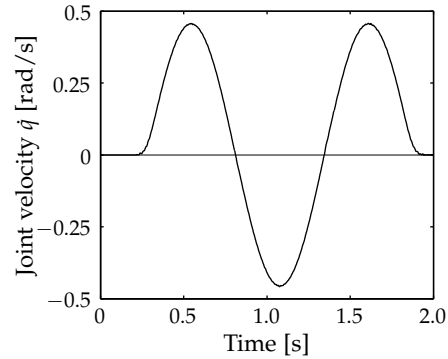
In order to compare the performance of the kinematic and the dynamic (LuGre) pre-sliding model, closed-loop simulations of joint 1 with the robot in an upright position are performed. The joint is moved with a sinusoidal velocity profile, which is illustrated in figures 3.16(a) and 3.16(b).

For this experiment, the first joint of the robot is modelled by a single rotational inertia J . Generally, the unknown value for the pre-sliding stiffness $c^{(0)}$ is obtained from an experiment where the joint torque is slowly increased towards the asperity friction torque $\mathcal{T}^{(a,BL)}$, while measuring the angular displacement of the robot joint. This exercise requires encoders with sufficiently high angular resolution. Unfortunately, the standard robot set-up does not provide a high resolution such as this, so an accurate estimation of the pre-sliding regime is not possible (Kool, 2003).

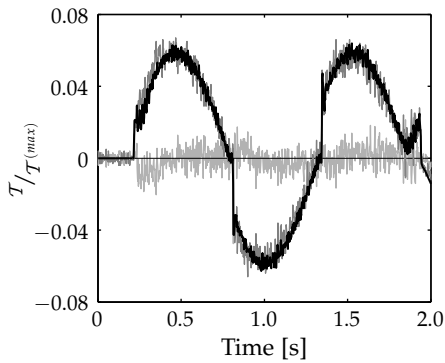
In an alternative approach, the value for the pre-sliding stiffness is chosen so that the rise in the simulated joint torque corresponds well with the measured joint torque. The resulting value for $c^{(0)}$ is in the order of $10^4 - 10^5$, depending on the specific joint. The value for the micro-viscous damping coefficient $c^{(1)}$ is chosen so that a relative viscous damping of



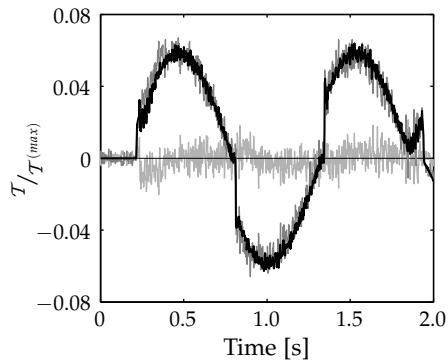
(a) Angular position.



(b) Joint velocity.



(c) Kinematic model.



(d) LuGre model.

Figure 3.16: Pre-sliding friction performance of a kinematic and a dynamic (LuGre) friction model during 1 DOF closed-loop simulation of joint 1, with: — the measured torque, — the simulated torque and — the residual torque.

$\zeta = 0.1$ is obtained,

$$\zeta = \frac{c^{(1)}}{2J\omega_n}, \quad (3.79a)$$

with

$$\omega_n = \sqrt{\frac{c^{(0)}}{J}}, \quad (3.79b)$$

which yields a value which is generally in the order of $\sqrt{c^{(0)}}$ and in this case this yields a value of approximately 10 for $c^{(1)}$.

The simulation results are shown in figures 3.16(c) and 3.16(d). The first conclusion that can be drawn from these results is that the closed-loop simulations accurately predict the joint torques. Secondly, there is, at the presented scale, no noticeable difference between the kinematic and the dynamic friction models.

As pointed out before, the angular resolution of the position sensors is not sufficient for a detailed study of the pre-sliding characteristics such as the hysteresis effect. Apparently, the reverse is also true and that leads to the conclusion that for closed-loop simulations with a rigid robot model it is not necessary to study the pre-sliding behaviour in more detail and that the presented pre-sliding models are sufficiently accurate for the scope of this thesis. A definitive choice for either the kinematic or the dynamic pre-sliding friction model will be made in chapter 5.

Fitting the robot with more accurate angular sensors to study the pre-sliding behaviour in detail might not give a straightforward solution because disturbances such as backlash in the gears and joint flexibility start to become visible at smaller scales. Consequently, a detailed study of the pre-sliding behaviour requires that effects such as backlash and joint flexibility should also be included in the robot model.

3.9 Discussion

In this chapter, the modelling and identification of joint friction has been discussed. It was shown that phenomenological friction models, commonly used in control literature, are inadequate for modelling the viscous friction behaviour of the robot transmission for the full velocity range with sufficient accuracy. Therefore, a new joint friction model has been

developed that relies on insights from sophisticated tribological models. The friction behaviour of two lubricated discs in a rolling–sliding contact is used to analyse the different contacts inside the gears and bearings of the robot transmission.

It is shown that the film height of the lubricant is a function of the sum velocity, which causes a nonlinear relationship between the joint angular velocity and the viscous friction torques. The analysis shows different behaviour for gears and prestressed bearings. Furthermore, it has been shown that the level of the friction force caused by the asperity contacts depends on the ratio between lubricant film height and the height distribution of the surface summits. Increasing the velocity leads to a decrease in the asperity friction torque.

Sub-models for the viscous friction and the friction due to the asperities are combined into two new friction models; one for gears and one for prestressed roller bearings. The sub-models describing the asperity part of the roller bearing and the viscous part of the helical gear pair are combined into a joint friction model. Using this method, a new friction model is developed that accurately describes the friction behaviour with a minimal and physically sound parametrisation.

Next, the joint friction model parameters have been identified by means of experiments. The experiments indicate that the model accurately describes the friction torque within the full velocity range. The model is linear in parameters that are temperature dependent which allows the estimation of the parameters during the inertia parameter identification. The model, in which the Coulomb friction effect has disappeared, has exactly the same number of model parameters as the commonly used Stribeck model of equation (3.5). Finally, the model has been extended in such a way that it is able to predict the joint friction behaviour in the pre-sliding regime during reversals of the joint velocity.

Chapter 4

Robot arm

4.1 Introduction

The modelling and identification of robotic manipulators has been widely discussed in robotics literature, for instance the textbooks of Corke (1996), Kozłowski (1998) and Khalil and Dombre (2002). For the modelling of the robotic manipulator dynamics, there are mainly two formulations that have been used in literature; the recursive Newton-Euler formulation and the Lagrange formulation. The recursive Newton-Euler formulation (Luh et al., 1980) is considered to be one of the most efficient algorithms for real-time computation of the inverse dynamic model. Consequently, it has been applied by many authors, e.g. Khosla (1989); Calafiore et al. (2001); Khalil and Dombre (2002).

In this thesis a nonlinear finite element method (Jonker, 1990) is used to formulate the dynamic equations of the robotic manipulator. In this method, the equations of motion are derived by using Lagrange's form of Jourdain's principle. This principle, a virtual power type approach, has the advantage of automatic elimination of non-working joint constraint forces and torques, but without the tedious calculation of partial differentiation.

The SPACAR computer program, based on this finite element formulation, has been developed (Jonker and Meijaard, 1990) for dynamic analysis and simulation of mechanisms that can be assembled from basic components, including beams, hinges, sliders, springs and dampers. The program also allows analytic generation of locally linearised models around a nominal trajectory (Jonker, 1988; Meijaard, 1991). Interfaces for con-

trol system design with MATLAB and SIMULINK have been developed by Jonker and Aarts (1998). This allows the analysis of advanced control schemes for application in mechanical systems. Recently, the finite element formulation has been extended with a module for automatic generation of dynamic models suitable for dynamic parameter identification (Hardeman et al., 2006b).

The problem that has to be addressed in order to obtain an accurate dynamic robot model is to find the values of the model parameters. Determination of the parameter values from Computer Aided Design (CAD) models may not yield a reliable and accurate representation because the models are often insufficiently detailed; they may not include the actual models of the servo motors, the servo wiring and/or the bearings. Furthermore, obtaining the rotational inertias of the transmissions requires a dynamic analysis which is generally not a feature that is included in the CAD system. However, the functionality of modern CAD software is constantly improving. Sophisticated parametric 3D solid modelling and an increase in model details may give sufficiently accurate model parameters in the near future. The most efficient way to obtain accurate values of the unknown model parameters may be experimental parameter identification using the assembled robot. The problem of obtaining the dynamic model parameters by means of experimental identification has been addressed by many authors. A general overview of experimental robot identification using linear least squares techniques can be found in the textbooks of Kozłowski (1998) and Khalil and Dombre (2002).

Outline

In this chapter, the modelling and identification of the inertia properties of the robotic arm will be presented. First, in section 4.2, a finite element representation of the robot arm will be given which will be used to derive the dynamic robot model. In this thesis, the robot links and joints are considered to be sufficiently stiff in order to allow both the joints and links to be modelled as rigid elements. The dynamic model of the robot is written in both an acceleration linear and a parameter linear form. The first form allows the model to be incorporated in closed-loop forward dynamic simulations, as will be presented in chapter 5. The latter form is derived in order to apply linear regression techniques for the identification of the unknown model parameters. In section 4.3, the identification of the unknown parameters will be discussed. It starts with the formulation of

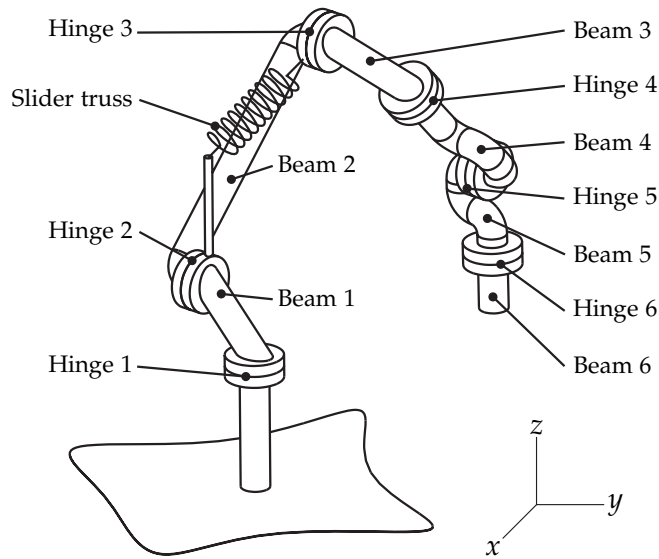


Figure 4.1: Finite element model of the Stäubli RX90B robot arm.

a linear least squares problem. Subsequently, the least squares problem will be analysed by means of singular value decomposition. The influence of errors will be discussed as well as the need for scaling. Finally, section 4.4 deals with the actual identification experiments. In a series of experiments, the unknown inertia parameters of the robot will be identified. The results are then validated with respect to the manufacturer's data and by means of validation experiments.

4.2 Finite element model of the robot arm

In the finite element formulation the manipulator mechanism is modelled as an assembly of interconnected finite elements. The gravity compensation spring inside link 2 (figure 2.1) is modelled as a slider-truss element. The manipulator links are modelled by beam elements. The joints are represented by six cylindrical hinge elements, which are actuated by torque servos. The manipulator mechanism is assembled by allowing the elements to have nodal points in common. The finite element model of the manipulator arm is depicted in figure 4.1.

The location of each element k is described relative to a fixed coordi-

nate system (xyz) by a set of nodal coordinates $\mathbf{x}^{(k)}$. Some coordinates may be Cartesian coordinates of the end nodes, while others may be sets of Euler parameters describing the orientation of orthogonal base vectors or triads, rigidly attached to the element nodes.

The key point in the finite element formulation is the specification of independent deformation modes for the description of the current state of an element. If the specification of the deformation modes is invariant for arbitrary large translations and rotations, then rigid body motions can be analysed by setting all deformations equal to zero.

The element's deformation modes are specified by a set of deformation mode coordinates $e^{(k)}$. These deformation mode coordinates may either be associated with large relative displacements or rotations between the element nodes, denoted by $e_i^{(k)}$, or be associated with small elastic deformations, in that case denoted by $\varepsilon_i^{(k)}$. The deformation mode coordinates are expressed as analytical functions of the elements nodal coordinates. These functions are known as deformation functions and have a clear physical meaning. They are expressed as vector functions as

$$\mathbf{e}^{(k)} = \mathcal{D}^{(k)}(\mathbf{x}^{(k)}), \quad (4.1)$$

or in component form as

$$e_i^{(k)} = \mathcal{D}_i^{(k)}(\mathbf{x}^{(k)}), \quad (4.2)$$

where the subscript i represents the deformation mode number. The number of deformation modes is equal to the number of nodal coordinates minus the number of degrees of freedom of the element as a rigid body. In Appendix B, the description of the deformation functions for the three finite elements that are used in the robot model—the slider truss, the spatial hinge and the spatial beam—is given.

4.2.1 Kinematic analysis

A kinematic robot model can be assembled with the finite elements by letting them have nodal points in common. In this way, a vector $\mathbf{x} = (x_1, x_2, \dots, x_{n^x})$ of nodal coordinates for the complete robot model is defined. The subscript n^x denotes the total number of nodal coordinates. The vector of deformation modes \mathbf{e} of the elements are then written as a

vector function of the nodal coordinates:

$$\begin{bmatrix} e_1 \\ \vdots \\ e_{n^e} \end{bmatrix} = \begin{bmatrix} \mathcal{D}_1(\mathbf{x}) \\ \vdots \\ \mathcal{D}_{n^e}(\mathbf{x}) \end{bmatrix}, \quad \text{or} \quad \mathbf{e} = \mathcal{D}(\mathbf{x}), \quad (4.3)$$

where the number of deformation mode coordinates is defined as n^e .

Kinematic constraints are introduced by imposing conditions on both nodal coordinates x_i and deformation mode coordinates e_i . The kinematic constraints on the nodal coordinates correspond to the fixed nodes of the robot base and are denoted by $\mathbf{x}^{(0)}$. For a rigid robot, the kinematic constraints on the deformation mode coordinates correspond with the deformation modes of the beam elements and the bending modes of the hinge element which have a prescribed value of zero and are denoted by $\mathbf{e}^{(0)}$. The first deformation mode coordinates of the six hinge elements, denoted by $\mathbf{e}^{(m)} = (e_1^{(m)}, e_2^{(m)}, \dots, e_6^{(m)})$, are taken as the degrees of freedom. This leaves the deformation mode of the slider truss element that models the gravity compensating spring, denoted by $e^{(c)}$, as the only calculable deformation coordinate. The remaining nodal coordinates that have to be computed are denoted by $\mathbf{x}^{(c)}$.

The main objective of the kinematic analysis is to solve the system of equation (4.3) for the generalised degrees of freedom $\mathbf{e}^{(m)}$. The solution is expressed as

$$\mathbf{x} = \mathcal{F}^{(x)}(\mathbf{e}^{(m)}), \quad (4.4a)$$

and

$$e^{(c)} = \mathcal{F}^{(e,c)}(e^{(m)}), \quad (4.4b)$$

where $\mathcal{F}^{(x)}$ and $\mathcal{F}^{(e,c)}$ are known as the geometric transfer functions.

Generally, the geometric transfer functions cannot be calculated explicitly from equation (4.3) but they have to be determined numerically in an iterative way (Jonker and Meijaard, 1990). For rigid robotic manipulators that form an open kinematic chain of joints and links, it is possible to determine the geometric transfer functions analytically, see e.g. Khalil and Dombre (2002).

The nodal velocities and the deformation rates are obtained by differentiating equations (4.4) with respect to time:

$$\dot{\mathbf{x}} = \mathbf{D}\mathcal{F}^{(x)}\dot{\mathbf{e}}^{(m)}, \quad (4.5a)$$

$$\dot{\mathbf{e}}^{(c)} = \mathbf{D}\mathcal{F}^{(e,c)}\dot{\mathbf{e}}^{(m)}, \quad (4.5b)$$

where the differentiation operator \mathbf{D} represents the partial differentiation with respect to the vector $\mathbf{e}^{(m)}$. The matrices $\mathbf{D}\mathcal{F}^{(x)}$ and $\mathbf{D}\mathcal{F}^{(e,c)}$ are known as the first order geometric transfer functions. Differentiating the vector of nodal velocities again with respect to time yields the vector of nodal accelerations

$$\ddot{\mathbf{x}} = (\mathbf{D}^2\mathcal{F}^{(x)}\dot{\mathbf{e}}^{(m)})\dot{\mathbf{e}}^{(m)} + \mathbf{D}\mathcal{F}^{(x)}\ddot{\mathbf{e}}^{(m)}, \quad (4.6)$$

where the tensor $\mathbf{D}^2\mathcal{F}^{(x)}$ is known as the second order geometric transfer function.

4.2.2 Dynamic analysis

In a dynamic analysis, the forces and torques are related to the robot's position, velocity and acceleration. Since the robot links are assumed to be rigid, the inertia properties are described by means of lumped masses at the nodes of the element. In this idealisation rigid bodies with equivalent mass and rotational inertias are attached to the end-nodes of the element. In this section, the equations of motion are derived in a form linear in the acceleration and in a form linear in the inertial parameters. The latter requires a parameter linear mass formulation for the finite elements constituting the manipulator mechanism.

Equations of motion in acceleration linear form

The equations of motion are formulated in terms of the degrees of freedom by means of the principle of virtual power (Jourdain's principle) and the first and second order geometric transfer functions. Let \mathbf{M} be the global mass matrix, obtained by assembling the mass matrices of the individual beam elements, and let $\mathbf{f}^{(x)}$ be the global force vector including the gravitational forces and the velocity dependent inertia forces (Jonker, 1988). Application of the principle of virtual power for the external forces,

including the inertial forces, and the vector of generalised stress resultants $\sigma^{(m)}$ associated with the hinge elements and the internal force of the compensating spring $\sigma^{(c)}$ yields

$$\langle (\mathbf{f}^{(x)} - \mathbf{M}\ddot{\mathbf{x}}), \delta\dot{\mathbf{x}} \rangle = \langle \sigma^{(m)}, \delta\dot{\mathbf{e}}^{(m)} \rangle + \langle \sigma^{(c)}, \delta\dot{\mathbf{e}}^{(c)} \rangle, \quad (4.7)$$

for all virtual velocities $\delta\dot{\mathbf{x}}$ and $\delta\dot{\mathbf{e}}$ satisfying the instantaneous kinematic constraints of equation (4.5). The operator $\langle \mathbf{a}, \mathbf{b} \rangle$ denotes the scalar product of vectors \mathbf{a} and \mathbf{b} . Substitution of equations (4.5) into equation (4.7) with the transpose transformations $\mathbf{D}\mathcal{F}^{(x)T}$ and $\mathbf{D}\mathcal{F}^{(e,c)T}$ yields

$$\mathbf{D}\mathcal{F}^{(x)T}(\mathbf{f}^{(x)} - \mathbf{M}\ddot{\mathbf{x}}) - \sigma^{(m)} - \mathbf{D}\mathcal{F}^{(e,c)T}\sigma^{(c)} = \mathbf{0}. \quad (4.8)$$

Substitution of equation (4.6) into equation (4.8) yields the equations of motion in terms of the joint degrees of freedom $\mathbf{q} = \mathbf{e}^{(m)}$:

$$\overline{\mathbf{M}}\ddot{\mathbf{q}} + \mathbf{D}\mathcal{F}^{(x)T}[\mathbf{M}((\mathbf{D}^2\mathcal{F}^{(x)}\dot{\mathbf{q}})\dot{\mathbf{q}}) - \mathbf{f}^{(x)}] + \mathbf{D}\mathcal{F}^{(e,c)T}\sigma^{(c)} = \mathcal{T}, \quad (4.9)$$

where $\overline{\mathbf{M}}$ is the reduced mass matrix, defined as

$$\overline{\mathbf{M}} = \mathbf{D}\mathcal{F}^{(x)T}\mathbf{M}\mathbf{D}\mathcal{F}^{(x)}, \quad (4.10)$$

and the vector of generalised stress resultants $\sigma^{(m)}$ has been replaced by the vector of joint torques

$$\sigma^{(m)} = -\mathcal{T}. \quad (4.11)$$

The reversed sign is a result of different sign conventions for the driving torques in control engineering literature and in structural dynamics literature.

Substitution of the joint torque of equation (2.5), page 21, into the reduced equations of motion (4.9) yields after some rearranging

$$\begin{aligned} \overline{\mathbf{M}}^{(N)}\ddot{\mathbf{q}} + \mathbf{D}\mathcal{F}^{(x)T}[\mathbf{M}((\mathbf{D}^2\mathcal{F}^{(x)}\dot{\mathbf{q}})\dot{\mathbf{q}}) - \mathbf{f}^{(x)}] \\ + \mathbf{D}\mathcal{F}^{(e,c)T}\sigma^{(c)} - \mathcal{T}^{(f)} = \mathcal{T}^{(m)}, \end{aligned} \quad (4.12)$$

where the combined mass matrix $\overline{\mathbf{M}}^{(N)}$ is defined as

$$\overline{\mathbf{M}}^{(N)} = \overline{\mathbf{M}} + \mathbf{T}^T\mathbf{J}^{(m)}\mathbf{T} \quad (4.13)$$

in which the matrix $\mathbf{T}^T\mathbf{J}^{(m)}\mathbf{T}$ represents the servo's rotor inertias. Furthermore, the vector of motor torques $\mathcal{T}^{(m)}$ is computed from the vector of servo motor currents according to equation (2.6), page 21.

The constitutive equation for the gravity compensating spring is given by

$$\sigma^{(c)} = \sigma^{(c,0)} + k^{(c)}e^{(c)}, \quad (4.14)$$

where $\sigma^{(c)}$ is the internal stress of the spring, $k^{(c)}$ is the stiffness of the spring and $\sigma^{(c,0)}$ denotes the pre-stress.

Equations of motion in parameter linear form

In the case of a lumped mass formulation, the equations of motion can also be written in a parameter linear form. For a single beam element k the equations of motion in a parameter linear form may be expressed as

$$\Phi^{(k,l)} \mathbf{p}^{(k,l)} = \mathbf{f}^{(k,p)}, \quad (4.15)$$

with the parameter vector

$$\mathbf{p}^{(k,l)} = \begin{bmatrix} m^{(k)} \\ m^{(k)} \mathbf{s}'^{(k)} \\ \mathbf{l}^{(k)} \end{bmatrix}. \quad (4.16)$$

The matrix $\Phi^{(k,l)}$ is a kinematic function of the element's nodal coordinates, velocities and accelerations. The vector $\mathbf{f}^{(k,p)}$ represents the external nodal forces and torques acting on node p . The vector $\mathbf{l}^{(k)}$ consists of the upper triangle elements of the inertia matrix $\mathbf{J}'^{(k,p)}$, which are

$$\mathbf{l}^{(k,l)} = (J'_{xx}{}^{(k,p)}, J'_{yy}{}^{(k,p)}, J'_{zz}{}^{(k,p)}, J'_{xy}{}^{(k,p)}, J'_{xz}{}^{(k,p)}, J'_{yz}{}^{(k,p)}), \quad (4.17)$$

where $\mathbf{J}'^{(k,p)}$ and $\mathbf{s}'^{(k)}$ denote the inertia matrix and the position vector of the centre of gravity with constant components in reference to the body fixed coordinate system (x', y', z') , see figure 4.2. For a detailed derivation of the lumped mass formulation in the parameter linear form the reader is referred to Hardeman et al. (2006b).

Let $\Phi^{(l)}(\ddot{\mathbf{q}}, \dot{\mathbf{q}}, \mathbf{q})$ be the global system matrix obtained by assembling the lumped matrices $\Phi^{(k,l)}$ and let $\mathbf{p}^{(l)}$ be the associated parameter vector, containing the lumped inertia parameters of the manipulator. Keeping in mind that the term $\Phi^{(l)} \mathbf{p}^{(l)}$ includes all inertia and gravitational forces, the principle of virtual power can be applied as follows:

$$\langle -\Phi^{(l)} \mathbf{p}^{(l)}, \delta \dot{\mathbf{x}} \rangle = \langle \sigma^{(m)}, \delta \dot{e}^{(m)} \rangle + \langle \sigma^{(c)}, \delta \dot{e}^{(c)} \rangle, \quad (4.18)$$

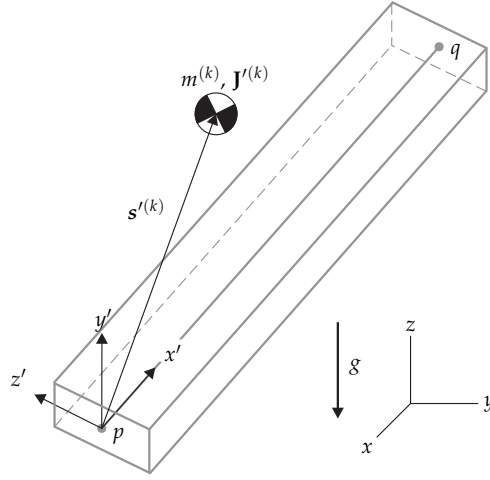


Figure 4.2: The lumped mass formulation of the spatial beam element.

which must hold true for all virtual velocities $\delta\dot{x}$, $\delta\dot{e}^{(m)}$ and $\delta\dot{e}^{(c)}$ satisfying the instantaneous kinematic constraints of equation (4.5).

Substitution of equations (4.5) and $\sigma^{(m)} = -\mathcal{T}$ into equation (4.18), yields, with the transpose transformations $\mathbf{D}\mathcal{F}^{(x)T}$ and $\mathbf{D}\mathcal{F}^{(e,c)T}$,

$$\mathbf{D}\mathcal{F}^{(x)T}\Phi^{(l)}\mathbf{p}^{(l)} + \mathbf{D}\mathcal{F}^{(e,c)T}\sigma^{(c)} = \mathcal{T}. \quad (4.19)$$

The vector of inertia parameters $\mathbf{p}^{(l)}$ is defined by

$$\mathbf{p}^{(l)} = [\mathbf{p}^{(1,l)} \quad \mathbf{p}^{(2,l)} \quad \dots \quad \mathbf{p}^{(6,l)}]^T, \quad (4.20)$$

with for each link $k = 1, 2, \dots, 6$ the ten inertia parameters

$$\mathbf{p}^{(k,l)} = \begin{bmatrix} m^{(k)} & ms_x'^{(k)} & ms_y'^{(k)} & ms_z'^{(k)} \\ J_{xx}'^{(k)} & J_{yy}'^{(k)} & J_{zz}'^{(k)} & J_{xy}'^{(k)} & J_{xz}'^{(k)} & J_{yz}'^{(k)} \end{bmatrix}. \quad (4.21)$$

The constitutive equation for the gravity compensating spring, described by equation (4.14), will be reformulated as

$$\sigma^{(c)} = \Phi^{(s)}\mathbf{p}^{(s)}, \quad (4.22)$$

with

$$\Phi^{(s)} = [1 \quad e^{(c)}] , \quad (4.23a)$$

$$p^{(s)} = \begin{bmatrix} \sigma^{(c,0)} \\ k^{(c)} \end{bmatrix} . \quad (4.23b)$$

The vector of joint driving torques \mathcal{T} , as defined in equation (2.5), page 21, can also be written in a parameter linear form

$$\mathcal{T} = \mathcal{T}^{(m)} - \Phi^{(m)} p^{(m)} - \Phi^{(f)} p^{(f)} , \quad (4.24)$$

where

$$\Phi^{(m)} = \mathbf{T}^T \text{diag}(\mathbf{T}\dot{q}) \quad (4.25a)$$

and

$$p^{(m)} = \text{diag}(\mathbf{J}^{(m)}) = [J_1^{(m)} \quad J_2^{(m)} \quad \dots \quad J_6^{(m)}]^T \quad (4.25b)$$

is the vector of motor inertias.

The joint friction models, developed in chapter 3, contain five friction parameters for each joint j . Furthermore, for each joint j , the friction model includes two temperature dependent friction parameters $\mathcal{T}_j^{(a,BL)}$ and $c_j^{(v)}$ which are linear in the friction model. The joint friction model is a nonlinear function of the remaining three parameters $\delta_j^{(a)}$, $\dot{q}_j^{(s)}$ and $\delta_j^{(v)}$. The latter are not temperature dependent and are therefore considered to be constant. Expressing the friction model in the parameter linear form yields the matrix

$$\Phi^{(f)} = \begin{bmatrix} \Phi_1^{(f)} & 0 & 0 & 0 & 0 & 0 & 0 \\ 0 & \Phi_2^{(f)} & 0 & 0 & 0 & 0 & 0 \\ 0 & 0 & \Phi_3^{(f)} & 0 & 0 & 0 & 0 \\ 0 & 0 & 0 & \Phi_4^{(f)} & 0 & 0 & 0 \\ 0 & 0 & 0 & 0 & \Phi_a^{(f)} & 0 & \Phi_c^{(f)} \\ 0 & 0 & 0 & 0 & 0 & \Phi_b^{(f)} & \Phi_c^{(f)} \end{bmatrix} \quad (4.26)$$

where

$$\Phi_j^{(f)} = \text{sign}(\dot{q}_j) \begin{bmatrix} e^{-|\dot{q}_j/\dot{q}_j^{(s)}|^{\delta_j^{(a)}}} & |\dot{q}_j|^{(1-\delta_j^{(v)})} \end{bmatrix}, \quad \text{for } j = 1 \text{ to } 4, \quad (4.27a)$$

$$\Phi_a^{(f)} = \text{sign}(\dot{q}_5) \begin{bmatrix} e^{-|\dot{q}_5/\dot{q}_5^{(s)}|^{\delta_5^{(a)}}} & |\dot{q}_5|^{(1-\delta_5^{(v)})} \end{bmatrix}, \quad (4.27b)$$

$$\Phi_b^{(f)} = \text{sign}(\dot{q}_6) \begin{bmatrix} e^{-|\dot{q}_6/\dot{q}_6^{(s)}|^{\delta_6^{(a)}}} & 1 - e^{-|\dot{q}_6/\dot{q}_6^{(l)}|} \end{bmatrix}, \quad (4.27c)$$

$$\Phi_c^{(f)} = \text{sign}(\dot{q}_7) \begin{bmatrix} e^{-|\dot{q}_7/\dot{q}_7^{(s)}|^{\delta_7^{(a)}}} & |\dot{q}_7|^{(1-\delta_7^{(v)})} \end{bmatrix}. \quad (4.27d)$$

Note that $\dot{q}_7 = \dot{q}_5 + \dot{q}_6$. The vector of friction parameters $\mathbf{p}^{(f)}$ is defined as

$$\mathbf{p}^{(f)} = \begin{bmatrix} \mathcal{T}_1^{(a,BL)} & c_1^{(v)} & \mathcal{T}_2^{(a,BL)} & c_2^{(v)} & \dots & \mathcal{T}_5^{(a,BL)} & c_5^{(v)} & \mathcal{T}_6^{(a,BL)} & \mathcal{T}_6^{(v,l)} & \mathcal{T}_7^{(a,BL)} & c_7^{(v)} \end{bmatrix}^T. \quad (4.28)$$

Substitution of equations (4.22) and (4.24) into equation (4.19) yields the equations of motion of the complete robot model in a parameter linear form:

$$\Phi(\ddot{\mathbf{q}}, \dot{\mathbf{q}}, \mathbf{q})\mathbf{p} = \mathcal{T}^{(m)}, \quad (4.29)$$

with

$$\Phi(\ddot{\mathbf{q}}, \dot{\mathbf{q}}, \mathbf{q}) = \left[\mathbf{D}\mathcal{F}^{(x)T}\Phi^{(l)} \quad \Phi^{(m)} \quad \mathbf{D}\mathcal{F}^{(e,c)T}\Phi^{(s)} \quad \Phi^{(f)} \right] \quad (4.30a)$$

and

$$\mathbf{p} = [\mathbf{p}^{(l)} \quad \mathbf{p}^{(m)} \quad \mathbf{p}^{(s)} \quad \mathbf{p}^{(f)}]^T. \quad (4.30b)$$

The total number of dynamic parameters in the vector \mathbf{p} becomes 82; ten inertia parameters for each of the six robot links, six motor inertias, two spring parameters and fourteen temperature dependent friction parameters.

4.3 Experimental parameter identification

The robot identification techniques make use of the property that the equations of motion can be formulated in a parameter linear form. The first step in the experimental parameter identification involves measuring the joint motion and torque data during the motion of the robot along an optimised trajectory $q(t)$. The data is recorded at a constant sample rate, yielding a vector of measured robot joint torques which is denoted by $\check{\mathcal{T}}^{(m)}$. The $\check{\cdot}$ indicates that measured values are considered.

In the second step, a linear system of equations with the 82 unknown parameters in the parameter vector p is constructed by evaluating the equations of motion and the recorded joint torques in n points along the trajectory:

$$\mathbf{A}p = \mathbf{b} + \rho, \quad (4.31)$$

where \mathbf{A} is known as the regression matrix, defined by

$$\mathbf{A} = \begin{bmatrix} \Phi_1(q_1, \dot{q}_1, \ddot{q}_1) \\ \vdots \\ \Phi_n(q_n, \dot{q}_n, \ddot{q}_n) \end{bmatrix}, \quad (4.32)$$

and the vector \mathbf{b} contains the measured joint torques

$$\mathbf{b} = \begin{bmatrix} \check{\mathcal{T}}_1^{(m)} \\ \vdots \\ \check{\mathcal{T}}_n^{(m)} \end{bmatrix}. \quad (4.33)$$

The vector ρ is the vector of residual joint torques.

The third and final step is to find an estimation \hat{p} of the unknown parameter values that minimises the residue between the simulated and measured robot response. The property that the equations of motion can be formulated in a parameter linear form allows the use of linear regression techniques, such as linear least squares. The estimate \hat{p} according to the least squares solution is found by solving the minimisation problem

$$\hat{p} = \arg \min_p \|\rho\|_2^2, \quad (4.34)$$

where $\|\rho\|_2 = \sqrt{\rho_1^2 + \rho_2^2 + \cdots + \rho_n^2}$ is known as the ℓ^2 -norm of vector ρ .

4.3.1 The linear least squares problem

The linear least squares (LS) problem for the identification of the robot model parameters is defined as a minimisation problem in which the residue ρ between the simulated and measured robot response is minimised. The linear least squares problem, equation (4.34), can then be stated as

$$\hat{\mathbf{p}} = \arg \min_{\mathbf{p}} \|\mathbf{A}\mathbf{p} - \mathbf{b}\|_2^2, \quad (4.35)$$

with $\mathbf{p} \in \mathbb{R}^m$, $\mathbf{A} \in \mathbb{R}^{6n \times m}$ and $\mathbf{b} \in \mathbb{R}^{6n}$. The number of unknown parameters in \mathbf{p} is given by m and n denotes the number of points along the identification trajectory in which the joint torques have been recorded.

The solution to equation (4.35) is found by setting the partial derivative of $\|\mathbf{A}\mathbf{p} - \mathbf{b}\|_2^2$ with respect to \mathbf{p} equal to zero, which leads to the so-called *normal equations*:

$$\mathbf{A}^T(\mathbf{A}\hat{\mathbf{p}} - \mathbf{b}) = \mathbf{0}. \quad (4.36)$$

Solving the normal equations yields an estimate $\hat{\mathbf{p}}$ of the unknown parameter vector. The mathematical solution of the normal equations can be found as follows

$$\mathbf{A}^T\mathbf{A}\hat{\mathbf{p}} = \mathbf{A}^T\mathbf{b}, \quad (4.37)$$

leading to

$$\hat{\mathbf{p}} = (\mathbf{A}^T\mathbf{A})^{-1}\mathbf{A}^T\mathbf{b}, \quad (4.38)$$

provided that the inverse $(\mathbf{A}^T\mathbf{A})^{-1}$ exist, which is only the case if the regression matrix \mathbf{A} has full rank. Obviously, the matrix \mathbf{A} depends on the excitation trajectory $\mathbf{q}(t)$.

To avoid loss of rank, the excitation trajectory has to be sufficiently exciting and an adequate number of samples n along the trajectory has to be taken into account. Even when that is accounted for, investigation of the regression matrix \mathbf{A} for the LS problem at hand reveals that it is rank deficient:

$$\text{rank}(\mathbf{A}) = r < m. \quad (4.39)$$

As a consequence, solving the normal equations by means of the matrix inverse $(\mathbf{A}^T\mathbf{A})^{-1}$ is not possible.

At the root of the rank deficiency of the regression matrix \mathbf{A} is the fact that not all parameters contribute to the joint torques. Even with an excitation trajectory that is sufficiently exciting there are still some link inertial parameters which do not contribute to joint torques. This is because of the restricted motion near the robot base, e.g. the rotational inertias $J_{xx}^{(1)}$ and $J_{yy}^{(1)}$ of link 1. The matrix column \mathbf{a}_j associated with such a parameter p_j has then an Euclidian norm equal to zero, $\|\mathbf{a}_j\|_2 = 0$. Furthermore, there are some columns of the regression matrix that are linearly dependent. This is caused by the fact that the associated parameters contribute to the joint torques in a similar manner. For instance, the contribution of the motor inertia $J^{(m,1)}$ of joint 1 and the rotational inertia $J_{zz}^{(1)}$ of link 1 both depend only on the acceleration \ddot{q}_1 of the first joint.

Several authors have addressed the problem of the rank deficiency of the regression matrix, including Khosla and Kanade (1985) and Atkeson et al. (1986). Methods based on a complete symbolic robot model have been developed for serial link manipulators. They are either based on the recursive Newton-Euler formulation (Gautier and Khalil, 1988) or on the Lagrangian formulation (Mayeda et al., 1998). In these methods the parameters that do not make any contribution to the joint torques are removed from the parameter vector. The parameters associated with linear dependent columns are gathered into single parameters. The definition of a new parameter vector ensures a regression matrix which has full rank under the condition that the trajectory is sufficiently exciting. Note that these methods become quite cumbersome when a gravity compensating spring, joint friction and motor inertias are added.

The more general techniques are the numerical methods, based on a decomposition of the regression matrix (Gautier, 1990; Sheu and Walker, 1991; Antonelli et al., 1999). Decompositions such as the Singular Value Decomposition (SVD) of matrix \mathbf{A} are commonly used to analyse and solve linear least squares problems with rank deficiency of the regression matrix \mathbf{A} , see Lawson and Hanson (1974); Golub and Van Loan (1983). The application of the singular value decomposition in the dynamic identification has been demonstrated by An et al. (1988); Gautier (1990); Sheu and Walker (1991); Shome et al. (1998); Khalil and Dombre (2002). In this thesis, the singular value decomposition will also be employed to solve and analyse the rank deficient least squares problem.

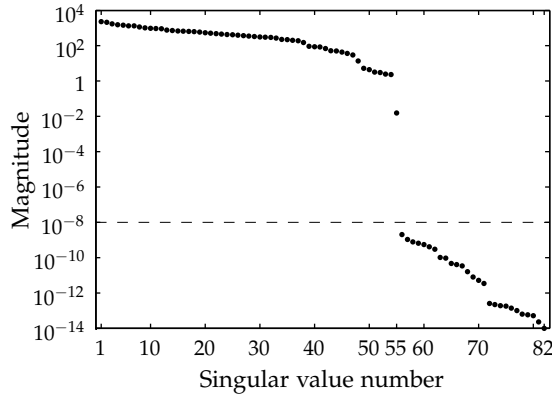


Figure 4.3: The magnitude of the singular values $\sigma_i(\mathbf{A})$, denoted by (\bullet) compared to the value of 10^{-8} of the precision at which the regression matrix was evaluated, indicated by $--$.

4.3.2 Solving the LS problem by singular value analysis

The singular value decomposition decomposes a matrix $\mathbf{A} \in \mathbb{R}^{6n \times m}$ into the form

$$\mathbf{A} = \mathbf{U}\mathbf{\Sigma}\mathbf{V}^T, \quad (4.40)$$

where $\mathbf{U} \in \mathbb{R}^{6n \times 6n}$ and $\mathbf{V} \in \mathbb{R}^{m \times m}$ are orthogonal matrices, known as the left and right singular matrices, respectively. When $6n > m$, matrix $\mathbf{\Sigma} \in \mathbb{R}^{6n \times m}$ is structured as follows

$$\mathbf{\Sigma} = \begin{bmatrix} \mathbf{S} \\ \mathbf{0} \end{bmatrix}, \quad (4.41)$$

where $\mathbf{S} = \text{diag}(\sigma_1, \sigma_2, \dots, \sigma_m)$ contains the singular values σ_i of \mathbf{A} on its diagonal and where $\sigma_1 \geq \sigma_2 \geq \dots \geq \sigma_m \geq 0$. For a typical sufficiently exciting trajectory and a sufficiently large number of samples n , the numerically evaluated singular values of the regression matrix of the least squares problem at hand are shown in figure 4.3. As a threshold for zero singular values the value 10^{-8} is used. This is the precision that is used in the SPACAR software for the evaluation of the regression matrix \mathbf{A} . It is clear that only 55 singular values are nonzero. The other 27 singular values can be considered zero. The number of nonzero singular values

equals the rank $r = \text{rank}(\mathbf{A}) = 55$ and as $r < m$ the matrix \mathbf{A} is rank deficient. Accordingly, the diagonal matrix with the singular values \mathbf{S} can be split into a nonzero part $\mathbf{S}_1 \in \mathbb{R}^{r \times r}$ and a zero part $\mathbf{S}_2 \in \mathbb{R}^{(m-r) \times (m-r)}$ as follows

$$\mathbf{S} = \begin{bmatrix} \mathbf{S}_1 & \mathbf{0} \\ \mathbf{0} & \mathbf{S}_2 \end{bmatrix}. \quad (4.42)$$

The left and right singular matrices are partitioned in the same way, yielding

$$\mathbf{U} = [\mathbf{U}_1 \quad \mathbf{U}_2], \quad (4.43)$$

$$\mathbf{V} = [\mathbf{V}_1 \quad \mathbf{V}_2], \quad (4.44)$$

where $\mathbf{U}_1 \in \mathbb{R}^{6n \times r}$, $\mathbf{U}_2 \in \mathbb{R}^{6n \times (6n-r)}$, $\mathbf{V}_1 \in \mathbb{R}^{m \times r}$ and $\mathbf{V}_2 \in \mathbb{R}^{m \times (m-r)}$.

With the right singular matrix, the parameter vector \mathbf{p} can be orthogonally transformed as follows

$$\mathbf{p} = \mathbf{V}\boldsymbol{\alpha} \quad (4.45)$$

and partitioning gives

$$\mathbf{p} = \mathbf{V}_1\boldsymbol{\alpha}^{(E)} + \mathbf{V}_2\boldsymbol{\alpha}^{(N)}, \quad (4.46)$$

where $\boldsymbol{\alpha}^{(E)}$ denotes the *essential* parameter vector, containing the 55 parameters that can be estimated independently. The vector $\boldsymbol{\alpha}^{(N)}$ is associated with the so-called *null space*:

$$\mathbf{0} = \mathbf{U}_2 \begin{bmatrix} \mathbf{S}_2 \\ \mathbf{0} \end{bmatrix} \boldsymbol{\alpha}^{(N)}, \quad (4.47)$$

for any vector $\boldsymbol{\alpha}^{(N)}$ as \mathbf{S}_2 is zero.

A similar orthogonal transformation can be carried out with the left singular matrix \mathbf{U} . Multiplication of both sides of equation (4.31) with the transpose of \mathbf{U} yields

$$\mathbf{U}^T \boldsymbol{\rho} = \mathbf{U}^T \mathbf{A} \mathbf{p} - \mathbf{U}^T \mathbf{b}. \quad (4.48)$$

Substitution of the singular value decomposition of \mathbf{A} , equation (4.40), gives

$$\mathbf{U}^T \boldsymbol{\rho} = \mathbf{U}^T \mathbf{U} \boldsymbol{\Sigma} \mathbf{V}^T \mathbf{p} - \mathbf{U}^T \mathbf{b}. \quad (4.49)$$

Substitution of equation (4.45) gives

$$\mathbf{U}^T \boldsymbol{\rho} = \begin{bmatrix} \mathbf{S} \\ \mathbf{0} \end{bmatrix} \boldsymbol{\alpha} - \mathbf{g}, \quad (4.50)$$

where the vector \mathbf{g} is defined as

$$\mathbf{g} = \mathbf{U}^T \mathbf{b}. \quad (4.51)$$

An important property of orthogonal matrices is the preservation of Euclidian length upon multiplication. This implies that instead of minimising $\|\boldsymbol{\rho}\|_2^2$ it is possible to minimise $\|\mathbf{U}^T \boldsymbol{\rho}\|_2^2$. Accordingly, the original LS problem, equation (4.35), is replaced by

$$\hat{\boldsymbol{\alpha}} = \arg \min_{\boldsymbol{\alpha}} \left\| \begin{bmatrix} \mathbf{S} \\ \mathbf{0} \end{bmatrix} \boldsymbol{\alpha} - \mathbf{g} \right\|_2^2. \quad (4.52)$$

Since \mathbf{S} is diagonal, the effect of each component of $\boldsymbol{\alpha}$ on the residual norm is immediately obvious. Introducing a component α_i with the value

$$\hat{\alpha}_i = \frac{g_i}{\sigma_i}, \quad (4.53)$$

reduces the sum of squares of the residuals $\|\boldsymbol{\rho}\|_2^2$ by the amount of g_i^2 . The solution of the transformed LS problem of equation (4.52) can now be written as

$$\hat{\alpha}_i^{(E)} = \frac{g_i}{\sigma_i}, \quad \text{for } i = 1, 2, \dots, r, \quad (4.54)$$

where obviously only the nonzero singular values are used. The residue vector that remains is then given by

$$\boldsymbol{\rho} = \sum_{i=r+1}^{6n} \mathbf{u}_i g_i, \quad (4.55)$$

where the vector \mathbf{u}_i denotes the i^{th} column of the left singular matrix \mathbf{U} .

Using equation (4.46), the estimate $\hat{\boldsymbol{\alpha}}$ as obtained partly in equation (4.54) can be transformed to the estimate $\hat{\mathbf{p}}$ in the physical parameter space according to

$$\hat{\mathbf{p}} = \mathbf{V}_1 \hat{\boldsymbol{\alpha}}^{(E)} + \mathbf{V}_2 \hat{\boldsymbol{\alpha}}^{(N)}, \quad (4.56)$$

which has an infinite number of solutions because it follows from equation (4.47) that $\hat{\boldsymbol{\alpha}}^{(N)}$ can have any value $\hat{\boldsymbol{\alpha}}^{(N)} \in \mathbb{R}^{m-r}$. Setting $\hat{\boldsymbol{\alpha}}^{(N)} = \mathbf{0}$

yields an estimate for the essential parameter vector expressed in the physical parameter space:

$$\hat{\mathbf{p}}^{(E)} = \mathbf{V}_1 \hat{\mathbf{a}}^{(E)}. \quad (4.57)$$

The fact that the null space $\hat{\mathbf{a}}^{(N)}$ may have any value in \mathbb{R}^{m-r} without affecting the joint torque, enables manipulation of the physical parameter vector $\hat{\mathbf{p}}$. In general, the essential parameter vector does not yield parameter values that can be considered physically convincing. The null space can then be used to obtain an equivalent solution $\hat{\mathbf{p}}$ which includes more physically convincing parameter values.

In a situation where *a priori* knowledge of the parameter values is available, e.g. an estimate from a CAD model, the values can be stored in the vector $\mathbf{p}^{(F)}$. Then it is possible to define the next minimisation problem:

$$\hat{\mathbf{a}}^{(N)} = \arg \min_{\mathbf{a}^{(N)}} \|\hat{\mathbf{p}} - \mathbf{p}^{(F)}\|_2^2, \quad (4.58)$$

which leads to an estimate $\hat{\mathbf{a}}^{(N)}$ that minimises the difference between $\hat{\mathbf{p}}$ and $\mathbf{p}^{(F)}$. Substitution of equation (4.56) into the normal equations which solve the LS problem (4.58) yields

$$\mathbf{V}_2^T \left(\mathbf{V}_2 \hat{\mathbf{a}}^{(N)} - (\mathbf{p}^{(F)} - \mathbf{V}_1 \hat{\mathbf{a}}^{(E)}) \right) = \mathbf{0}, \quad (4.59)$$

which have the solution

$$\hat{\mathbf{a}}^{(N)} = \mathbf{V}_2^T (\mathbf{p}^{(F)} - \mathbf{V}_1 \hat{\mathbf{a}}^{(E)}). \quad (4.60)$$

4.3.3 Error analysis of the LS problem

In order to study the sensitivity of the least squares solution $\hat{\mathbf{p}}$ to perturbations on the elements of \mathbf{A} and \mathbf{b} the following system (Golub and Van Loan, 1983) is considered

$$\mathbf{b} + \delta \mathbf{b} = (\mathbf{A} + \delta \mathbf{A}) \hat{\mathbf{p}}, \quad (4.61)$$

where the least squares solution is given by $\hat{\mathbf{p}} = \mathbf{p} + \delta \mathbf{p}$. The perturbation bounds on parameter errors are then given by

$$\frac{\|\delta \mathbf{p}\|_2}{\|\mathbf{p}\|_2} \leq \kappa_2(\mathbf{A}) \frac{\|\delta \mathbf{b}\|_2}{\|\mathbf{b}\|_2} \quad \text{with } \delta \mathbf{A} = \mathbf{0} \quad (4.62)$$

and

$$\frac{\|\delta\mathbf{p}\|_2}{\|\mathbf{p} + \delta\mathbf{p}\|_2} \leq \kappa_2(\mathbf{A}) \frac{\|\delta\mathbf{A}\|_2}{\|\mathbf{A}\|_2} \quad \text{with } \delta\mathbf{b} = \mathbf{0}, \quad (4.63)$$

where $\kappa_2(\mathbf{A})$ is known as the condition number. For rank deficient LS problems and application of the ℓ^2 -norm, the condition number $\kappa_2(\mathbf{A})$ equals the ratio between the largest $\sigma_1(\mathbf{A})$ and smallest nonzero singular value $\sigma_r(\mathbf{A})$:

$$\kappa_2(\mathbf{A}) = \frac{\sigma_1(\mathbf{A})}{\sigma_r(\mathbf{A})}, \quad (4.64)$$

where $r = \text{rank}(\mathbf{A})$. As a consequence, small condition numbers are desirable as the perturbations then have minimal influence on the overall estimation error. Note that the errors δa_{ij} on \mathbf{A} in equations (4.62) and (4.63) must be of the same size (Gautier and Khalil, 1992). This requires that matrix \mathbf{A} must be normalised by means of column norm scaling, see section 4.3.4, before the condition number is computed.

If perturbations $\delta\mathbf{A}$ on \mathbf{A} become large, the use of the Maximum Likelihood Estimation (MLE) technique instead of linear least squares is more appropriate (Swevers et al., 1996; Olsen and Petersen, 2001). Perturbations on \mathbf{A} are caused by stochastic measurement noise and systematic errors—such as controller tracking errors—of the joint positions, velocities and accelerations. Olsen et al. (2002) states that the MLE is reduced to a linear least squares problem if measurement noise on the joint positions, velocities and accelerations can be neglected. In this thesis, matrix \mathbf{A} is computed using the reference values of the joint positions, velocities and accelerations. Consequently, application of linear least squares is justified as long as errors between the actual joint angles (and derivatives) and the reference joint angles (and derivatives) are small. This will be verified in section 4.4.1. It is expected, however, that on one hand the motion errors will be small due to the fact that the robot has a high tracking accuracy and on the other hand the measurement errors will be small because of the joint motion data is directly taken from the digital servo amplifiers.

The sensitivity to perturbations can also be analysed by looking at the influence of the variance of the estimation residual $\text{var}(\boldsymbol{\rho})$ on the covariance matrix of the least squares estimates (Kozłowski, 1998; Antonelli et al., 1999). The unbiased variance s^2 of the estimation residual is defined as

$$s^2 = \text{var}(\boldsymbol{\rho}) = \frac{1}{6n - r} \sum_{i=1}^{6n} \rho_i^2, \quad (4.65)$$

where $\text{rank}(\mathbf{A}) = r$ is the number of estimated parameters. Note that it is assumed that the contributions of the 6 joints have been properly scaled. The variance $\text{var}(\hat{\alpha}_i)$ of a least squares estimate $\hat{\alpha}_i$ for a rank deficient problem, $r < m$, can be written as

$$\text{var}(\hat{\alpha}_i) = \frac{s^2}{\sigma_i^2}, \quad (4.66)$$

where σ_i is the i^{th} singular value. This expression shows that an error of order $\mathcal{O}(s)$ in \mathbf{g} will typically lead to an error in the estimate $\hat{\alpha}$ of the order $\mathcal{O}(s/\sigma)$. It can be concluded that a large smallest singular value with respect to the noise in the measurement vector \mathbf{g} is preferred. However, in many cases the signal-to-noise ratio is not sufficient enough to produce an accurate estimate and the noise in the measurement vector \mathbf{g} combined with a small singular value will then lead to large errors in the parameter vector.

A well known technique is the so-called truncated or partial SVD method (Lawson and Hanson, 1974). While keeping in mind that the singular values are sorted in descending order, it is possible to even further reduce the number of singular values r that is taken into account regarding the solution of the LS problem, expressed in equation (4.54), so taking $r < \text{rank}(\mathbf{A})$. Typically it is then a matter of finding a proper number of singular values r that needs to be taken into account in such a way that influence of noise in g_r on a value for parameter $\hat{\alpha}_r$ is acceptably small. This can be accomplished by having the singular value σ_r that is sufficiently large with respect to the noise level and verifying that the contribution of g_{r+1}^2 to the sum of squared residuals $\|\boldsymbol{\rho}\|_2^2$ is sufficiently small. In other words, if a value for r is taken too small it will lead to large residues and erroneous model parameters and if a value for r is taken too large it will lead to a so-called overfit; there is reduction of the residue and the parameter values lose their physical meaning.

4.3.4 Scaling of the least squares problem

In the experimental identification problem at hand it is necessary to scale the LS problem because the measurement vector \mathbf{b} includes the measured signals of six joints. In order to balance the range of these six signals, scaling by means of left multiplication of \mathbf{A} and \mathbf{b} is needed. Furthermore, scaling by means of right multiplication of \mathbf{A} may be applied either to

balance the Euclidean norm of the regression matrix columns or to level the numerical values of the parameters to be estimated.

Scaling by means of left multiplication of \mathbf{A} and \mathbf{b}

In order to include the six joints in an even way in the LS problem, a scaling operation based on the maximum joint torque will be applied. This is achieved by means of left multiplication of \mathbf{A} and \mathbf{b} by a diagonal matrix \mathbf{L} , which is actually a row-scaling operation. Application of the diagonal scaling matrix \mathbf{L} changes the minimisation problem of equation (4.35) into

$$\hat{\mathbf{p}} = \arg \min_{\mathbf{p}} \|\mathbf{L}\mathbf{A}\mathbf{p} - \mathbf{L}\mathbf{b}\|_2^2, \quad (4.67)$$

where \mathbf{L} is defined as

$$\mathbf{L} = \begin{bmatrix} \text{diag}(\mathcal{T}^{(max)})^{-1} & \dots & \mathbf{0} \\ \vdots & \ddots & \vdots \\ \mathbf{0} & \dots & \text{diag}(\mathcal{T}^{(max)})^{-1} \end{bmatrix}^{6n \times 6n}. \quad (4.68)$$

Vector $\mathcal{T}^{(max)}$ contains the six maximum joint torques. For the remainder of this chapter, both the matrix \mathbf{A} and the measurement vector \mathbf{b} denote the row-scaled versions, $\mathbf{L}\mathbf{A}$ and $\mathbf{L}\mathbf{b}$, respectively.

Scaling by means of right multiplication of \mathbf{A}

Scaling of the LS problem by means of right multiplication is accomplished as follows

$$\mathbf{b} = \overline{\mathbf{A}}\overline{\mathbf{p}} + \boldsymbol{\rho}, \quad (4.69)$$

where

$$\overline{\mathbf{p}} = \mathbf{H}^{-1}\mathbf{p}, \quad (4.70)$$

$$\overline{\mathbf{A}} = \mathbf{A}\mathbf{H}. \quad (4.71)$$

A technique that is often used to improve the numerical condition of the regression matrix \mathbf{A} is balancing the Euclidian norms of its columns. A scaling matrix $\mathbf{H}^{(C)}$ is then defined as a diagonal matrix with components $h^{(C)}$ set as follows:

$$h_{ii}^{(C)} = \begin{cases} \|\mathbf{a}_i\|_2^{-1} & \text{if } \|\mathbf{a}_i\|_2 \neq 0 \\ 1 & \text{if } \|\mathbf{a}_i\|_2 = 0 \end{cases} \quad (4.72)$$

where \mathbf{a}_i denotes the i^{th} column vector of \mathbf{A} .

This column scaling technique does indeed yield a better condition number for matrix \mathbf{A} . However, according to Lawson and Hanson (1974), improving the condition number in this way may lead to unnecessary and large estimation errors due to bad signal-to-noise ratios.

Taking an alternative approach in stead of scaling can be motivated as follows. Without scaling, the covariance matrix of the least squares estimate probes the absolute parameter error. Due to the fact that the range in parameter values can be large—the parameter vector includes inertia parameters, a stiffness and a pre-tension parameter, and also the friction parameters—the parameters with large numerical values will be estimated more accurately than parameters with small numerical values. In order to have a parameter estimate with equal relative errors, scaling based on parameter values has been proposed by Lawson and Hanson (1974) and Kozłowski (1998). Consequently, a scaling matrix $\mathbf{H}^{(P)}$ is chosen to be a diagonal matrix with the diagonal components equal to the expected values of $\hat{\mathbf{p}}$.

The components $h_{ij}^{(P)}$ of the scaling matrix $\mathbf{H}^{(P)}$ are then defined as follows

$$h_{ij}^{(P)} = \begin{cases} p_i^{(F)} & \text{for } i = j \text{ and } i = 1, 2, \dots, m \\ 0 & \text{for } i \neq j. \end{cases}, \quad (4.73)$$

where $\mathbf{p}^{(F)}$ include the *a priori* estimation of the inertia parameters that was provided by Stäubli. Although these values are known to be incomplete, they should be sufficient for use regarding the normalisation. The zero values in the first estimates $\mathbf{p}^{(F)}$ are replaced by 10^{-3} in order to prevent elimination of the associated dynamics. For the friction parameters in $\mathbf{p}^{(F)}$ the values obtained in chapter 3 are taken as a logical first estimate.

The result of scaling with the first estimates $\mathbf{p}^{(F)}$ is that the values of the estimates of the new parameter vector $\bar{\mathbf{p}}$ will be close to 1 and as a consequence the magnitude of a singular value σ_i will be close to the value of g_i . This allows for a direct comparison of the singular values with the magnitude of the error in \mathbf{g} , which will be used to determine the number of singular values r that should be taken into account in the truncated SVD method, see section 4.4. Furthermore, the singular value σ_i gives a direct indication of the significance of the associated parameter α_i in the dynamics of the robot. Accordingly, the scaling with the *a priori* estimation of the parameters will be employed in this thesis.

4.4 Identification experiments

4.4.1 Experiment design

In experimental robot identification, the unknown model parameters are estimated from the measured response during an identification experiment. It is undisputed that reliable and accurate identification of the model parameters requires specially designed experiments. When designing an identification experiment it is essential that the trajectory is sufficiently exciting so that an accurate estimation can be carried out regardless of the presence of disturbances, such as measurement noise and unmodelled dynamic behaviour. Furthermore, in order to prevent the excitation of vibrations due to flexibilities, it will be desired to control the frequency contents of the identification trajectory.

The problem of finding exciting trajectories for the identification has been discussed in several publications. In general, the excitation trajectory is parameterised and subsequently the trajectory parameters are obtained by means of optimisation. First, the trajectory optimisation is discussed.

Excitation trajectory optimisation

An overview of different criteria that have been used for the optimisation of the excitation trajectory has been given by Kozłowski (1998). A well known optimisation criterion is the condition number $\kappa_2(\mathbf{A})$ of matrix \mathbf{A} (Gautier and Khalil, 1992; Swevers et al., 1997). This optimisation criterion is a logical choice with respect to the error analysis given in the first part of section 4.3.3. However, since the regression matrix needs to be scaled on column norm, it contradicts with the need to scale on parameter values. Furthermore, the column norm $\|\mathbf{a}_i\|_2$ can be seen as the magnitude of excitation of parameter p_i . So it can be concluded that normalisation of matrix \mathbf{A} by scaling on column norm removes information regarding the level of excitation of a certain parameter from the regression matrix.

An optimisation criterion which is based on the error analysis by means of the parameter covariance matrix, see section 4.3.3, is then a more logical choice. The analysis shows that a large smallest singular value is desirable. Consequently, the trajectory optimisation problem can be defined as

$$\hat{\mathbf{p}}^{(t)} = \arg \min_{\mathbf{p}^{(t)}} \left(\frac{1}{\sigma_r(\mathbf{A})} \right), \quad (4.74)$$

where $\mathbf{p}^{(t)}$ is the vector of trajectory parameters and $\sigma_r(\overline{\mathbf{A}})$ is the smallest nonzero singular value of the matrix $\overline{\mathbf{A}}$ which has been scaled in such a way that the parameter vector is normalised.

Excitation trajectory parametrisation

In the work that has been presented by Armstrong (1987) an optimal acceleration sequence is determined and then the velocity and positions are found by means of numerical integration. The drawback of this method is the difficulty of including trajectory feasibility constraints in the optimisation procedure. Another method is based on the determination of optimal joint position–velocity points, see Gautier and Khalil (1992) and Antonelli et al. (1999). By means of a fixed order polynomial through these points, a smooth interpolation function is obtained. A variation on this method is the random search of position-velocity points for the polynomial interpolation (Van der Linden and Van der Weiden, 1994).

In this thesis harmonic excitation trajectories, which have been independently introduced by both Swevers et al. (1997) and Calafiore and Indri (1998), are applied. Calafiore et al. (2001) stated that the application of harmonic trajectories does yield a sub-optimal excitation trajectory. However, harmonic excitation trajectories can be optimised in order to be sufficiently exciting. The application of harmonic excitation trajectories includes several advantages (Swevers et al., 1997):

- the possibility of time domain data averaging by measuring multiple periods, which improves the signal-to-noise ratio of the experimental data.
- the bandwidth of the excitation trajectories can be specified by means of the basic pulsation in such a way that the excitation of flexible modes can be prevented.
- the joint velocities and accelerations can be computed from the measured joint positions in an analytical way by means of Fourier transformations. The periodicity of the excitation trajectory ensures that the Fourier transform does not introduce leakage errors. Selecting the main spectral lines in the Fourier transform and differentiation in the frequency domain yields the time derivatives in a simple and accurate way.

The harmonic trajectories, i.e. finite Fourier series, are defined as:

$$q_j(t) = q_{0j} + \sum_{i=1}^h a_{ij} \sin(i\omega_0 t) + b_{ij} \cos(i\omega_0 t), \quad (4.75a)$$

$$\dot{q}_j(t) = \sum_{i=1}^h a_{kj} i\omega_0 \cos(i\omega_0 t) - b_{kj} i\omega_0 \sin(i\omega_0 t), \quad (4.75b)$$

$$\ddot{q}_j(t) = \sum_{i=1}^h -a_{kj} i^2 \omega_0^2 \sin(i\omega_0 t) - b_{kj} i^2 \omega_0^2 \cos(i\omega_0 t), \quad (4.75c)$$

where h is the number of harmonics and ω_0 is the basic pulsation of the trajectory. The trajectory is parameterised by means of the amplitudes a_{ij} and b_{ij} of the sine and cosine functions and a joint angle off-set q_{0j} for each joint j . The trajectory parameters are collected in the parameter vector

$$\mathbf{p}^{(t)} = (q_{01} \quad \dots \quad q_{06} \quad a_{11} \quad a_{12} \quad \dots \quad a_{6h} \quad b_{11} \quad b_{12} \quad \dots \quad b_{6h}). \quad (4.76)$$

Note that the optimisation problem in equation (4.74) is subject to constraints on the maximum joint positions, velocities and acceleration and also subject to constraints on the position of the end-effector of the robot in order to prevent damage to the robot due to collisions. The constraint optimisation problem in equation (4.74) is nonlinear in its parameters, which makes it quite cumbersome to solve. Calafiore et al. (2001) applied a genetic algorithm in order to find the values of the trajectory parameters. Another way of determining the trajectory parameters is by means of trial and error: the trajectory parameters are chosen randomly and the random set that yields the best optimum is then selected.

In this thesis, the MATLAB (2004) `fmincon` nonlinear constraint optimisation algorithm has been used to solve the problem in equation (4.74). A typical optimisation run can take up to 12 hours until an optimum is found while the motion constraints are being obeyed. Knowing that it is almost inevitable that a local optimum will be found, the optimisation has been computed several times, each time using different randomised start values for the vector $\mathbf{p}_0^{(t)}$. The two trajectories with the smallest optimisation criterium have been selected.

The basic trajectory pulsation ω_0 is chosen as $\frac{1}{4}\pi$ rad/s. The number of harmonics h is 10, yielding a total of 126 unknown trajectory parameters. With a sample time $T = 0.04$ s (25 Hz) and a period of 8 seconds, a

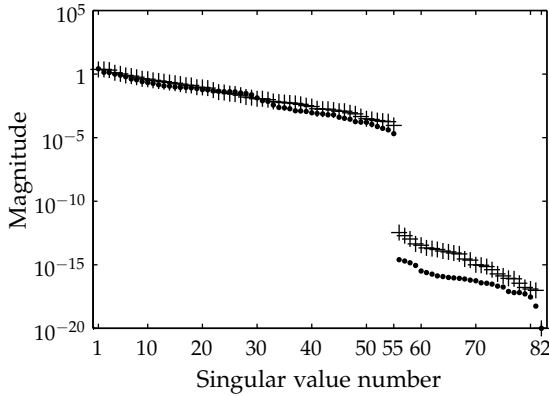


Figure 4.4: The magnitude of the singular values of both the optimised trajectory (+) and a trajectory with randomly chosen trajectory parameters (•).

total of 200 samples along the trajectory has been used for the trajectory optimisation.

In figure 4.4 the singular values σ_r of the regression matrix belonging to the optimised trajectory are compared to the singular values of the regression matrix of the trajectory before optimisation. The figure shows that the trajectory with the optimised parameters does not yield significantly higher singular values than the trajectory with the randomly chosen parameters. This will be elaborated upon in the next section.

As the robot controller needs set points at a sample rate of $T = 0.004$ s (250 Hz), the actual trajectory for the robot has been recomputed at the appropriate sample rate. In figures 4.5(a) and 4.5(c) the position and velocity during one period of the optimised excitation trajectory for all six axes have been plotted as a function of time. The actual joint positions and velocities have been recorded and their difference with the designed trajectory has been plotted as a function of time in figures 4.5(b) and 4.5(d). Note that there may be a small synchronisation error due to the step-size $T = 0.004$ s of the discrete time and the micro interpolator in the controller. The trajectory error is in the range of 0.1%, which is considered to be sufficiently small to use the designed trajectory for computing matrix \mathbf{A} and consequently it is assumed that $\delta\mathbf{A} \approx \mathbf{0}$.

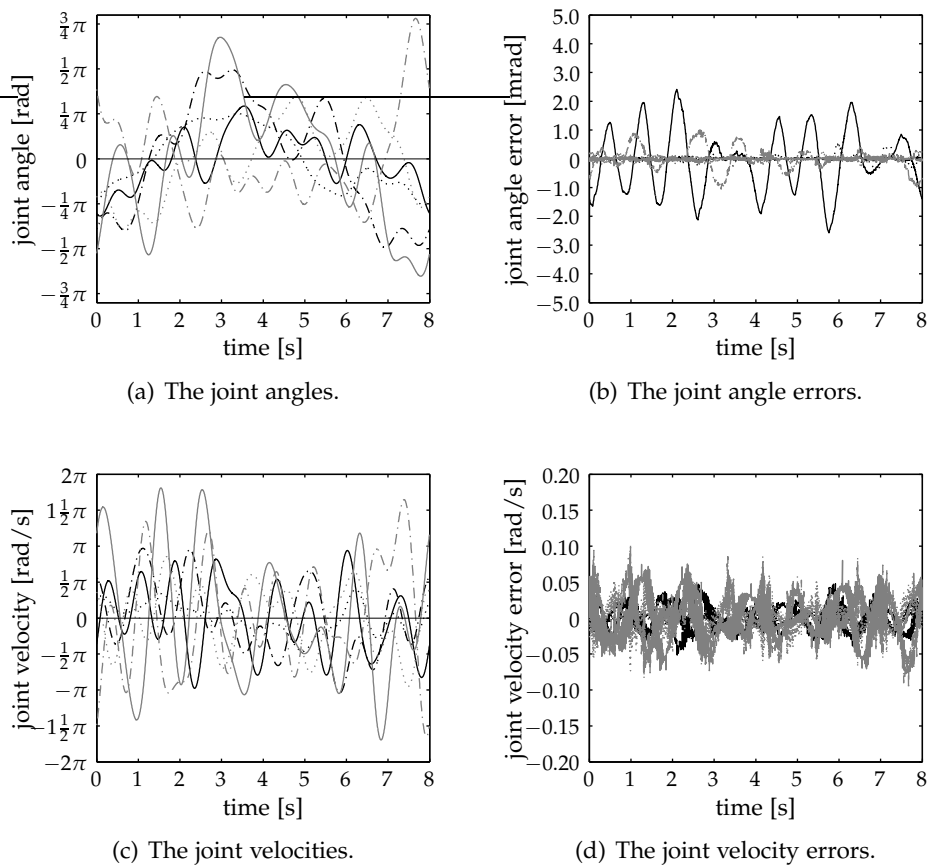


Figure 4.5: One period of the optimised excitation trajectory as a function of time. Figure (a) shows the joint angles, figure (b) shows the joint tracking errors. The joint velocities along the trajectory have been plotted in figure (c) and the velocity errors are depicted in figure (d). The six joints are denoted by — q_1 , q_2 , - - - q_3 , — q_4 , q_5 , - - - q_6 .

4.4.2 Identification of the Stäubli RX90B

The identification experiment was carried out on the Stäubli RX90B robot. The start and end of the trajectory have been filtered in order to ensure smooth motion and to reduce transients. In a single measurement, a total of 4 periods are recorded of which only the second and third period are used for the actual identification. The first and last period are disregarded as they contain the filtered parts and transients may be present in the first period. Before each measurement a warmup cycle was carried out in order to equalise the experimental conditions.

The first identification experiment involves the Stäubli RX90B without an additional payload attached. A total of 8 measurements are averaged in order to reduce stochastic noise. However, unmodelled dynamics caused by controller quantisation and drive nonlinearities are not reduced by averaging and will be present in the measured joint torques.

The next step is to determine the number r of singular values that can be estimated by means of the truncated SVD method. An effective way of determining r is to plot the square of the Euclidean norm of the residual vector $\|\rho\|_2^2$ as a function of the number r of singular values taken into account, see figure 4.6. It appears that including more than about 20 parameters does not yield a significant improvement.

In order to investigate the influence of disturbances in the measured joint torques on the estimated parameter uncertainty, the unbiased variance s^2 of the estimation residual for an estimate with all 55 parameters has been computed according to equation (4.65). From equation (4.66) it follows that the error on the estimate $\hat{\alpha}_i$ equals the standard deviation s of the estimation residual divided by the magnitude of the singular value of σ_i as the parameters are scaled. Limiting the relative error in the estimate $\hat{\alpha}_i$ to 10% implies that the value of σ_i needs to be larger than the tenfold of the standard deviation s of the estimation residual. This 10% threshold line is shown as the dashed line in figure 4.7 and from the graph it is obvious that only about 22 parameters can be estimated accurately.

Note that it was observed from figure 4.4 that the trajectory optimisation only improved the singular values in the range from 33 to 55. Combining this with the fact that only 22 parameters can be estimated accurately, it can be concluded that a trajectory optimisation has little to no effect. Apparently, a random trajectory with an adequate number of harmonics is already sufficiently exciting.

The vector of estimated parameter values $\hat{p}^{(E)}$ is computed according

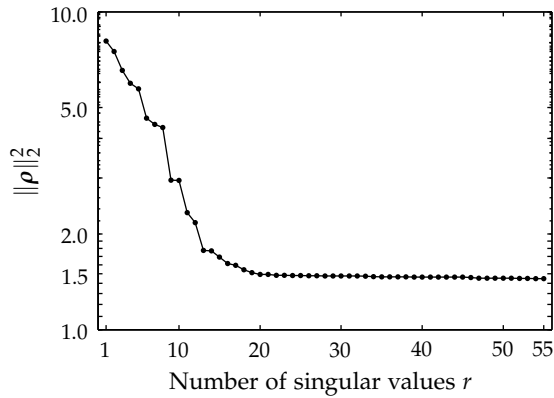


Figure 4.6: The square of the Euclidean norm of the residual vector for a specific estimate r , $\|\rho_r\|_2^2$, as a function of the number r of nonzero singular values that have been taken into account in that specific estimate.

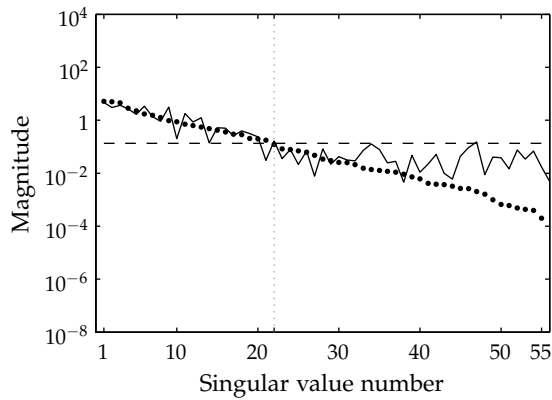


Figure 4.7: The magnitude of the singular values is indicated by (\bullet) and the continuous line ($—$) denotes the absolute value of g_i associated with the singular value σ_i . The dashed line ($- -$) represents the tenfold of the standard deviation of the estimation residual ρ . The vertical dotted line marks the number of singular values ($r = 22$) that has been taken into account in the final least squares estimate. Note that the zero singular values, $\sigma_{56\dots 82}$, have not been plotted.

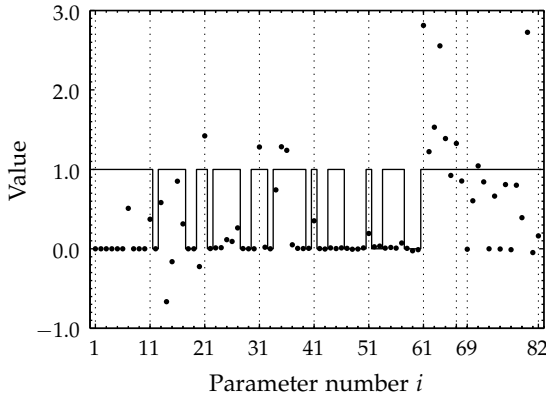


Figure 4.8: Scaled values of the estimated essential parameters $\hat{\mathbf{p}}^{(E)}$ compared to the factory parameters $\mathbf{p}^{(F)}$, denoted by (\bullet) and $(—)$, respectively. The values have been scaled with the factory parameters $\mathbf{p}^{(F)}$.

to equation (4.57). The values of the estimated parameters $\hat{\mathbf{p}}^{(E)}$ are displayed in figure 4.8. The factory parameters $\mathbf{p}^{(F)}$ are displayed in the same figure by the solid line; the value equals 1 for nonzero factory parameters, otherwise it is zero. The graph shows clearly that the parameters $\hat{\mathbf{p}}^{(E)}$ do not have true physical values.

Shaping the parameter vector towards the factory values by means of the null space, as expressed in equations (4.58) to (4.60), yields a parameter vector of an equivalent model with more realistic physical values. The values are displayed and compared to the factory values in figure 4.9.

Although the estimated parameters do not need to be the exact physical values, they clearly indicate that the factory values for the motor and transmission inertia, numbers 61 to 66, were underestimated. The values for the link inertias are in good agreement with the factory values that were obtained from CAD data. Furthermore, as a result of different temperatures, the viscous friction parameters have changed significantly compared to the values obtained in chapter 3. This clearly demonstrates the need to include the friction parameters in an inertia identification experiment.

The model based on the identified parameter set $\hat{\mathbf{p}}$, which has been estimated using 22 singular values, is referred to as model \mathcal{M}_1 . In figure 4.10 the measured and simulated joint torques have been plotted. The

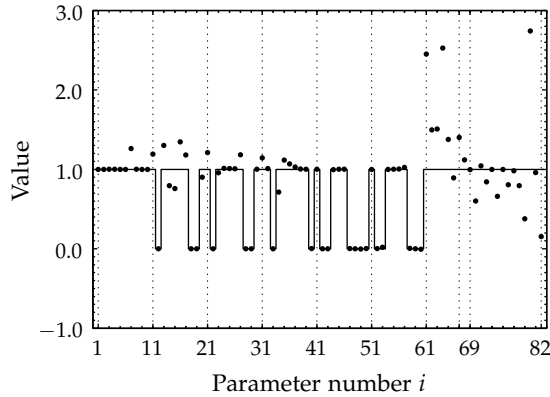


Figure 4.9: Scaled values of the estimated parameters $\hat{\mathbf{p}} = \hat{\mathbf{p}}^{(E)} + \hat{\mathbf{p}}^{(N)}$ compared to the factory parameters $\mathbf{p}^{(F)}$, denoted by (\bullet) and $(—)$, respectively. The values have been scaled with the factory parameters $\mathbf{p}^{(F)}$.

figures show that the residual torques are caused by (high frequency) unmodelled dynamics. These unmodelled dynamics are caused by the quantisation of the controller's internal signals. Additionally, nonlinearities in the robot transmission may also cause disturbances.

Figure 4.10(a) shows that there are some peaks present in the residual torque. These peaks arise at points in the trajectory where a velocity reversal occurs in the joint motion. At these velocity reversals, the friction torque makes a jump from a negative friction torque to a positive torque or vice versa, see chapter 3. Due to a small phase difference between the actual velocity and the simulated velocity, peaks in the residual torque may arise.

It is not expected that a more exciting trajectory will improve the signal-to-noise ratio enough so that more parameters can be estimated. This is motivated by the fact that increasing the level of excitation will also increase disturbances due to nonlinearities. Furthermore, trajectory tracking errors may arise. Therefore, an increase of the level of excitation may also lead to an undesirable decrease of the signal-to-noise ratio.

With a model \mathcal{M}_F based on the factory parameters $\mathbf{p}^{(F)}$ a simulation has been carried out as well. For the values of the friction parameters, the values from model \mathcal{M}_1 have been used. The results of the simulation have been plotted in figure 4.11. It is clearly visible in the residual torques

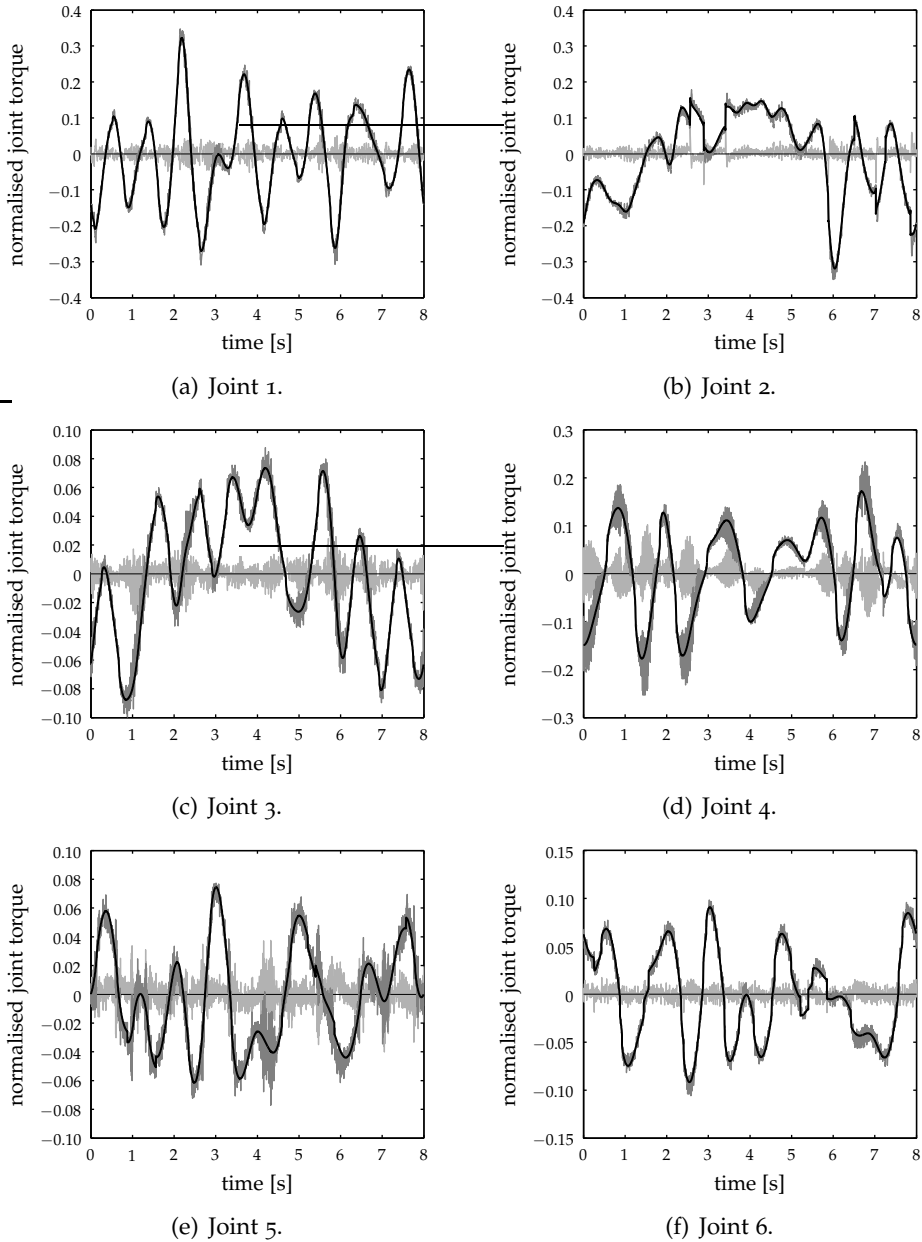


Figure 4.10: The simulated and measured joint torques along the trajectory as a function of time. The simulation has been carried out with model \mathcal{M}_1 , with: — the measured torque, — the simulated torque and — the residual torque.

that the joint torques of the lower joints (1 to 4) have been underestimated as a result of the missing transmission inertias.

4.4.3 Validation of the identification experiments

Identification using a different excitation trajectory

The identification technique will be validated first by means of an identification that has been carried out using a second harmonic excitation trajectory that has been obtained by a random selection of the trajectory parameters while the trajectory constraints are met. Again, 22 singular values have been used for this estimation. The operating temperature of the robot during the identification differed slightly from the first identification experiment, which causes a change in the friction parameter values. The robot model with the parameter values from this second identification is referred to as model \mathcal{M}_2 .

As in the first experiment, the regression matrix \mathbf{A} has been decomposed by means of the singular value decomposition analysis. Verification of the standard deviation of the estimation residual, the values of the components of vector g and the magnitude of the singular values demonstrates that for this trajectory 22 parameters can be estimated as well, with a relative accuracy of $\approx 10\%$. For this model, the null space has been found by minimising the difference between the values of model \mathcal{M}_1 and \mathcal{M}_2 as opposed to minimising the difference between the values of model \mathcal{M}_1 and the factory values. In figure 4.12, the parameter values of model \mathcal{M}_2 are compared to both the factory values and the parameters from model \mathcal{M}_1 . The figure shows that there is significant correspondence between both models. Investigation of the left singular matrix shows that the physical parameters whose values differ the most appear to be associated with the smallest singular values that were taken into account in the estimation. To visualise this effect, a graphical representation of the left singular matrix is shown in figure 4.13.

The graph clearly reveals that the physical parameters p_i whose values differ the most, $i = \{15, 16, 23, 31, 35, 36, 61, 62, 63, 67\}$ (as observed in figure 4.12), are associated with the smaller singular values σ_j , where $j = \{21, 22\}$. Figure 4.13 shows that these parameters p_i are also associated with larger singular values. It indicates that linear combinations of these parameters can be identified quite accurately, but that their mutual

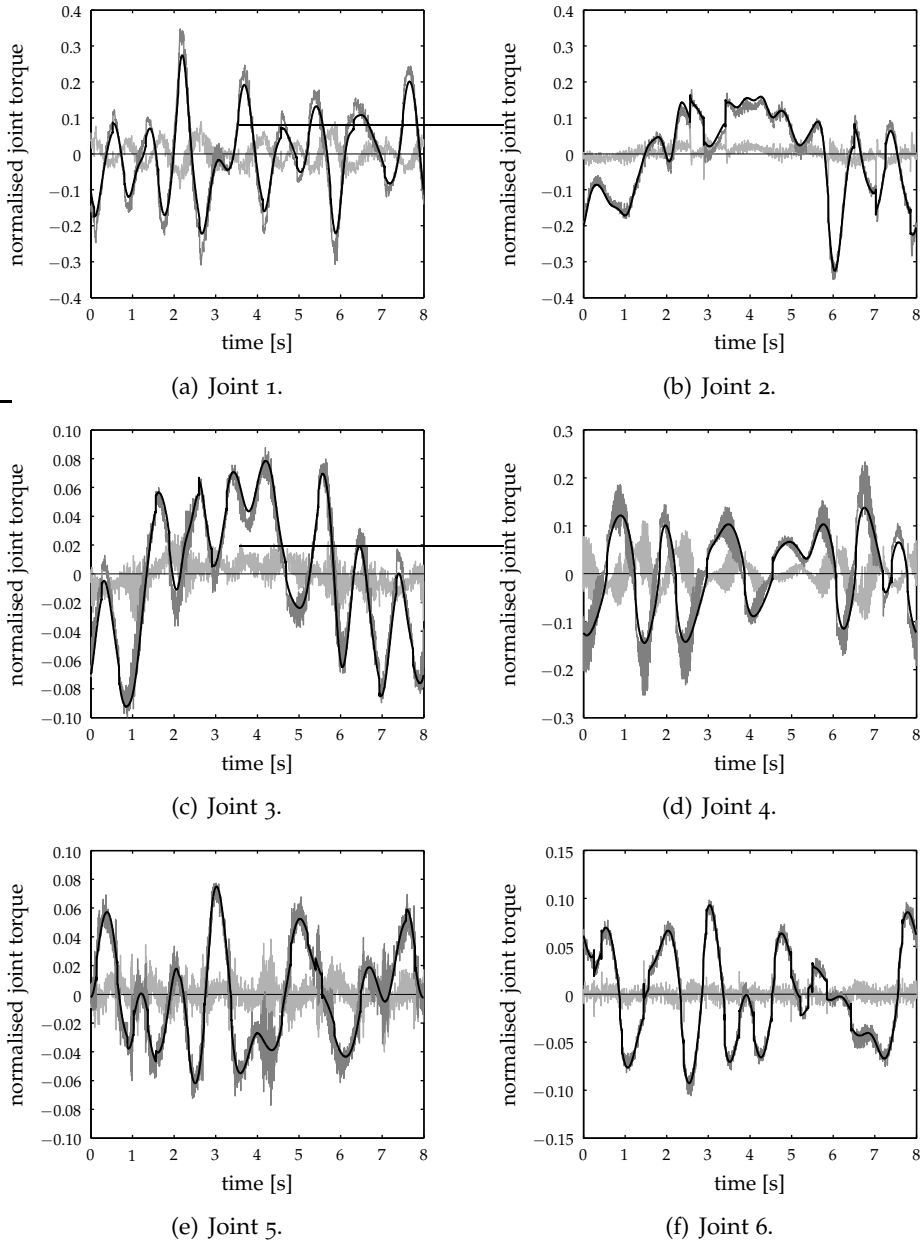


Figure 4.11: The simulated and measured joint torques along the trajectory as a function of time. The model is now based on the factory parameters \mathcal{M}_F , with: — the measured torque, — the simulated torque and — the residual torque.

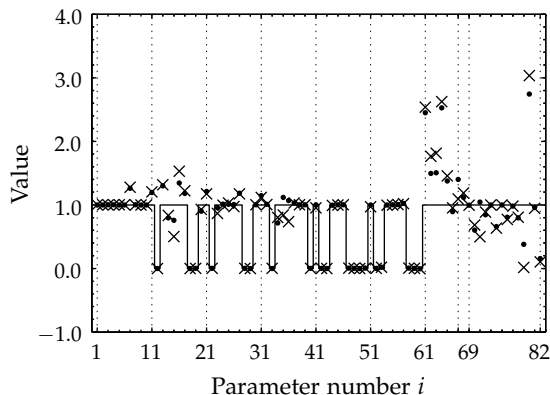


Figure 4.12: Scaled values of the parameters of the two models \mathcal{M}_1 (\bullet) and \mathcal{M}_2 (\times), estimated with different excitation trajectories. The line — denotes the factory values $\mathbf{p}^{(F)}$. The values have been scaled with the factory parameters.

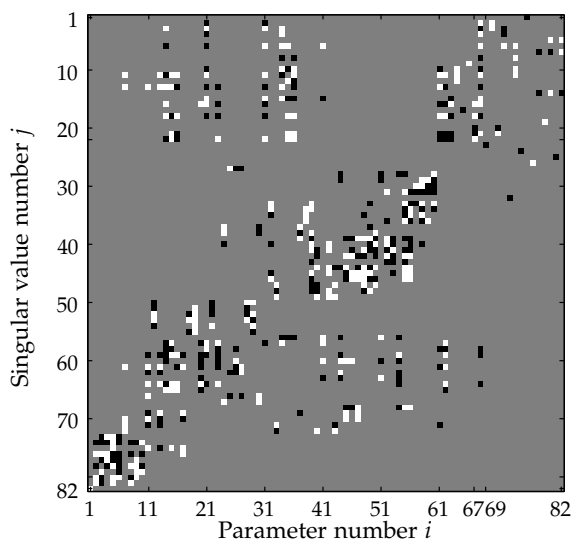


Figure 4.13: Graphical representation of the left singular matrix \mathbf{V}^T for excitation trajectory 2. The matrix shows how the physical parameters \mathbf{p} are transformed to components of vector $\boldsymbol{\alpha}$ associated to the singular values. The white squares correspond with elements $v_{ij} \geq 0.125$ and black squares correspond with matrix elements $v_{ij} \leq -0.125$. The matrix elements $-0.125 < v_{ij} < 0.125$ are displayed as grey boxes.

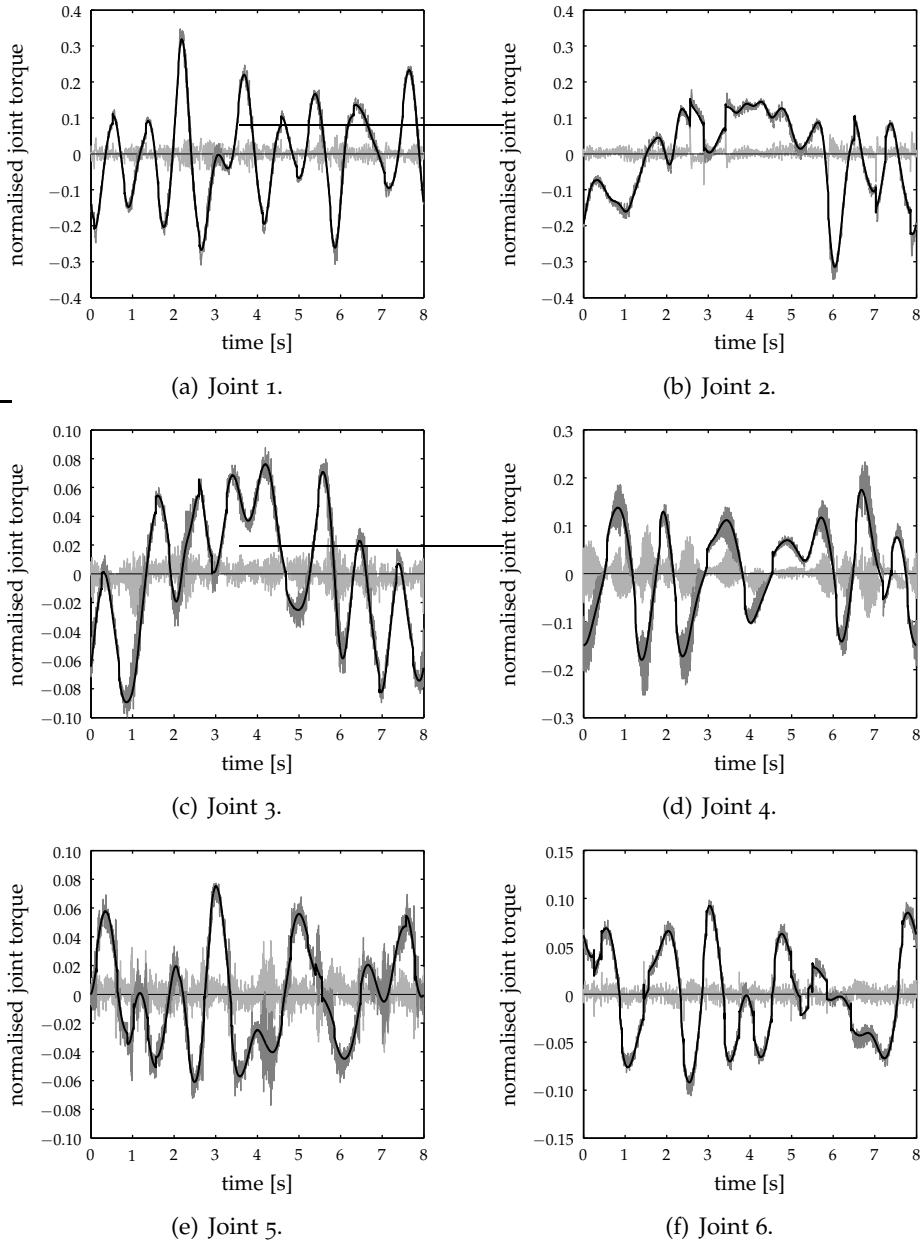


Figure 4.14: The simulated and measured joint torques along the trajectory as a function of time. The simulation has been carried out with model \mathcal{M}_2 , with: — the measured torque, - - - the simulated torque and --- the residual torque.

proportions cannot be determined accurately by means of experimental identification.

Furthermore, the graphical representation of the left singular matrix reveals that none of the inertia parameters associated with link 6 can be identified. This is clearly a result of the fact that no payload has been attached to the robot flange. The small mass of the wrist is clearly not sufficiently exciting. Note that the rotor inertia of motor 6, parameter p_{66} , can be estimated independently as it is only associated with one higher singular value σ_9 which is not associated with any other parameter p .

Figure 4.13 also shows that nearly all the parameters p_i , $i = \{69, 71, 73, 75, 77, 81\}$, for the magnitude of the asperity friction $\mathcal{T}^{(a)}$ cannot be identified, as the singular values associated with these parameters are too small. Only the value of the asperity friction $\mathcal{T}_b^{(a)}$ for the roller bearing in joint 6 can be estimated, parameter p_{79} .

With model \mathcal{M}_2 a simulation of the joint torques for trajectory 1 has been carried out. The results are shown in figure 4.14. Note that for the values of the friction parameters the values from model \mathcal{M}_1 have been used. The results show that there is again a good agreement between the measured and the simulated results, which was to be expected as the model parameters of models \mathcal{M}_1 and \mathcal{M}_2 already were largely equivalent. It can be concluded that accurate identification results can be obtained from a different sufficiently exciting identification trajectory. Furthermore, it proves that the obtained parameter values result in an accurate general applicable dynamic robot model.

Identification of a second Stäubli RX90B

A second Stäubli RX90B, stationed at Stäubli Faverges, France, has been identified using the excitation trajectory 2. The dynamic model obtained is indicated by \mathcal{M}_b . The estimation residual for a estimate with 22 parameters appeared to be slightly higher for this robot due to larger disturbances on the torque of joint 4. As a result of these disturbances, which were probably caused by controller dynamics, the estimation error associated with the smallest singular value taken into account is a bit higher than 10%. The estimated parameter values of models \mathcal{M}_b and \mathcal{M}_2 are compared to each other in figure 4.15. The values of the inertia parameters related to the smaller singular values show some small differences.

The values of most viscous friction parameters are smaller for the robot at the Stäubli factory in comparison with the robot at the University

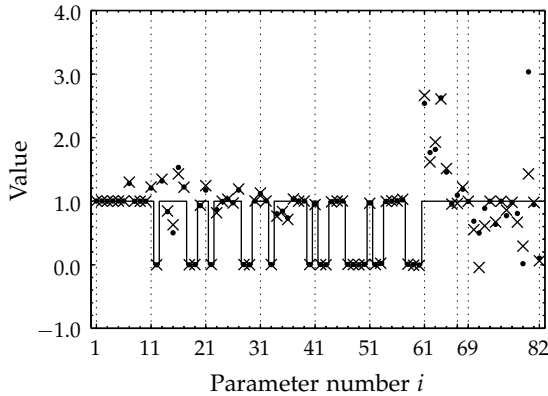


Figure 4.15: Scaled values of the estimated parameters (\times) of the Stäubli RX90B at Stäubli Faverges, France, compared to the estimated parameters (\bullet) of the Stäubli RX90B at the University of Twente. The line — denotes the factory values $\mathbf{p}^{(F)}$. The values have been scaled with the factory parameters $\mathbf{p}^{(F)}$.

of Twente. The difference in the friction parameters is mainly due to the fact that the robot at the Stäubli factory had been running for significantly more time than the robot at the University of Twente. The values for the nonlinear friction model parameters have been chosen in order to be identical to the values obtained for the robot at the University of Twente.

It is to be expected that the powers $\delta^{(a)}$ and $\delta^{(v)}$ are very much the same for both robots, as they are mainly determined by the geometry of the joints and transmissions. The parameter for the Stribeck velocity $\dot{q}^{(s)}$ will be somewhat different as it includes the standard deviation of the height of surface summits $\sigma^{(s)}$, see section 3.3.2. The standard deviation of the height of surface summits will most likely change as a function of the time that the robot has been operating. In order to investigate this assumption, a detailed analysis of the friction characteristics of the second robot should be carried out. Fortunately, a change in the parameter for the Stribeck velocity $\dot{q}^{(s)}$ will not cause any problems for the identification as the parameters for the asperity friction cannot be determined in this identification experiment.

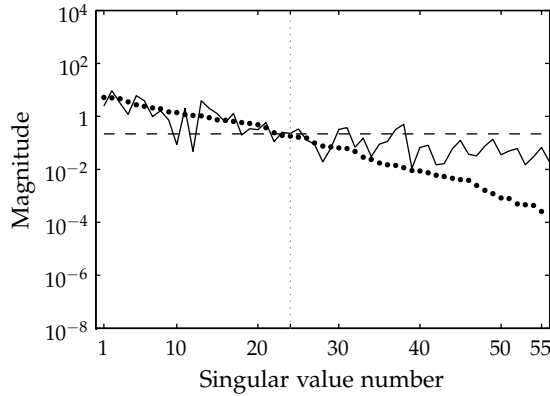


Figure 4.16: The magnitude of the singular values (\bullet) for the identification of the robot with a payload and absolute value of g_i (—) associated with the singular value σ_i . The dashed line (—) represents the tenfold of the standard deviation of the estimation residual ρ . The vertical dotted line marks the number of singular values ($r = 24$) that has been taken into account.

4.4.4 Identification of the Stäubli RX90B with a payload

A dynamic model of the robot with a laser welding head as payload needs to be obtained for the dynamic simulations that will be carried out in chapter 5. The identification experiment with the robot and attached laser head has been carried out using excitation trajectory 2 because trajectory 1 would have caused collisions.

A CAD model of the laser welding head was used to obtain a first estimation of the inertia parameters. The mass of the welding head of 4.12 kg was verified by weighing it on scales. This extra mass will increase the amplitude of the joint torques. Furthermore, the singular values associated with the LS problem will change as a result of scaling with the adapted *a priori* estimation of the parameters.

Again, the number of singular values that can be taken into account in the solution of the LS problem is determined by comparing their magnitudes to the standard deviation of the estimation residual, see figure 4.16. It is now possible to estimate 24 singular values with sufficient accuracy, as the increase in inertia also increased the signal-to-noise ratio of the associated inertia parameters.

The graph of the left singular matrix, depicted in figure 4.18, shows that most inertia parameters $p_{51\dots60}$ of link 6—that now includes the payload—are associated with larger singular values and are now included in the estimation.

The identified parameters are depicted for \mathcal{M}_3 in figure 4.17. The identified values of the inertia parameters of the payload correspond well with the values that were determined from the CAD data, e.g. the mass for the payload found in the identification is 3.99 kg, which differs only 3% from the real mass. This difference can, on one hand, be caused by identification errors or, on the other hand, it can be due to differences in the values of motor constants between the model and the actual robot.

Figure 4.19 shows the measured and simulated joint torques for the identification trajectory as a function of time. It is clear that the extra mass has indeed increased the joint torques. It shows that the simulated values generally agree well with the measured values. Figure 4.19(e) shows that there is a dissimilarity between the measured joint torque and the simulated joint torque in joint 5, clearly noticeable at $t = 2.7$ s. The dissimilarity is most likely caused by the fact that the asperity friction torque in the worm-wheel gear pairs may depend on the load.

Despite the fact that the friction characteristics of the robot wrist are not accurately described in this case, the parameter values that have been identified appear to agree well with previously identified values.

4.5 Discussion

In this chapter, the modelling and identification of a six degree of freedom Staubli RX90B industrial robot has been presented. A nonlinear finite element method has been used to model the mechanical part of the robot. The equations of motion have been written in a form linear in the accelerations and in a form linear in the parameters. The latter form allows the application of linear least squares estimation techniques.

In the second part of this chapter, the experimental parameter identification has been discussed. The linear least squares technique proved to be very suitable for identification of the unknown parameters, provided that the problem is properly scaled and that the influence of disturbances is sufficiently analysed and managed.

A row scaling operation of the regression matrix is needed as the identification experiment consists of measurements of six joint torques

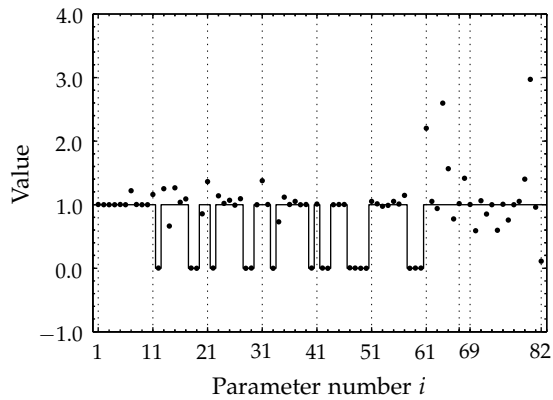


Figure 4.17: Scaled values of the parameters of model \mathcal{M}_3 (\bullet). The line — denotes the factory values $\mathbf{p}^{(F)}$. The values have been scaled with the factory parameters.

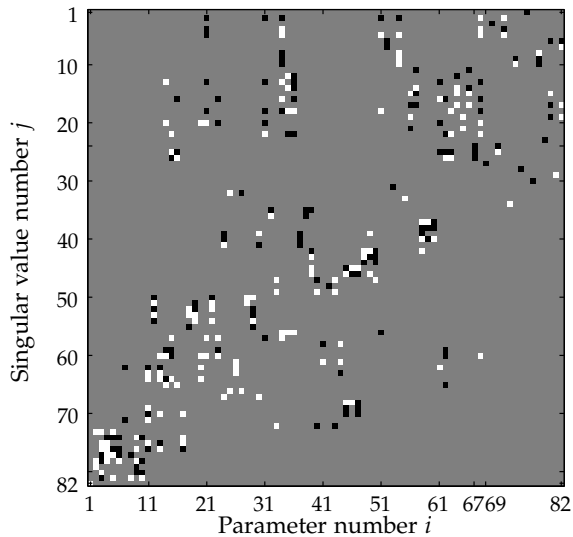


Figure 4.18: Graphical representation of the left singular matrix \mathbf{V}^T for excitation trajectory 2 and payload. The white squares correspond with elements $v_{ij} \geq 0.125$ and black squares correspond with matrix elements $v_{ij} \leq -0.125$. The matrix elements $-0.125 < v_{ij} < 0.125$ are displayed as grey boxes.

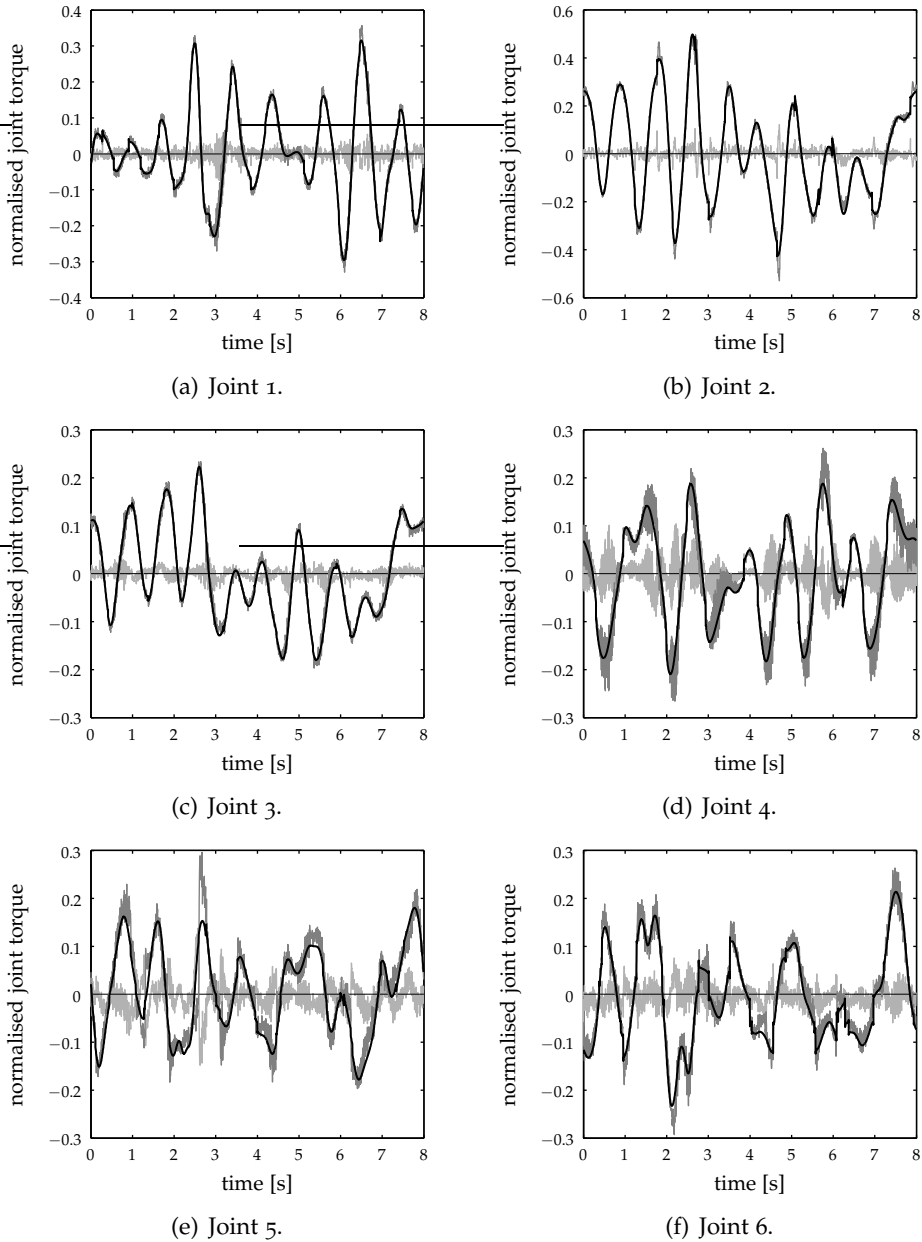


Figure 4.19: The simulated and measured joint torques along the trajectory as a function of time for the robot with a laser welding head as payload, with: — the measured torque, — the simulated torque and — the residual torque.

with a different torque range. Furthermore, a large range in parameter magnitudes gives rise to a column scaling operation. Using an *a priori* estimation of the parameter values for the column scaling operation improves the ability to analyse the influence of disturbances and it leads to parameters with equal relative accuracy.

Having all 82 unknown parameters in the model yields a rank deficient LS problem. An analysis of the least squares problem by means of a singular value decomposition has been applied to solve the problem of rank deficiency. The singular value decomposition showed that the 82 physical parameters can be transformed into 55 so-called essential parameters. Theoretically, all the essential parameters can be estimated when the measurements are both free of measurement noise and free of unmodelled dynamics. The remaining 27 parameters span the null space and have no influence on the rigid body dynamics. The estimation of the parameters by means of the truncated SVD method shows that from the original 55 essential parameters $\alpha^{(E)}$ only approximately 22 parameters can be identified in the presence of measurement noise and unmodelled dynamics. Subsequently, estimates for the null space spanned by the remaining $27 + 33 = 60$ parameters are obtained by means of minimising the difference between the physical parameters p and an *a priori* estimation of the factory parameters.

Application of random harmonic excitation trajectories generally leads to sufficiently exciting trajectories provided that the level of excitation is properly chosen. Optimisation of the excitation trajectories showed only little improvement with respect to the magnitude of the lower singular values. Considering the signal-to-noise ratio of the identification experiment, trajectory optimisation does not bring any advantages.

Validation of the experimental identification technique showed that it is robust with regard to changes in the friction conditions as friction is taken into account in the identification process. It can be concluded that accurate identification results can be obtained from a different sufficiently exciting identification trajectory. In addition, the equivalence between models \mathcal{M}_1 and \mathcal{M}_2 proves that the obtained parameter values result in an accurate dynamic robot model. Furthermore, an identification performed on a second identical robot yielded parameter values that agreed well with earlier identified parameters.

Additionally, an identification experiment has been carried out with a laser welding head as a payload attached to the robot. The mass of the payload was found to be within 3 % of the mass measured on scales. The

obtained dynamic model will be used for the simulations carried out in the following chapter.

It can be concluded that the modelling assumptions that were made with the derivation of the robot model in chapter 2 are supported by the results obtained both in chapter 3 and, to a certain extent, in this chapter as well. It has been shown that the friction effects inside a joint can be combined into a single joint friction model. The load independence of the asperity friction proved to be valid only for joints 1 to 4. However, the effect of load dependence of the friction models of the robot wrist did not have a significant influence on the identification of the model parameters.

Finally, it is concluded that dynamic robot models based on inertia parameters determined from CAD data will be sufficiently accurate, especially if the transmission inertias are properly included. The friction model parameters can be obtained by means of identification experiments that have been described in chapter 3.

With the presented finite element formulation and the identification method, a dynamic robot model has been obtained which can be applied in closedloop dynamic simulations to study the trajectory performance of typical laser welding trajectories.

Chapter 5

Dynamic simulation

5.1 Introduction

This chapter deals with dynamic robot simulations. First, the models of the robot subsystems that have been derived in the previous chapters, are assembled into a complete model of the closed-loop robot system. Then, a perturbation method will be introduced in order to make the dynamic simulations more time efficient. Motion experiments will be carried out with both the nonlinear and the perturbation models. The simulation results are then validated by means of measurements done on the actual robot while performing the motion experiments. Finally, the applicability of realistic dynamic simulations for off-line programming will be demonstrated by means of motion experiments regarding typical laser welding trajectories.

5.2 Closed-loop dynamic robot model

The models of the robot subsystems, the manipulator arm, the digital motion controller and robot drives including joint friction are assembled into a complete model of the closed-loop robot system, shown in figure 5.1. The closed-loop simulations are carried out using the graphical user interface and equation solvers of SIMULINK (2004).

The reference trajectory of the robot tip $x^{(r)}$, provided by a trajectory generator, is the input of the simulation model. The inverse kinematics block computes the associated joint angles $\varphi^{(r)}$. The six reference joint angles are fed into the motion controller where they are compared to the

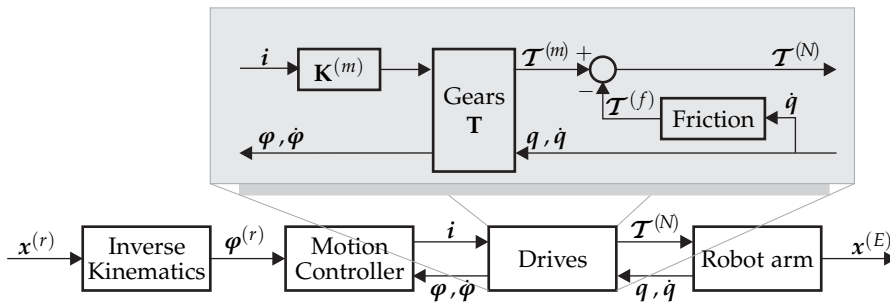


Figure 5.1: Assembly of the closed-loop robot model.

actual joint positions. The motion controller, which consists of the six SISO (Single Input Single Output) PID controllers, computes the motor currents i that are sent to the servo motors. The effects of sampling and quantisation by the AD and DA converters of the digital motion controller are taken into account in the controller model.

The vector of motor currents i acts as input for the drive model where joint torques including joint friction are computed. The friction block allows selection of either kinematic or dynamic pre-sliding behaviour. Note that the driving system shown in figure 5.1 differs slightly from the driving system model which has been presented in figure 2.7, page 21; the rotational inertia torques of the motor rotors are left out of the model of the driving system as they are included in the dynamic model of the robot arm.

The output of the driving system, the vector of net joint torques $\mathbf{T}^{(N)}$, is the input of the robot arm. The equations of motion (4.12) of the robot arm are evaluated in the SPACAR computer program. The SPACAR program is implemented as a SIMULINK block by means of a so-called *S-function* within SIMULINK (Jonker and Aarts, 1998). The S-function enables interaction with the SIMULINK equation solvers which are employed to carry out the numerical integration required for solving the equations of motion. The output of the robot arm model block may be any of the internal model variables, such as (derivatives of) nodal or deformation mode coordinates or nodal forces and can be selected by the user. In the model at hand, the outputs are the vector of joint positions \mathbf{q} and velocities $\dot{\mathbf{q}}$ and the vector $\mathbf{x}^{(E)}$ with the position and orientation of the end-effector.

The nonlinear dynamic robot simulations will be carried out with the

presented SIMULINK block scheme. In SIMULINK a variable time-step integration scheme has been selected that determines the integration time steps based on the estimated simulation accuracy (SIMULINK, 2004). In addition, the motion controller model works using discrete time steps; the position loop and the velocity loop are running at 2 kHz and 4 kHz, respectively. In SIMULINK this implies that the robot model is simulated at time steps equal to 0.25 milliseconds or even at smaller time steps if SIMULINK's integrator requires it. Unfortunately, these small time steps combined with the iterative way of computing the robot's configuration will lead to high computational loads. In order to overcome this drawback, a perturbation scheme will be presented first. This perturbation scheme has been successfully applied to simulate flexible manipulators (Jonker and Aarts, 2001, 2002).

5.3 Application of a perturbation method

In the perturbation method, deviations from the nominal motion $(q_0, \dot{q}_0, \ddot{q}_0)$ due to joint friction and limitations of the control system are modelled as first-order perturbations $(\delta q, \delta \dot{q}, \delta \ddot{q})$ of the nominal motion, so that the actual degrees of freedom q and its time derivatives are of the form

$$q = q_0 + \delta q, \quad \dot{q} = \dot{q}_0 + \delta \dot{q} \quad \text{and} \quad \ddot{q} = \ddot{q}_0 + \delta \ddot{q}, \quad (5.1)$$

where the prefix δ denotes a perturbation and the subscript 0 refers to the nominal trajectory. The vector of nodal coordinates x and its time derivatives are also written as a first order perturbation

$$x = x_0 + \delta x, \quad \dot{x} = \dot{x}_0 + \delta \dot{x} \quad \text{and} \quad \ddot{x} = \ddot{x}_0 + \delta \ddot{x}. \quad (5.2)$$

Substitution of $x = \mathcal{F}^{(x)}(q)$ and disregarding second and higher order terms results in the linear approximations

$$x = \mathcal{F}_0^{(x)}(q_0) + \mathbf{D}\mathcal{F}_0^{(x)}\delta q, \quad (5.3a)$$

$$\dot{x} = \mathbf{D}\mathcal{F}_0^{(x)}\dot{q}_0 + \mathbf{D}\mathcal{F}_0^{(x)}\delta \dot{q} + (\mathbf{D}^2\mathcal{F}_0^{(x)}\dot{q}_0)\delta q, \quad (5.3b)$$

$$\begin{aligned} \ddot{x} = & (\mathbf{D}^2\mathcal{F}_0^{(x)}\dot{q}_0)\dot{q}_0 + \mathbf{D}\mathcal{F}_0^{(x)}\ddot{q}_0 + \mathbf{D}\mathcal{F}_0^{(x)}\delta \ddot{q} + \\ & 2(\mathbf{D}^2\mathcal{F}_0^{(x)}\dot{q}_0)\delta \dot{q} + (\mathbf{D}^2\mathcal{F}_0^{(x)}\ddot{q}_0 + \mathbf{D}^3\mathcal{F}_0^{(x)}\dot{q}_0\dot{q}_0)\delta q. \end{aligned} \quad (5.3c)$$

The general principle of the perturbation method is to solve the equations of motion in two (separate) stages; a *preprocessing stage* in which the nominal motion is computed and analysed and a *simulation stage* in which the perturbations on the nominal motion are computed.

The *preprocessing stage* analyses the nominal motion $q_0(t_i)$ by an inverse dynamic computation at discrete time steps $t = t_i$, ($i = 0, 1, \dots, n$) using the nonlinear manipulator model of equation (4.12) in which the degrees of freedom are prescribed as a function of time, yielding

$$\overline{\mathbf{M}}_0^{(N)} \ddot{q}_0 + \mathbf{D}\mathcal{F}_0^{(x)T} \left[\mathbf{M}_0 \left((\mathbf{D}^2 \mathcal{F}_0^{(x)} \dot{q}_0) \dot{q}_0 \right) - f_0^{(x)} \right] + \mathbf{D}\mathcal{F}_0^{(e,c)} \sigma_0^{(c)} = \mathcal{T}_0^{(N)}, \quad (5.4)$$

where $\sigma_0^{(c)}$ is the internal force of the gravity compensating spring and $\mathcal{T}_0^{(N)}$ is the vector of nominal net joint torques. Obviously, the desired nominal motion $(\ddot{q}_0, \dot{q}_0, q_0)$ equals the reference motion $(\ddot{q}^{(r)}, \dot{q}^{(r)}, q^{(r)})$ of the closed-loop system. The reference motion is computed from the reference trajectory $x^{(r)}$ using the inverse kinematic model.

In the *simulation stage* the perturbed motion $\delta q(t)$ is computed using a set of linear time-varying (LTV) equations of motion that have been obtained by linearising the equations of motion around a number of the points on the nominal trajectory. The linear time-varying equations of motion for the perturbations of the degrees of freedom δq are

$$\overline{\mathbf{M}}_0^{(N)} \delta \ddot{q} + \mathbf{C}_0 \delta \dot{q} + (\mathbf{K}_0 + \mathbf{N}_0 + \mathbf{G}_0) \delta q = \delta \mathcal{T}^{(N)}, \quad (5.5)$$

where $\overline{\mathbf{M}}_0^{(N)}$ is the reduced system mass matrix as in equation (4.13), \mathbf{C}_0 is the velocity sensitivity matrix, \mathbf{K}_0 denotes the structural stiffness matrix, \mathbf{N}_0 and \mathbf{G}_0 are the dynamic stiffening matrix and the geometric stiffening matrix, respectively. The matrices $\overline{\mathbf{M}}_0^{(N)}$, \mathbf{K}_0 and \mathbf{G}_0 are symmetric, but \mathbf{C}_0 and \mathbf{N}_0 need not to be symmetrical. For a detailed description of the derivation of these matrices the reader is referred to Jonker and Aarts (2001). The matrices, computed at corresponding time steps, are stored in files which allows them be read at the simulation stage.

Figure 5.2 shows the SIMULINK closed-loop robot model using the perturbation scheme. The block that contains the perturbation scheme is displayed in the detailed view with the LTV-block in the centre. Its input $\delta \mathcal{T}^{(N)}$ is computed according to

$$\delta \mathcal{T}^{(N)} = \mathcal{T}^{(N)} - \mathcal{T}_0^{(N)}. \quad (5.6)$$

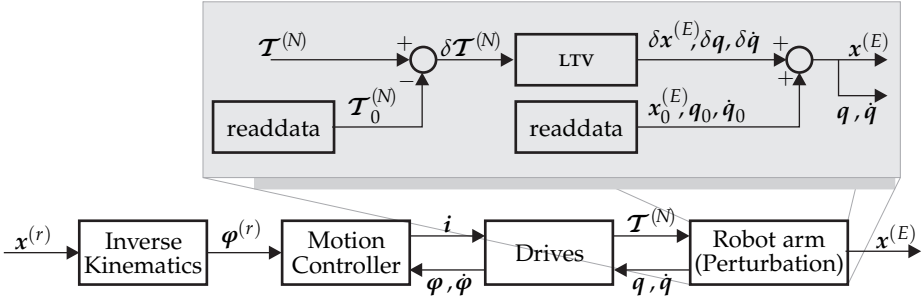


Figure 5.2: Closed-loop robot model using the perturbation scheme.

In the LTV-block the linear time-varying equations of motions, equation (5.5), are solved using a SIMULINK s-function which employs a (time-varying) state-space framework. The perturbed output vector $(\delta x^{(E)}, \delta q, \delta \dot{q})$ is added to the vector $(x_0^{(E)}, q_0, \dot{q}_0)$, yielding the actual output $(x^{(E)}, q, \dot{q})$.

In order to employ a state-space solver for the linear time-varying equations of motions, they are rewritten in the following state-space representation

$$\dot{x}_{ss} = \mathbf{A}_{ss}x_{ss} + \mathbf{B}_{ss}u_{ss}, \quad (5.7a)$$

$$y_{ss} = \mathbf{C}_{ss}x_{ss} + \frac{1}{2}(\mathbf{G}_{ss} \cdot x_{ss}) \cdot x_{ss}, \quad (5.7b)$$

where u_{ss} , y_{ss} and x_{ss} are the input, output and state vectors, respectively, and \mathbf{A}_{ss} , \mathbf{B}_{ss} and \mathbf{C}_{ss} are the time-varying state-space matrices. The usual state-space representation is supplemented with a second order term in the output equation for y_{ss} which includes a time-varying tensor \mathbf{G}_{ss} that will be explained below. First, the state and input vectors are defined as

$$x_{ss} = \begin{bmatrix} \delta q \\ \delta \dot{q} \end{bmatrix}, \quad (5.8a)$$

$$u_{ss} = \delta \mathcal{T}^{(N)}. \quad (5.8b)$$

The state-space matrices \mathbf{A}_{ss} and \mathbf{B}_{ss} are then computed from the matrices in equation (5.5) using a straightforward procedure, yielding

$$\mathbf{A}_{ss} = \begin{bmatrix} \mathbf{0} & \mathbf{I} \\ -\overline{\mathbf{M}}_0^{(N)-1} [\mathbf{K}_0 + \mathbf{N}_0 + \mathbf{G}_0] & -\overline{\mathbf{M}}_0^{(N)-1} \mathbf{C}_0 \end{bmatrix} \quad (5.9)$$

and

$$\mathbf{B}_{\text{ss}} = \begin{bmatrix} \mathbf{0} \\ \overline{\mathbf{M}}_0^{(N)-1} \end{bmatrix}. \quad (5.10)$$

The output matrix \mathbf{C}_{ss} depends on the output vector \mathbf{y}_{ss} that is defined by the user. It may consist of (first derivatives of) the degrees of freedom $\delta\mathbf{q}$ present in \mathbf{x}_{ss} or (first derivatives of) nodal coordinates $\delta\mathbf{x}$ that are computed from \mathbf{x}_{ss} using equations (5.3a) and (5.3b). Note that in this particular case, the output \mathbf{y}_{ss} is chosen to include the position of the end-effector $\mathbf{x}^{(E)}$, the joint position \mathbf{q} and the joint velocity $\dot{\mathbf{q}}$. The latter two are required for both the feedback controller and the friction model.

For kinematically highly nonlinear mechanisms and possibly large $\delta\mathbf{q}$, as is the case with the robotic manipulator at hand, the linear approximation of equation (5.3a) may be inaccurate and a second order expansion

$$\delta\mathbf{x} = \mathbf{D}\mathcal{F}_0^{(x)} \delta\mathbf{q} + \frac{1}{2}(\mathbf{D}^2\mathcal{F}_0^{(x)}\delta\mathbf{q})\delta\mathbf{q} \quad (5.11)$$

is used instead of equation (5.3a). Combining equation (5.11) and (5.7) the coordinates $\delta\mathbf{x}$ in \mathbf{y}_{ss} are computed using

$$\mathbf{C}_{\text{ss}} = \begin{bmatrix} \mathbf{D}\mathcal{F}_0^{(x)} & \mathbf{0} \end{bmatrix}, \quad (5.12)$$

$$\mathbf{G}_{\text{ss}} = \begin{bmatrix} \mathbf{D}^2\mathcal{F}_0^{(x)} & \mathbf{0} \\ \mathbf{0} & \mathbf{0} \end{bmatrix}. \quad (5.13)$$

The time varying state-space system associated with the perturbed motion is solved by SIMULINK at appropriate integration time steps. As the values of $\mathcal{T}_0^{(N)}$, $\mathbf{x}_0^{(E)}$, the state-space matrices \mathbf{A}_{ss} , \mathbf{B}_{ss} , \mathbf{C}_{ss} and the tensor \mathbf{G}_{ss} have been computed in the preprocessing stage at a number n of discrete time steps t_i , ($i = 0, 1, \dots, n$), they need to be adequately interpolated in order to prevent artificial excitation of the dynamic system. For the state-space matrices, a linear interpolation scheme has been applied that guarantees that the second order derivative $\delta\ddot{\mathbf{q}}$ will be of a continuous nature. To ensure a smooth reconstruction of the output vector $\mathbf{x}^{(E)}$, a cubic interpolation scheme (Waiboer, 1999) has been applied for $\mathbf{x}_0^{(E)}$. The interpolated values of $\mathcal{T}_0^{(N)}$ are obtained by means of the cubic interpolation scheme as well.

The application of the perturbation method is only allowed when the final motion of the dynamic system is sufficiently close to the nominal

motion. This requirement imposes two conditions on the simulations. The first condition is that the number of points in which the linearised equations of motions are computed must be sufficient with respect to the nonlinear behaviour of the robot along the nominal motion; if the robot's arm configuration changes rapidly during a certain motion, more linearisation points have to be included. The second condition is that the control system must be able to keep the final robot motion close to the nominal motion in order to assume validity for the linearised equations of motion.

5.4 Simulation experiment

In this section, both the full nonlinear closed-loop simulation model and the perturbation method will be verified by means of a dynamic simulation of the robot with a laser welding head, attached at the robot tip and moving along a reference trajectory. The motion experiment is illustrated in figure 5.3. The reference trajectory is defined as a straight line in a horizontal plane from point A to point B with a trapezoidal velocity profile as shown in figure 5.4(a). During the acceleration phase, between 1.0 s and 1.25 s, the velocity is increased to 100 mm/s according to a ramped sine function, as shown in figure 5.4(b). The acceleration profile is shown in figure 5.4(c). The orientation of the laser welding head remains aligned with the coordinate system $(x^{(t)}, y^{(t)}, z^{(t)})$ of the trajectory. The joint set-points are computed with the inverse kinematic module of the SPACAR software.

The linear motion of the laser welding head requires complex motion of the robot joints as is shown in figures 5.4(d) to 5.4(f) where the joint angles, the joint angle velocities and the joint angle accelerations have been plotted as a function of time, respectively. Note the velocity reversal of joints 2, 3 and 5 at about $t = 5.25$ s. During the motion experiment on the robot the values of the joint torques, the actual joint positions and joint velocities have been recorded at a sample rate of 250 Hz. Before the motion experiment the robot is warmed up using the same warmup sequence as was applied for the identification experiments. The warmup sequence is required to obtain the same temperature of the drives during the motion experiment as was present during the identification procedure, since the viscous friction properties strongly depend on the temperature of the drives.

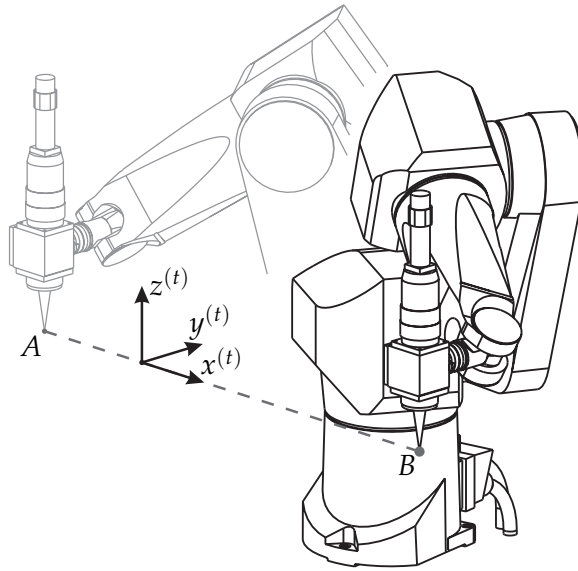
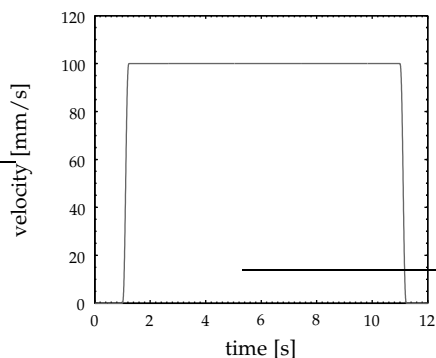


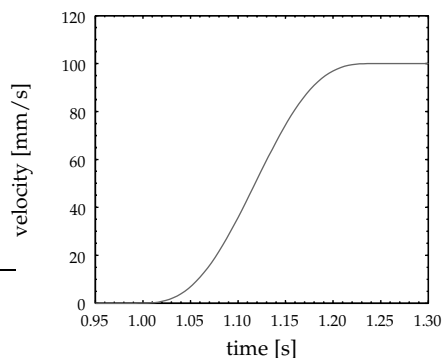
Figure 5.3: Motion experiment: the robot tip (the focal point of the laser beam) moves along a straight line from A to B at a constant velocity with a smooth acceleration and deceleration profile while keeping the orientation of the laser welding head aligned with the coordinate system $(x^{(t)}, y^{(t)}, z^{(t)})$ of the trajectory.

5.4.1 Simulation results obtained with the nonlinear robot model

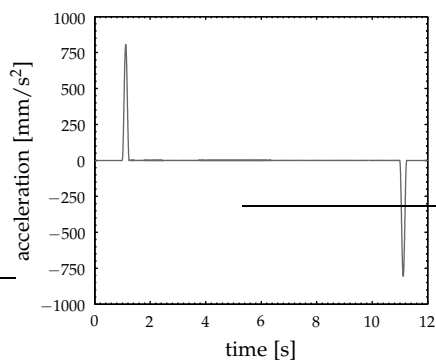
The closed-loop dynamic model is first validated by means of a dynamic simulation of the presented motion experiment using the full nonlinear model of the robot as was shown in figure 5.1. The simulation has been carried out within SIMULINK using the variable time-step `ode23t` (SIMULINK, 2004) integration scheme with the relative tolerance set to the value of 10^{-3} , whereas other settings were set to their “*auto*” defaults. The `ode23t` integration scheme is described as a dedicated solver for moderately stiff problems for which a solution is required without numerical damping (SIMULINK, 2004). Due to the fact that the friction torque rapidly reverses sign at a velocity reversal—which requires a smaller time scale of the numerical integrator—the simulation problem at hand is moderately



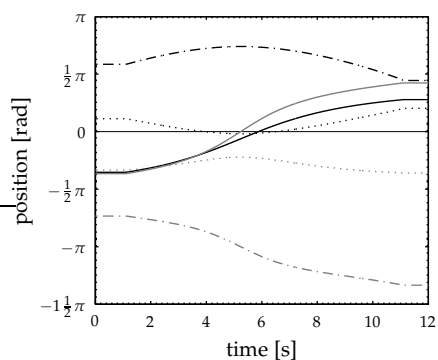
(a) Robot tip velocity at full time scale.



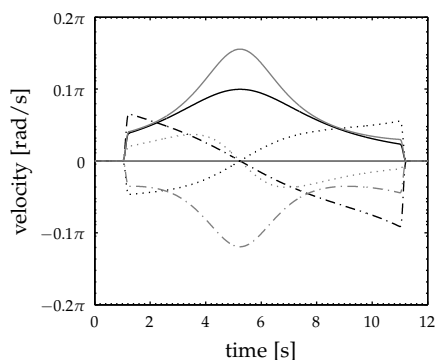
(b) Detail of the robot tip velocity during the acceleration phase.



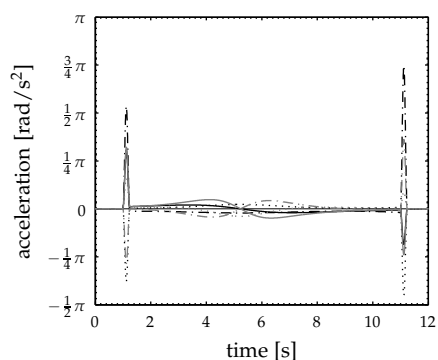
(c) Robot tip acceleration.



(d) Joint angles.



(e) Joint angle velocities.



(f) Joint angle acceleration.

Figure 5.4: Motion profiles for the straight-line motion experiment. The six joints are denoted by — q_1 , q_2 , - - - q_3 , — q_4 , q_5 , - - - q_6 .

stiff and the `ode23t` integration scheme turned out to be a time-efficient solver. SIMULINK's default variable time-step integration scheme `ode45` appeared to be incapable of managing the friction behaviour in the pre-sliding regime at the velocity reversals and at small velocities near zero. As noted in section 3.8, both the kinematic and the dynamic (LuGre) pre-sliding models show similar behaviour with respect to the simulation results. In the present simulation experiment the LuGre pre-sliding friction model has been used as it has been shown to be more time efficient than the kinematic pre-sliding model of equation (3.69), page 58.

The results of the simulation with the closed-loop robot model are validated by means of data that have been recorded on the robot while performing the motion experiment. In figure 5.5, both the measured and simulated joint position errors are shown. It is observed that there are peaks in the joint position errors at the acceleration and deceleration phases. Due to inaccurate feed forward torques and the limited bandwidth of the controller, tracking errors arise during these high accelerations and decelerations. The inaccurate feed forward is caused by the fact that the feed forward is constant—remember figures 2.4, page 17 and 2.5, page 18—and does not adapt to the nonlinear behaviour of the robot dynamics due to large configuration changes. Furthermore, the velocity feed forward does not include the complex behaviour of the joint friction. The controller bandwidth is, amongst other things, limited by the lowest natural frequencies of the robot arm, which is about 10 Hz.

The joints that have a velocity reversal in their trajectory motion, joints two, three and five, also show a peak in the joint position error near $t = 5.25$ s. These peaks are caused by the rapid changes in the joint friction torque from the maximum asperity friction torque $\mathcal{T}^{(a,BL)}$ to the minimum asperity friction torque $-\mathcal{T}^{(a,BL)}$, or vice versa, at velocity reversals. Although joint six does not have a velocity reversal along the trajectory, it shows a peak in the position error, see figure 5.5(f). This peak is caused by joint five which has a velocity reversal at $t = 5.25$ s. As there is a coupling in the driving system between joint five and joint six, the velocity reversal of joint five has an effect on the position error of joint six. The results show a clear agreement between the measurement and the simulated prediction. Although the magnitudes of the peaks at $t = \{1 \text{ s}, 5.25 \text{ s}, 11 \text{ s}\}$ in the simulation do not exactly correspond with the magnitudes of the measurements, they are still in fairly close agreement with one another.

A series of simulations that have been carried out revealed that the

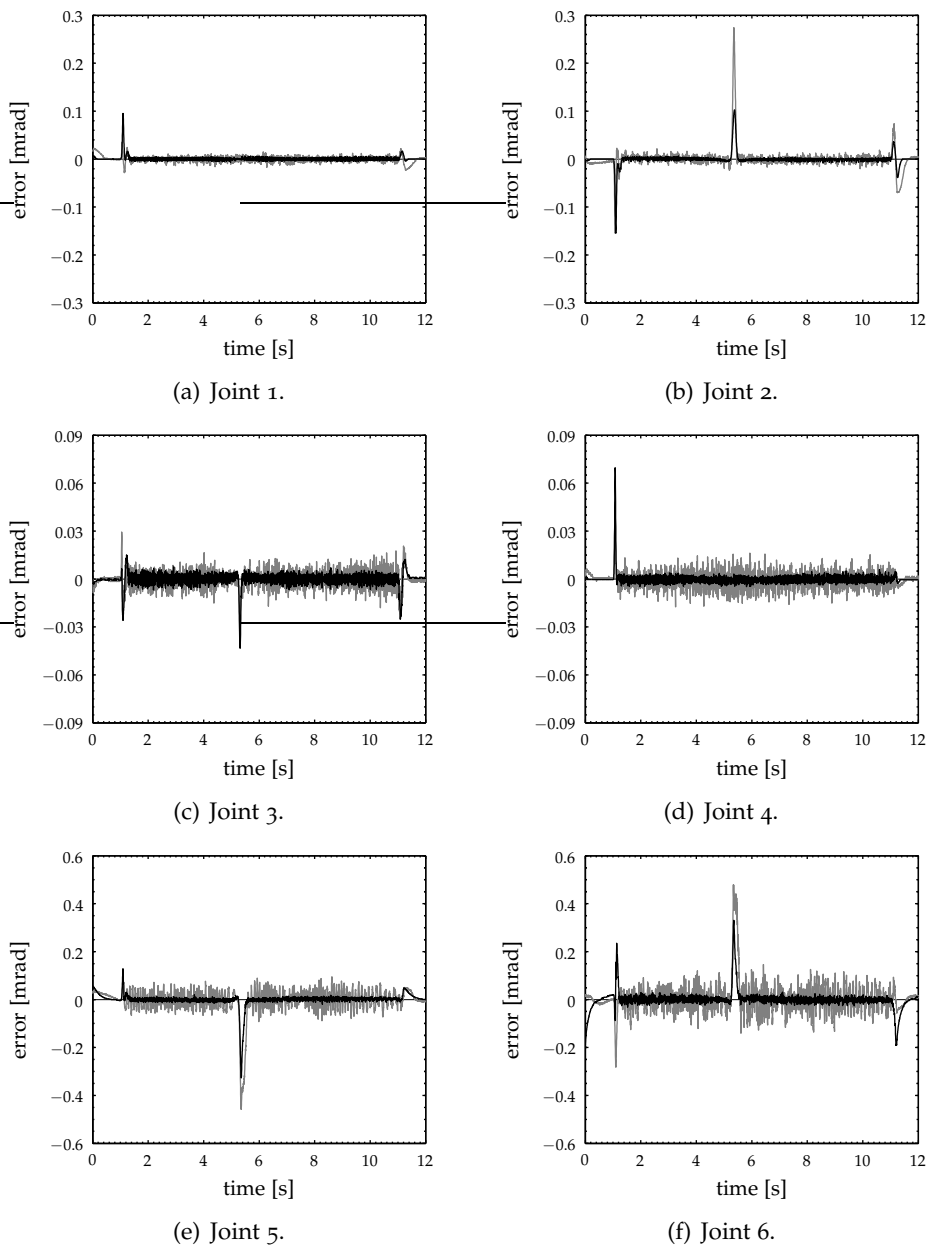


Figure 5.5: The simulated — and measured — joint angular position errors along the straight line trajectory as a function of time.

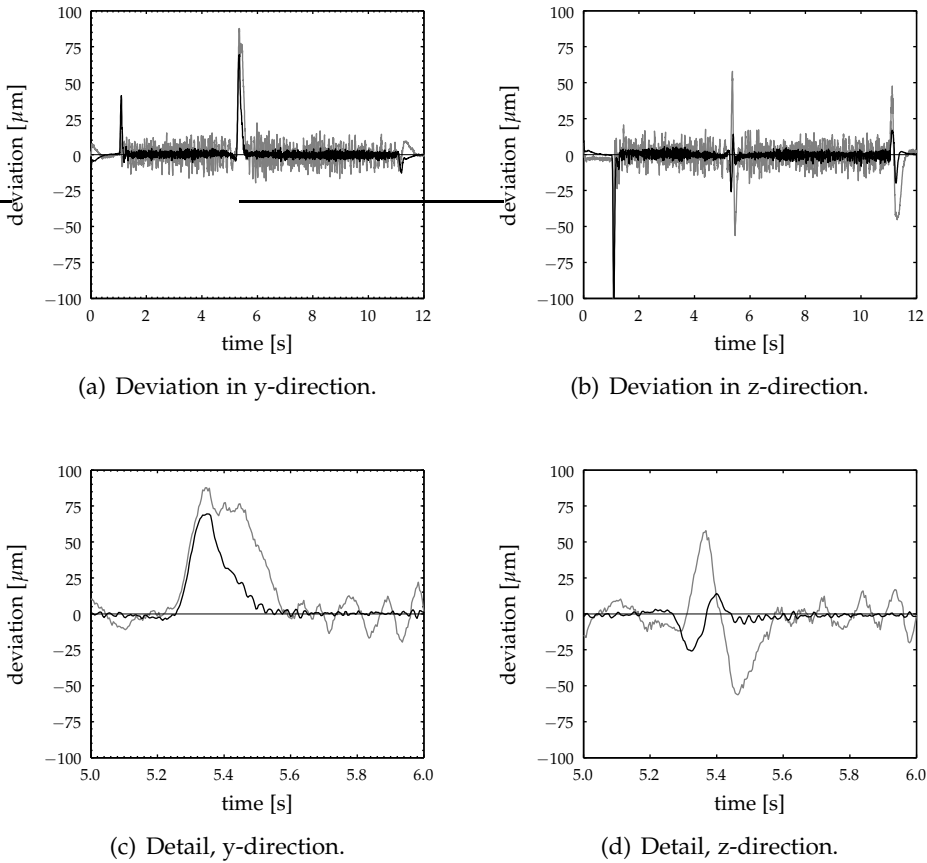


Figure 5.6: The simulated — and measured — path tracking errors of the laser welding head in the straight-line motion experiment.

height of the peaks in the joint position error is mainly determined by the interaction between the LuGre pre-sliding behaviour of the joint friction model and the controller performance; increasing the stiffness $c^{(0)}$ of the LuGre pre-sliding behaviour will give rise to larger controller errors.

The most important quality to examine for the application of laser welding is the tracking performance of the laser beam's focal point. Therefore, the lateral (y-direction) and vertical (z-direction) tracking errors have been plotted as a function of time in figure 5.6. Note that the measured and simulated path tracking errors have been determined as a function of the measured and simulated joint positions, respectively.

Again, the graphs show peaks at the acceleration and deceleration phases of the trajectory. Also, there is a peak at the moment of the velocity reversals of joints two, three and five. Figures 5.6(a) and 5.6(c) show that the simulated and the measured path tracking error correspond closely in the y-direction. In the z-direction, as shown in figures 5.6(b) and 5.6(d), the peak near $t = 5.25$ s, as computed by the simulation, deviates from the measured path tracking error. Although the simulated and measured tracking errors on joint level show a clear agreement, small discrepancies lead to larger differences at the tip of the robot. Depending on the kinematic configuration of the robot, errors at joint level translate differently to tracking errors at the robot tip. The results show that the agreement between the simulated prediction and the measurement is typically within $25 \mu\text{m}$, which is well within the required range of accuracy.

During the experiment, the motor currents are recorded. In figure 5.7 the measured motor currents are compared with the simulated motor currents. The joint torques $\mathcal{T}^{(m)}$ have been normalised with the maximum joint torque $\mathcal{T}^{(max)}$. The figures show that the simulated joint torques match the measured joint torques quite well for the major part of the trajectory. Only at the start and end of the trajectory, where the robot is at a standstill, is there a disagreement between the simulated and measured joint torques. This disagreement is caused by the pre-sliding friction behaviour. In a zero velocity situation, the required controller torque needed to keep the robot axis at its current position may be anywhere between $-\mathcal{T}^{(a,BL)}$ and $\mathcal{T}^{(a,BL)}$, depending on the moment of ‘sticking’ of the pre-sliding friction. Any small difference between the actual pre-sliding behaviour and the model then leads to differences in the steady state torque.

Figures 5.7 show that the joint torques are only of the order of 10% of the maximum joint torques, so the trajectory is not very demanding. The major part of the joint torque is caused by joint friction. Torques caused by acceleration and deceleration represent only a small portion of the total joint torques. The joint torques in joint five and six show larger differences between the simulated and the measurement joint torques. One of the causes for these discrepancies is that the friction behaviour of the worm-wheel gears are load dependent. Additionally, the worm-wheel gears that drive joints five and six may become self-locking. This means that the friction between the teeth gets higher than the load force from the wheel. As a consequence, the servo motor ‘feels’ no static load from the joint.

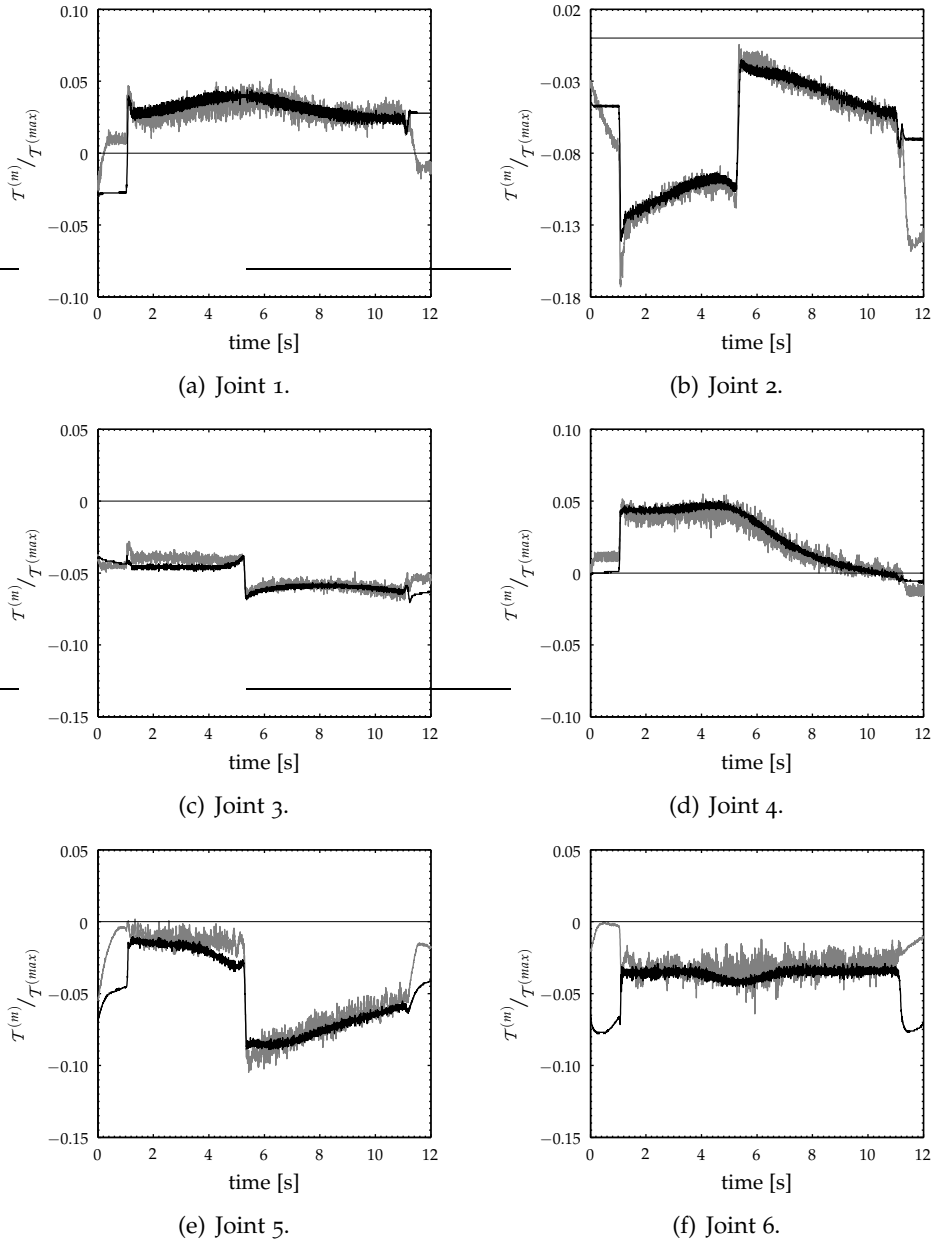


Figure 5.7: The simulated — and measured — joint torques along the straight line trajectory as a function of time.

The simulation results show that the closed-loop dynamic robot model is sufficiently accurate to be used to predict the path tracking accuracy of the robot since the differences between simulation and measurement are within the accuracy range that is required for laser welding. The required CPU time needed for the simulation of the 12 second trajectory was approximately 60 minutes when carried out on a Pentium-IV 2.4 GHz PC. This is caused by the small time steps in which the manipulator configuration needs to be solved by an iterative method. To overcome this drawback, the perturbation method will be applied next.

5.4.2 Simulation results obtained with the perturbation method

For the simulations discussed in this section, the block-scheme of the full nonlinear model, figure 5.1, is replaced by the block-scheme of the perturbation method, figure 5.2. For the perturbation method the number of points along the trajectory n at which the system is linearised is chosen to be 300. The simulation results of the perturbation method and the nonlinear simulation have been compared. Figure 5.8 shows the difference between the simulated path tracking errors using the perturbation method and the nonlinear method of figure 5.6. There is no noticeable difference between the results at this scale. The difference stays well below $10\ \mu\text{m}$ and is mostly less than $2\ \mu\text{m}$, which is small compared to the overall accuracy of the simulations (figure 5.6).

The simulated motor currents for both the nonlinear simulation and the perturbation are plotted for joints 1 and 6 in figure 5.9. It shows that the differences in joint torque are very small, mostly within 0.1% of the maximum joint torque. The larger differences in joint torque appear at the parts of the trajectory where the joints are at rest. This illustrates the high sensitivity of the pre-sliding model to small differences in the joint positions and velocities.

The application of the perturbation method appears to reduce the simulation time significantly; the simulation time that was achieved equals 60 seconds, which is 5 times real-time. The simulation times that have been achieved by the perturbation method are sufficiently short to apply realistic dynamic simulations in off-line programming software. Furthermore, the simulations have shown to be sufficiently accurate to be used in predicting the path tracking accuracy. In order to demonstrate the applicability of realistic dynamic simulations for off-line programming, several typical welding trajectories are evaluated in the next section.

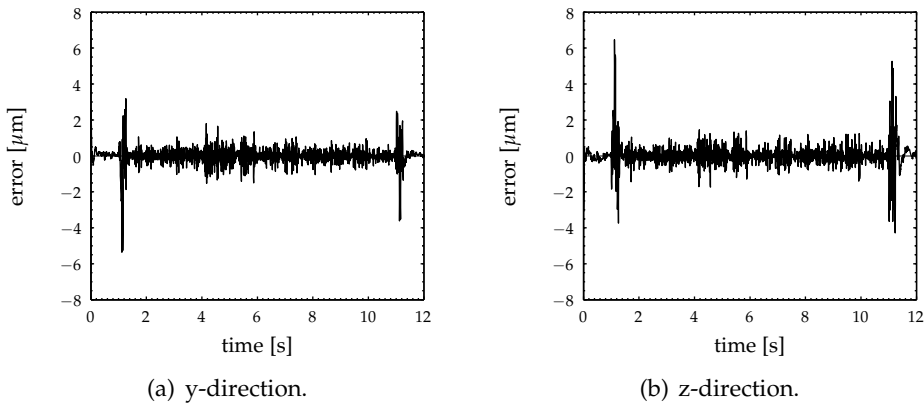


Figure 5.8: The difference between the simulated path tracking errors using the perturbation method and the nonlinear method of figure 5.6.

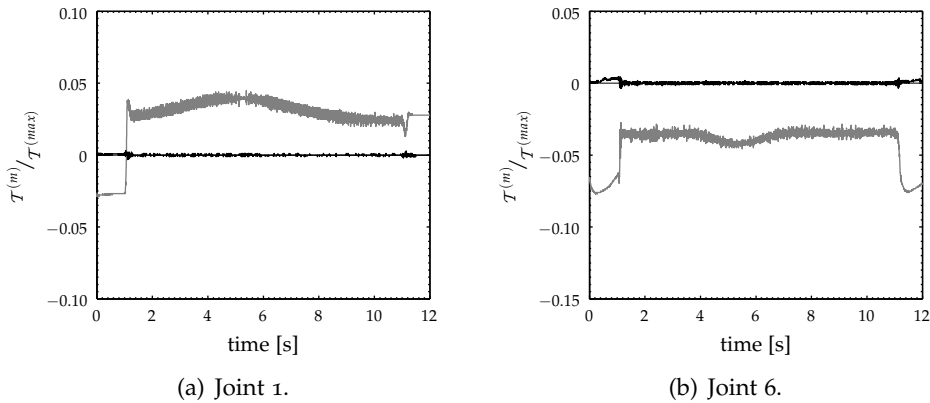


Figure 5.9: The simulated joint torques for joint 1 and 6 using the perturbation method, indicated by —. The difference between the nonlinear simulation and the perturbation method is indicated by —. The results are similar for the other joints.

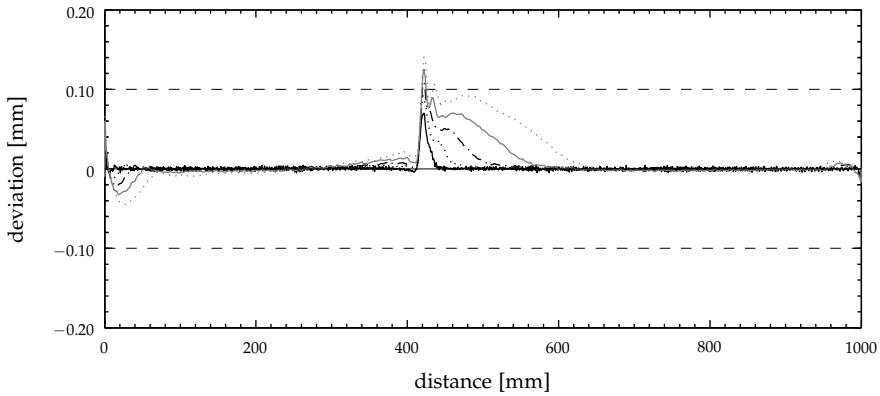
5.5 Off-line programming and dynamic simulations

The application of realistic dynamic simulations for the support of off-line programming will be demonstrated on the basis of three typical weld seams; the straight line, a 90° corner without change in orientation of the welding head and a 90° corner with the orientation of the welding head following the orientation of the seam. These trajectories will be performed with increasing velocities, up to the point where the tracking errors become too large for the laser welding application. The simulated path tracking errors will be compared to the actual measured path tracking errors.

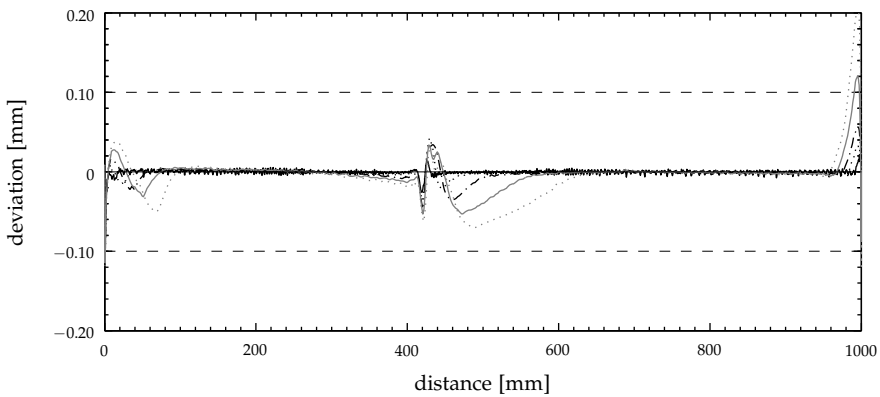
5.5.1 Straight line motion

The straight line motion experiment is repeated several times with an increase in path velocity each time. The simulated path errors in y -direction and z -direction are plotted as a function of the travelled distance in figure 5.10. The figure shows that the path tracking error increases with higher velocities. However, the maximum path tracking error stays mostly within the limits of ± 0.1 mm that are required by the laser welding process. Only at the velocities of 300 mm/s and beyond is there a small part along the trajectory of about 8 mm—starting at the velocity reversal of joints 2, 3 and 5—where the tracking error is above 0.1 mm.

The orientation of the welding head is less critical in the laser welding process and the orientation errors may be of the order of several degrees. The observed errors in the orientation are very small and therefore negligible. Additional simulation results can be found in Appendix C.1. Figures C.2 and C.3 show the simulated and measured path tracking accuracy at a welding velocity of 300 mm/s and 500 mm/s, respectively. At these high velocities, the simulated path tracking errors deviate from the measured path tracking errors. These deviations are caused by the fact that the Stäubli RX90B robot has flexible joints which are excited by the acceleration and deceleration phases and by the velocity reversal at about 400 mm. Figures C.4 and C.5 show that the measured and simulated joint torques match reasonably well. The mismatches, which can be observed as small offsets, are caused by differences in the viscous friction torques and are a result of variations in the joint temperature.



(a) Deviation in y-direction.



(b) Deviation in z-direction.

Figure 5.10: The simulated path tracking errors at different path velocities; — $v = 100$ mm/s, \cdots $v = 200$ mm/s, $-\cdot-$ $v = 300$ mm/s, $---$ $v = 400$ mm/s, \cdots $v = 500$ mm/s and $--$ denotes the maximum allowable tracking error.

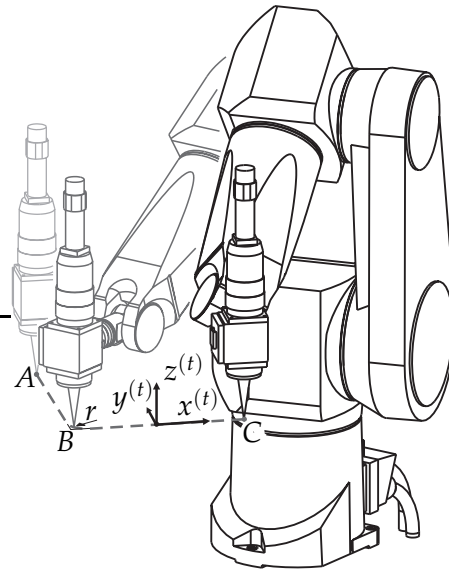


Figure 5.11: Motion experiment: the robot moves through a corner from A to B to C at a constant velocity with a smooth acceleration and deceleration profile while keeping the orientation of the laser welding head aligned with the coordinate system $(x^{(t)}, y^{(t)}, z^{(t)})$. The coordinate system is moving along the trajectory, with the x -axis constantly pointing in the direction of the motion. The corner has a radius r .

5.5.2 90° corner, the orientation of the welding head follows the orientation of the seam

The next experiment involves the motion along a trajectory that includes a 90° corner, while the laser welding head is following the orientation of the welding seam, as illustrated in figure 5.11. This is a typical situation when additional material is added to the weld by means of a wire feeding unit that has to remain in a fixed orientation with respect to the welding direction. The velocity profile is identical to the previous experiment. The corner has a radius $r = 100$ mm, which is achieved by applying a cubic spline interpolation between the start and the end of the curve. The cubic spline interpolation closely approximates a circle segment, while it ensures a smooth transition from the straight line part to the curved part of the trajectory and vice versa.

The joint angles, velocities and accelerations are computed using the inverse kinematic robot model. Figure C.7 in Appendix C.2 shows that the joint motion is quite complex, especially at the corner. All six joints incorporate two or more velocity reversals during the corner motion. The required joint accelerations are quite high which gives rise to large joint torques, see Appendix C.2, figure C.9.

Figures 5.12(a) and 5.12(b) show the simulated and measured path tracking accuracy. Note that even for a large radius of 100 mm the tracking error is already just above the threshold of 0.1 mm for some parts of the trajectory. The prediction of the simulation agrees quite well with the measurement on the robot, except for the part in between 320–370 mm. This is caused by the fact that the position errors of joints 5 and 6 are not predicted as accurately as the position errors of joints 1 to 4, see Appendix C.2, figure C.8.

In the next sequence, the corner radius is reduced while the tracking velocity is kept at 100 mm/s. The simulation shows that the path tracking error increases, as is to be expected. At the radius of $r = 50$ mm the joint position error of joint 4 reaches its maximum allowed value and an error is generated by the robot controller which results in an emergency stop of the robot's motion. In order to be able to perform the trajectory with smaller radii, the welding speed needs to be reduced. Reducing the velocity to 50 mm/s allows for a radius of 40 mm while the path tracking error peaks only just outside the limits, see figures 5.12(c) and 5.12(d).

Again, the prediction of the simulation agrees well with the measurement on the robot. The disagreement that is noted in the interval 320–370 mm is caused, once again, by the fact that the position errors of joints 5 and 6 were not predicted as accurately as the position errors of joints 1 to 4, see Appendix C.2, figure C.10. It is suspected that the self-locking properties of the worm-wheel gears and the load dependency of the asperity friction caused the mismatch. Figures C.10 and C.11 in Appendix C.2 show that there is a disagreement in the joint torques of joints 5 and 6 inside the robot wrist. For the first four joints, however, the joint torques are predicted quite accurately.

The experiments show that keeping the orientation of the laser welding head aligned with the trajectory imposes high demands on the robot. The minimum radius that can accurately be performed at 100 mm/s is about 100 mm. If smaller radii are required, the welding velocity needs to be reduced significantly.

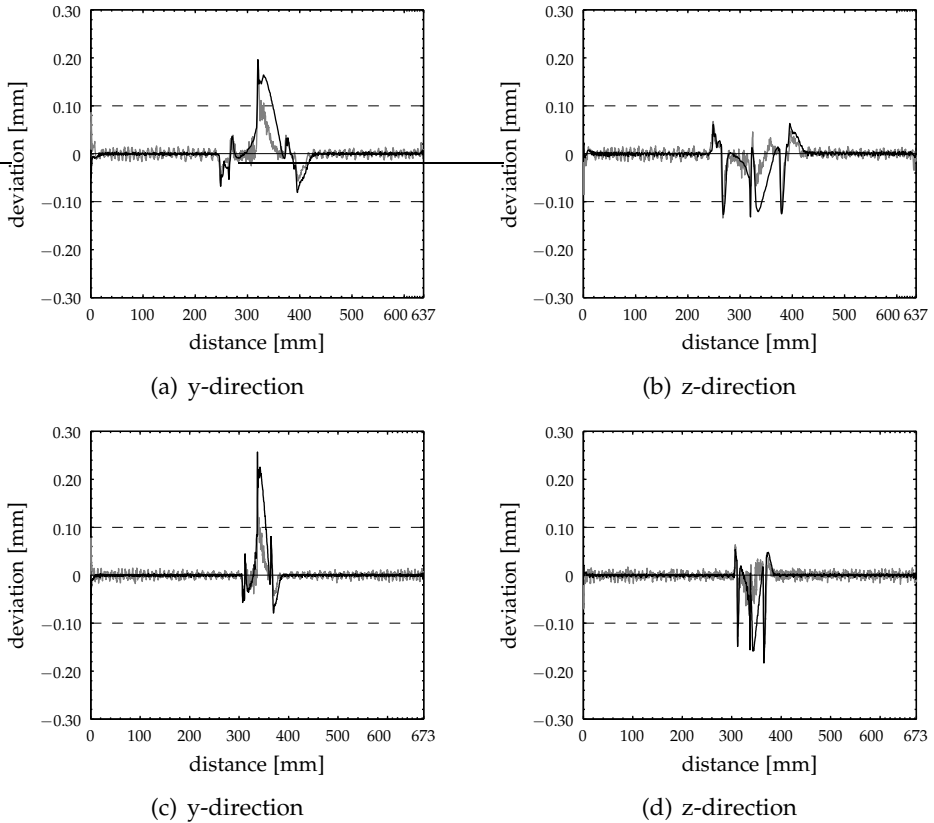


Figure 5.12: The simulated — and measured — path tracking errors of the laser welding head in y -direction and in z -direction during the 90° corner motion experiment where the welding head follows the orientation of the trajectory. In (a) and (b) the corner radius is 100 mm and the welding speed is 100 mm/s. In (c) and (d) the corner radius is 40 mm and the welding speed is 50 mm/s. The dashed line - - indicates the maximum allowable tracking error.

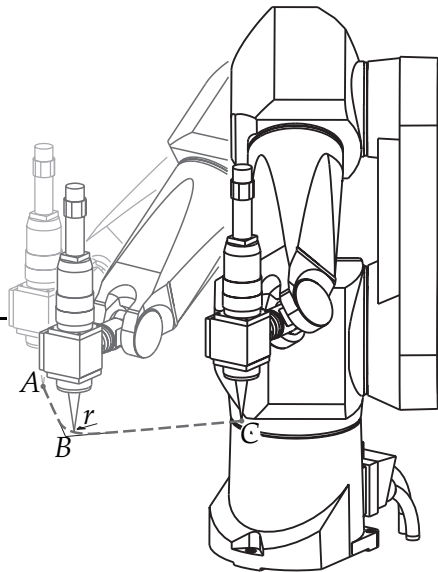


Figure 5.13: Motion experiment: the robot moves through a corner from A to B to C at a constant velocity with a smooth acceleration and deceleration profile while keeping a fixed orientation of the laser welding head with respect to the global coordinate system.

5.5.3 90° corner, fixed welding head orientation

In this experiment, the welding head orientation is fixed with respect to the robot base, as is illustrated in figure 5.13. The welding speed is kept constant at 100 mm/s while the radius of the corner r is reduced from 50 mm to 2.5 mm in several steps. The joint positions and the joint velocities for a radius of $r = 50$ mm are plotted as a function of time in figures C.13(a) and C.13(b), respectively. The figures show that there is a velocity reversal of joints 2, 3 and 5 at about $t = 3.9$ s. Note that the maximum velocity is one order lower than in figure C.7(b) in which the welding head orientation follows the orientation of the seam.

In figure 5.14 the path tracking errors along the trajectory in the y -direction and the z -direction, respectively, have been plotted. The figures clearly show that the tracking error stays well within the ± 0.1 mm tolerance for the major part of the trajectory. For all radii, there is a peak in the path tracking error in both directions when the robot moves through the

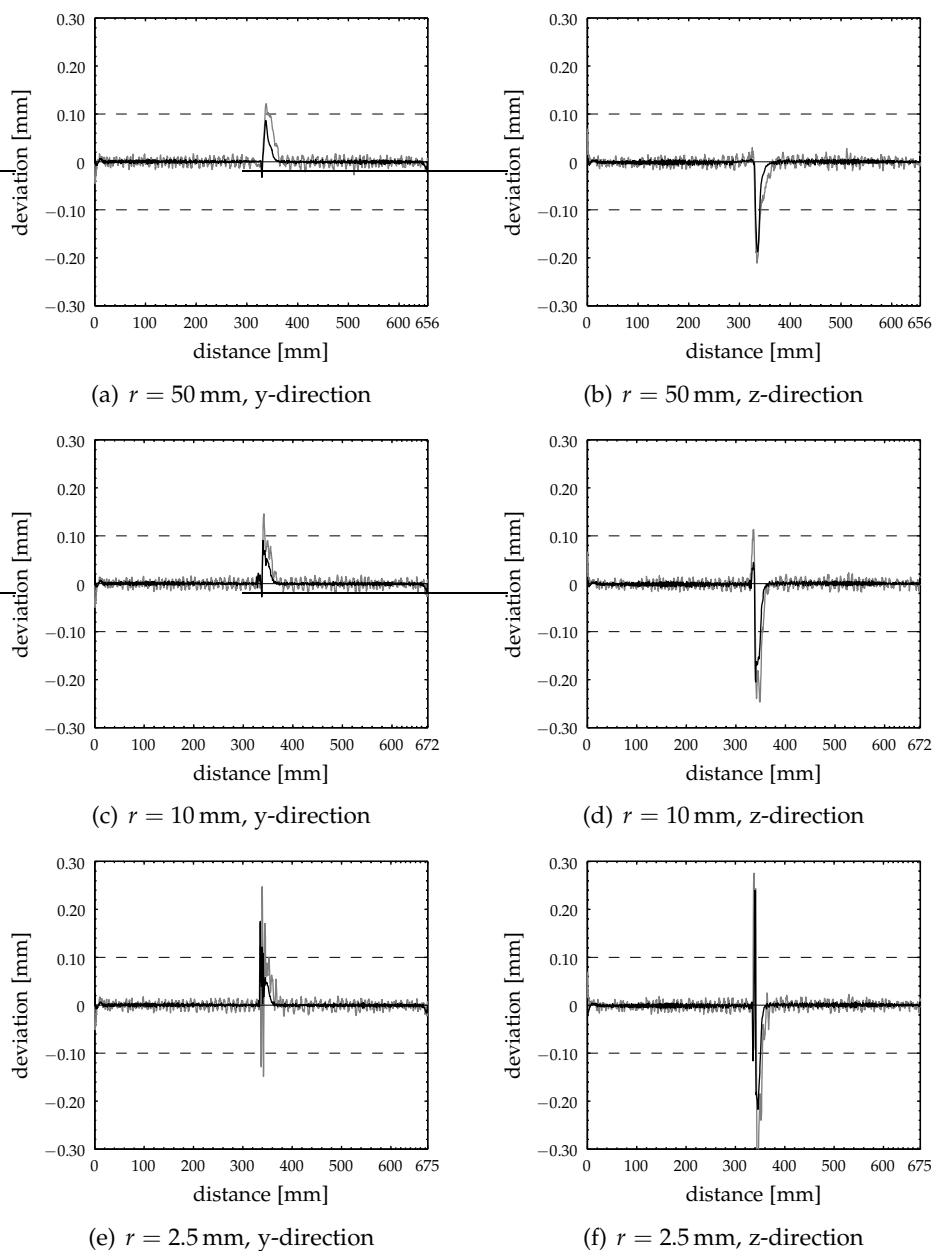


Figure 5.14: The simulated — and measured — path tracking error of the laser welding head during the 90° corner motion experiment at a welding speed of 100 mm/s. The dashed line - - indicates the maximum allowed tracking error.

corner. The error in y -direction does not significantly increase when the radius r is reduced and remains more or less within the limit of 0.1 mm. The tracking error in z -direction shows an increase from 0.2 mm to 0.3 mm when the radius is decreased from 50 mm to 2.5 mm. Although the tolerances of the laser welding process are a bit less strict for the z -direction (focus), the welding quality will be less in the corner for the 2.5 mm radius.

The simulation results agree well with the measurements. In Appendix C.3, in figures C.14 to C.15, the measured and simulated joint torques for the experiments with $r = 50$ mm, $r = 10$ mm, $r = 5$ mm and $r = 2.5$ mm are plotted and they demonstrate good agreement as well.

5.6 Discussion

In this chapter the closed-loop model of the Stäubli RX90B robot has been assembled. A perturbation method has been introduced in order to reduce the simulation time. Simulations of a straight line motion have been carried out to validate both the identified nonlinear robot model and the perturbation method.

The simulation results agree well with measurements that were carried out on the robot, leading to the conclusion that the robot model is adequate and that the model parameters have been identified consistently. However, at some parts of the trajectory somewhat larger differences between the simulation and the measurements occur.

The main disagreements that have been observed are caused by joint friction. First, due to different temperatures of the drives during the identification of the friction model parameters and during the motion experiments, the magnitude of the viscous friction torques may be different. This results in a difference between the magnitude of the simulated and measured joint torques. The impact of this difference on the tracking accuracy is negligible as the controller's integrating action is able to compensate for this low-frequency effect. Secondly, the pre-sliding joint friction model is not able to model the pre-sliding friction behaviour of the joints precisely. This model error manifests itself during velocity reversals of the joint, causing disagreements between the measured and simulated tracking errors. Furthermore, it causes differences between the simulated and measured joint torques during standstill. Additionally, the unmodelled load dependent friction behaviour of joints five and six leads

to differences between the simulated and measured joint torques. Finally, the self-locking nature of the worm wheel and gear is not included in the robot model, which means that static loads on the joints of the robot wrist are not transmitted to the servo motors.

The application of dynamic simulations in off-line programming has been demonstrated by means of three typical welding trajectories: the straight line motion, a 90° corner with the laser welding head following the orientation of the welding seam and a 90° corner with a constant orientation of the laser welding head. It was shown that it is possible to *a priori* detect path tracking errors on the basis of joint data which are caused by trajectories that are too demanding for the robot. Consequently, the simulations have demonstrated that the prediction of the path tracking errors is sufficiently accurate for use in off-line programming for robotised laser welding.

Chapter 6

Conclusions & Discussion

6.1 Conclusions

In this thesis, the dynamic modelling, identification and simulation of a Stäubli RX90B industrial robot for off-line programming of robotised laser welding has been presented. First, the modelling of the main components, the robot arm, the driving system including friction and the robot controller have been discussed in detail. The key in accurate dynamic simulations lies in the availability of a model structure with a set of dynamic equations that model the relevant physical phenomena of the actual robot correctly. Such a model structure is a prerequisite for consistent identification of the model parameters by performing experimental identification techniques. The robot model has been validated by means of several motion experiments. Finally, the applicability of dynamic simulations in off-line programming has been demonstrated for three typical welding jobs.

From the work presented in this thesis the following general conclusions can be drawn:

- Assuming an ideal transmission in which the friction torques of the gears and bearings inside a joint are lumped into a single joint friction torque is sufficient for application in a rigid model for the Stäubli RX90 robot.
- Phenomenological friction models, commonly used in control literature, are inadequate to model the viscous friction behaviour of the robot transmission for the full velocity range with sufficient

accuracy. A new joint friction model has been developed that relies on insights from sophisticated tribological models. The friction model accurately describes friction behaviour in the full velocity range with a minimal and physically sound parametrisation.

- A nonlinear six degree of freedom finite element model of the Stäubli RX90B industrial robot has been built. The application of the finite element model allows the model to be extended into a model that includes joint flexibility for future research. The presented parametrisation for the lumped mass description of the beam element allows for a robot model with equations of motion that are linear in the inertia parameters. Furthermore, the constitutive equation of the gravity compensating spring has been rewritten in a parameter linear form. The equations of motion have been extended with the friction models which were rewritten in such a way that they are linear in the temperature dependent parameters. Finally, the inertia properties of the servo motors were also added to the equations of motion in a parameter linear way.
- The linear least squares estimation technique is very suitable for the identification of the unknown model parameters. Analysis of the least squares problem by means of a singular value decomposition enables a careful selection of the number of parameters that can be estimated in the presence of measurement noise and unmodelled dynamics.
- A closed-loop model of the Stäubli RX90B robot has been assembled. A perturbation method has been introduced in order to reduce the simulation time. Simulations of straight line motion have been carried out to validate both the nonlinear robot model and the perturbation method. The simulation results have been shown to agree well with measurements that have been carried out on the robot. This leads to the conclusion that the model structure and the set of dynamic equations describe the relevant physical phenomena of the robot correctly and that the model parameters have been identified consistently.
- The main disagreements between measurements and simulations that have been observed are caused by joint friction. Three main causes can be indicated. First, due to temperature variations in the

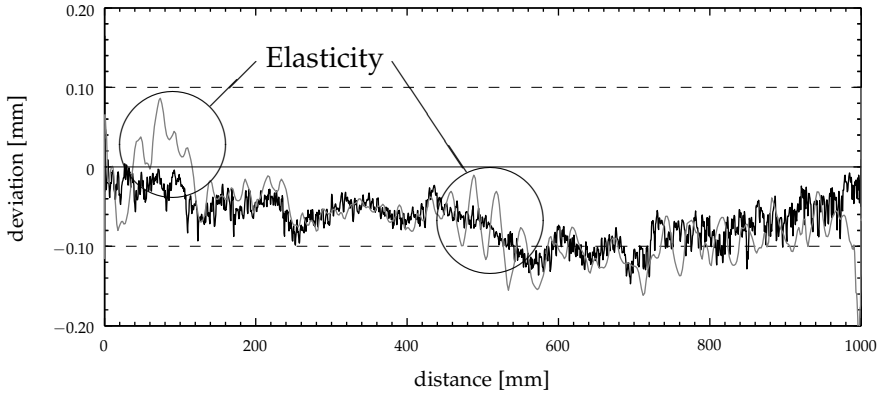
drives the magnitude of the viscous friction torques will vary. Secondly, the joint friction model is not equipped to describe the pre-sliding friction behaviour of the joints precisely. As a result, errors arise in the simulated joint positions during velocity reversals. Furthermore, this causes differences between the simulated and measured joint torques during standstill. Finally, the unmodelled load dependent and self-locking friction behaviour of joints five and six leads to differences between the simulated and measured torques for these joints.

- The simulations have shown that the prediction of the path tracking errors is sufficiently accurate for use in off-line programming for laser welding. The application of dynamic simulations in off-line programming has been demonstrated by means of three typical welding trajectories: the straight line motion, a 90° corner with the laser welding head following the orientation of the welding seam and a 90° corner with a constant orientation of the laser welding head. It has been shown that it is possible to *a priori* detect path tracking errors as a result of trajectories that are too demanding for the robot.

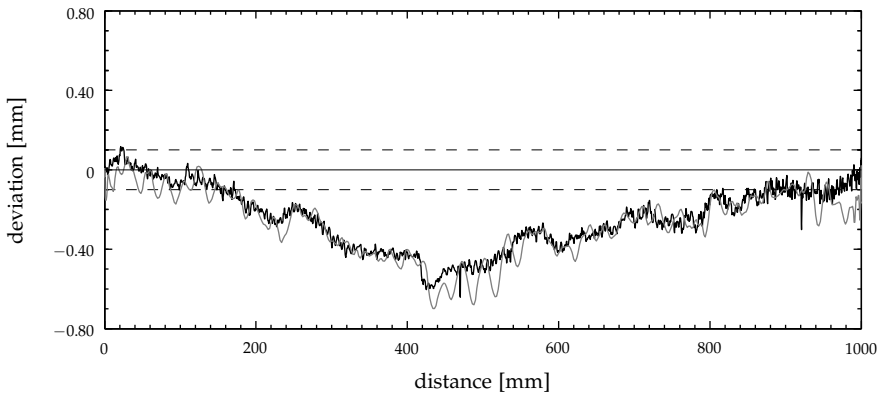
6.2 Discussion and suggestions for future research

Joint friction is the root cause for many difficulties that were encountered during the research presented in this thesis. In order to increase the accuracy of both the dynamic simulations and the parameter identification, further research on joint friction is recommended. In particular, the friction behaviour of the robot wrist and the worm wheel and gear will need more attention. Additionally, the pre-sliding behaviour during velocity reversals should be modelled more precisely.

The robot model presented in this thesis did not include drive nonlinearities and flexibilities. Furthermore, the path tracking performance of the robot was based on the joint motion of the robot with an ideal kinematic description. In reality, the path tracking accuracy of the robot is compromised by joint flexibilities, kinematic errors, drive nonlinearities and disturbance forces from the motion of the optical fibre and coolant/shielding gas hoses attached to the laser welding head. In figure 6.1, the actual path tracking errors that have been observed during the straight line experiment of section 5.4 are shown. The path tracking



(a) Deviation in y-direction.



(b) Deviation in z-direction.

Figure 6.1: The measured path tracking errors using a seam tracking sensor at two different velocities; — $v = 100$ mm/s and — $v = 500$ mm/s. The line - - denotes the maximum allowable tracking error.

errors were measured with a seam tracking sensor mounted at the robot tip. The figure shows the path tracking errors for two different velocities; $v = 100 \text{ mm/s}$ and $v = 500 \text{ mm/s}$.

The large and 'slow' path tracking errors are caused by kinematic deviations; the lengths of the links differ slightly from those used in the kinematic model in the robot controller. This is due to fabrication tolerances and, more importantly, to temperature variations. Furthermore, the gravitational load on the joint elasticity causes the robot arm to sag.

The more erratic path tracking errors are caused by drive nonlinearities; imperfections in the dimensions and shape of the drive components lead to non-constant gear ratios and, consequently, deviations in the kinematics. Either of these path tracking errors can be observed for both velocities. Joint elasticity is more excited at the welding velocity of 500 mm/s , which is clearly noticeable at the start of the trajectory and at the point of the velocity reversal of joints 2, 3 and 5, at about 420 mm .

The path measurement with the seam tracking sensor shows that extension of the robot model with drive nonlinearities and flexibilities is desirable. However, the main limitations of the robot are already predicted by the rigid robot model as presented in this thesis. Furthermore, several innovative techniques are being developed to compensate for remaining path tracking errors due to drive nonlinearities, kinematic errors and to some extent flexibilities also. Some promising techniques are, for instance:

- Application of seam tracking sensors and algorithms for robotised laser welding (De Graaf et al., 2006).
- Application of iterative learning control for robotised laser welding (Hakvoort et al., 2006).
- Application of scanning laser welding optics for robotised laser welding (Hardeman et al., 2006a).

In order to utilise dynamic robot simulations to support off-line programming software, it is recommended that the simulation software becomes available as a so-called plug-in in the OLP software. In this way the graphical user interface of the OLP software can be used to visualise the predicted path tracking accuracy directly on the graphical model of the weld seam.

Appendix A

Friction behaviour of a helical gear pair

The kinematics associated with helical gear are quite complex. In order to make a simplification, a two-dimensional analysis is made using a cross-section of two helical gears in contact, see figure A.1. The goal of the analysis is to derive expressions for both tangential velocities $u_1^{(t)}$ and $u_2^{(t)}$ as a functions of the angular velocity ω_1 of the driving gear wheel. The expressions are then used in the modelling of the friction torques arising in the helical gear pair.

Because of the fact that the gear teeth have an involute shape, the point of contact C travels along the contact line, from the start of the contact C_{in} to the end of the contact C_{out} . In order for the gear teeth to stay in contact along the contact line, the surface points of both gear teeth in the contact point C must have the same velocity, consequently

$$u^{(n)} = R_1^{(b)} \omega_1 = R_2^{(b)} \omega_2, \quad (\text{A.1})$$

where $R_1^{(b)}$ and $R_2^{(b)}$ are the base circle radii. The base circle radii are given by

$$R_1^{(b)} = R_1^{(p)} \cos(\alpha^{(p)}), \quad (\text{A.2a})$$

$$R_2^{(b)} = R_2^{(p)} \cos(\alpha^{(p)}), \quad (\text{A.2b})$$

where $R_1^{(p)}$ and $R_2^{(p)}$ are the pitch circles of the gear wheels and $\alpha^{(p)}$ is the

pressure angle. From equation (A.1) follows the gear ratio

$$\frac{\omega_1}{\omega_2} = \frac{R_2^{(b)}}{R_1^{(b)}} = \frac{z_2}{z_1} = n^{(g)}, \quad (\text{A.3})$$

where z_1 and z_2 denote the number of teeth for each gear wheel.

In the contact point C , the velocities u_1 and u_2 of the gear teeth are

$$u_1 = \omega_1 R_1^{(c)} = \omega_1 \frac{R_1^{(p)} \cos(\alpha^{(p)})}{\cos(\alpha^{(p)} + \beta_1)}, \quad (\text{A.4a})$$

$$u_2 = \omega_2 R_2^{(c)} = \omega_2 \frac{R_2^{(p)} \cos(\alpha^{(p)})}{\cos(\alpha^{(p)} + \beta_2)}. \quad (\text{A.4b})$$

Using the uniformity of the angles, the expressions for the tangential velocities $u_1^{(t)}$ and $u_2^{(t)}$ are expressed as

$$u_1^{(t)} = \sin(\alpha^{(p)} + \beta_1) u_1 = \omega_1 R_1^{(p)} \cos(\alpha^{(p)}) \tan(\alpha^{(p)} + \beta_1), \quad (\text{A.5a})$$

$$u_2^{(t)} = \sin(\alpha^{(p)} + \beta_2) u_2 = \omega_2 R_2^{(p)} \cos(\alpha^{(p)}) \tan(\alpha^{(p)} + \beta_2). \quad (\text{A.5b})$$

With the substitutions $\omega_2 R_2^{(p)} = \omega_1 R_1^{(p)}$ and $\beta_2 = -n^{(g)} \beta_1$, the expressions for the sum and sliding velocities become

$$u^{(+)} = \omega_1 R_1^{(p)} \cos(\alpha^{(p)}) \left(\tan(\alpha^{(p)} + \beta_1) + \tan(\alpha^{(p)} - n^{(g)} \beta_1) \right), \quad (\text{A.6a})$$

$$u^{(-)} = \omega_1 R_1^{(p)} \cos(\alpha^{(p)}) \left(\tan(\alpha^{(p)} + \beta_1) - \tan(\alpha^{(p)} - n^{(g)} \beta_1) \right). \quad (\text{A.6b})$$

For a typical pressure angle $\alpha^{(p)} = 20^\circ$ and a gear ratio $n^{(g)} \approx 0.3$, the sum and sliding velocities have been plotted as a function of the angle of rotation β_1 during the full interconnecting phase of a single tooth, see figure A.2. It is clear from equations (A.6) that the expressions are nonlinear functions of the angle of rotation β_1 . However, figure A.2 indicates that both the sum and sliding velocity might be approximated by functions that are linear in β_1 .

A first order Taylor series expansion in β_1 of both velocities yields

$$u^{(+)} = 2\omega_1 R_1^{(p)} \sin(\alpha^{(p)}) + \omega_1 R_1^{(p)} \beta_1 \frac{1 - n^{(g)}}{\cos(\alpha^{(p)})} + \mathcal{O}(\beta_1^2), \quad (\text{A.7a})$$

$$u^{(-)} = 0 + \omega_1 R_1^{(p)} \beta_1 \frac{1 + n^{(g)}}{\cos(\alpha^{(p)})} + \mathcal{O}(\beta_1^2). \quad (\text{A.7b})$$

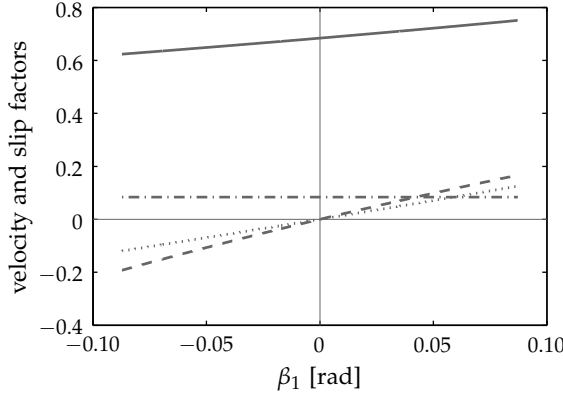


Figure A.2: The sum (—) and sliding (·····) velocity factors, the slip factor (---) and the average absolute slip factor (- · - ·) as a function of β_1 . Multiplication of the sum and sliding velocity factors with $\omega_1 R_1^{(p)}$ yields the actual velocities.

The sum velocity $u^{(+)}$ is taken invariant for β_1 and is approximated by its zeroth order Taylor expansion

$$u^{(+)} \approx 2\omega_1 R_1^{(p)} \sin(\alpha^{(p)}), \quad (\text{A.8})$$

which leads to an error of $\pm 10\%$ on the sum velocity along the interconnection phase for the gear ratio $n^{(g)} \approx 0.3$ at hand. The sliding velocity is approximated by its first order Taylor expansion, yielding

$$u^{(-)} \approx \omega_1 R_1^{(p)} \beta_1 \frac{1 + n^{(g)}}{\cos(\alpha^{(p)})}. \quad (\text{A.9})$$

The first order Taylor approximation of the slip ratio s is

$$s \approx \frac{\beta_1 (1 + n^{(g)})}{2 \sin(\alpha^{(p)}) \cos(\alpha^{(p)})}. \quad (\text{A.10})$$

Because the friction force is a dissipative force and the sliding velocity is approximated as a linear function of the contact angle β_1 , an average and positive slip ratio s_0 is considered for the full meshing phase of the gear teeth. The average slip ratio is computed by taking the mean of the

absolute value of β_1 . This then leads to the average absolute slip ratio s_0 , given by

$$s_0 = \frac{\beta_1^{(c)}(1 + n^{(g)})}{4 \sin(\alpha^{(p)}) \cos(\alpha^{(p)})}, \quad (\text{A.11})$$

where $\beta_1^{(c)}$ denotes the maximum contact angle during the meshing phase and $\alpha^{(p)}$ the pressure angle of the gear pair.

The friction force $f^{(f)}$ that is generated in the contact contributes to a friction torque $\mathcal{T}^{(f)}$ which is computed as

$$\mathcal{T}^{(f)} = R_1^{(b)} f^{(f)}. \quad (\text{A.12})$$

Appendix B

Spatial finite elements

B.1 Spatial slider truss element

The position of the element is determined by two Cartesian position vectors \mathbf{x}^p and \mathbf{x}^q of the end nodes p and q , respectively, see figure B.1. The vector of nodal coordinates for the truss element is then

$$\mathbf{x}^{(k)} = \begin{bmatrix} \mathbf{x}^p \\ \mathbf{x}^q \end{bmatrix} = [x^p \quad y^p \quad z^p \mid x^q \quad y^q \quad z^q]^T. \quad (\text{B.1})$$

The number of rigid body degrees of freedom is five, as a rotation around the p - q axis is not involved in the description of the element position. With the six nodal coordinates, this leaves a single deformation mode for the element. Naturally, the deformation mode is defined as the element's elongation and is expressed as a function of the instantaneous values of the position coordinates \mathbf{x}^q and \mathbf{x}^p and the reference length. The

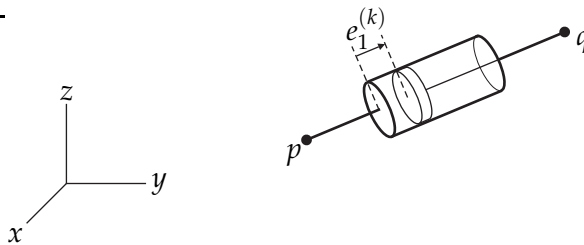


Figure B.1: The spatial slider truss element in a deformed state.

deformation function is defined by

$$e_1^{(k)} = \mathcal{D}_1^{(k)}(\mathbf{x}^{(k)}) = l^{(k)} - l_0^{(k)}, \quad (\text{B.2})$$

where $l_0^{(k)}$ is the reference length of the element and $l^{(k)}$ is defined as

$$l^{(k)} = \sqrt{(\mathbf{x}^q - \mathbf{x}^p)^T (\mathbf{x}^q - \mathbf{x}^p)}, \quad (\text{B.3})$$

which is the actual length of the element.

B.2 Lambda element

Although the λ -element is not a real structural element, the way in which it is used in the theory justifies its presentation as an element. According to Euler, an arbitrary rotation can always be described as a rotation along a certain axis \mathbf{n}_ϕ over a certain angle ϕ . The set of Euler parameters that describes this rotation forms the unit quaternion

$$\boldsymbol{\lambda} = \begin{bmatrix} \lambda_0 \\ \boldsymbol{\lambda}_\phi \end{bmatrix}, \quad (\text{B.4})$$

which is defined as:

$$\lambda_0 = \cos\left(\frac{\phi}{2}\right), \quad (\text{B.5a})$$

$$\boldsymbol{\lambda}_\phi = \begin{bmatrix} \lambda_1 \\ \lambda_2 \\ \lambda_3 \end{bmatrix} = \mathbf{n}_\phi \sin\left(\frac{\phi}{2}\right). \quad (\text{B.5b})$$

Rotations described in terms of Euler parameters must satisfy the constraint equation

$$\lambda_0^2 + \lambda_1^2 + \lambda_2^2 + \lambda_3^2 = 1 \quad \text{or} \quad \boldsymbol{\lambda}^T \boldsymbol{\lambda} = 1. \quad (\text{B.6})$$

Let the deformation function for the λ -element be defined as

$$e^{(\lambda)} = \mathcal{D}^{(k)} = \boldsymbol{\lambda}^T \boldsymbol{\lambda} - 1. \quad (\text{B.7})$$

In that case the constraint condition for the Euler parameters is of a similar form as the un-deformability condition $e^{(\lambda)} = 0$ for the λ -element. For each set of Euler parameters used in the description, a λ -element is added to the list of elements with the condition that the deformation mode belonging to the λ -element is prescribed a value of zero.

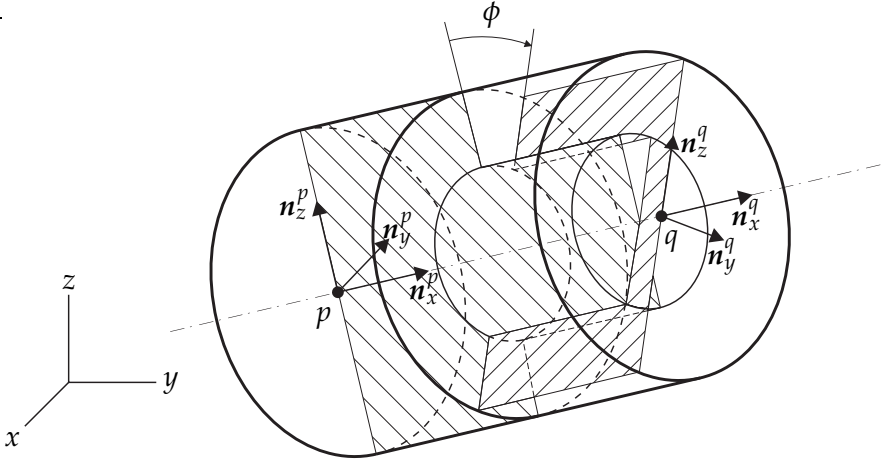


Figure B.2: Graphical representation of the spatial hinge element. The figure shows a rotation ϕ around the main axis of the element.

B.3 Spatial hinge element

The spatial hinge element, illustrated in figure B.2, describes the relative rotation between nodes p and q . The hinge element has been introduced by Van der Werff and Jonker (1984). Later, Geradin et al. (1986) presented the expressions for the deformations in their present form.

Using the Euler parameters, the vector of nodal coordinates for the hinge element is expressed as

$$\mathbf{x}^{(k)} = \begin{bmatrix} \boldsymbol{\lambda}^p \\ \boldsymbol{\lambda}^q \end{bmatrix} = [\lambda_0^p \ \lambda_1^p \ \lambda_2^p \ \lambda_3^p \mid \lambda_0^q \ \lambda_1^q \ \lambda_2^q \ \lambda_3^q]^T. \quad (\text{B.8})$$

The configuration of the hinge element is then given by the two sets of Euler parameters $\boldsymbol{\lambda}^p$ and $\boldsymbol{\lambda}^q$ describing the orientation of the orthogonal triads $(\mathbf{n}_x^p, \mathbf{n}_y^p, \mathbf{n}_z^p)$ and $(\mathbf{n}_x^q, \mathbf{n}_y^q, \mathbf{n}_z^q)$ rigidly attached to nodes p and q . Note that nodes p and q coincide and that their initial orientation is identical.

The relative rotation of the triad $(\mathbf{n}_x^q, \mathbf{n}_y^q, \mathbf{n}_z^q)$ rigidly attached to node q with respect to the triad $(\mathbf{n}_x^p, \mathbf{n}_y^p, \mathbf{n}_z^p)$ rigidly attached to node p is described by the set of Euler parameters $\boldsymbol{\lambda}^r$ which is obtained from the quaternion product (Geradin et al., 1986)

$$\boldsymbol{\lambda}^p \circ \boldsymbol{\lambda}^r = \boldsymbol{\lambda}^q, \quad (\text{B.9})$$

where

$$\boldsymbol{\lambda}^p \circ \boldsymbol{\lambda}^r = (\lambda_0^p \lambda_0^r - \boldsymbol{\lambda}_\phi^p \cdot \boldsymbol{\lambda}_\phi^r, \lambda_0^p \boldsymbol{\lambda}_\phi^r + \lambda_0^r \boldsymbol{\lambda}_\phi^p + \boldsymbol{\lambda}_\phi^p \times \boldsymbol{\lambda}_\phi^r). \quad (\text{B.10})$$

Multiplying both sides of equation (B.9) with the adjoint quaternion $\bar{\boldsymbol{\lambda}}^p$, which is defined as

$$\bar{\boldsymbol{\lambda}}^p = \begin{bmatrix} \lambda_0^p \\ -\boldsymbol{\lambda}_\phi^p \end{bmatrix}, \quad (\text{B.11})$$

yields the expression for the relative rotation r of node q with respect to node p

$$\boldsymbol{\lambda}^r = \bar{\boldsymbol{\lambda}}^p \circ \boldsymbol{\lambda}^q. \quad (\text{B.12})$$

This is a relative rotation expressed in the global reference frame. Usually, the initial orientation of the hinge is according to the local reference frame $(\boldsymbol{n}_x^p, \boldsymbol{n}_y^p, \boldsymbol{n}_z^p)$. Expressing the relative rotation $\boldsymbol{\lambda}^r$ in this local reference frame yields

$$\boldsymbol{\lambda}^{r'} = (\lambda_0^r, \boldsymbol{\lambda}_\phi^r \cdot \boldsymbol{n}_x^p, \boldsymbol{\lambda}_\phi^r \cdot \boldsymbol{n}_y^p, \boldsymbol{\lambda}_\phi^r \cdot \boldsymbol{n}_z^p). \quad (\text{B.13})$$

The hinge element has a total of eight nodal coordinates. The number of degrees of freedom of the element as a rigid body is three and with two constraint deformation modes for the Euler parameters (equation (B.7)) this leaves a total of three deformation modes. The deformation modes of the hinge element are expressed as

$$\text{relative rotation: } e_1^{(k)} = \mathcal{D}_1^{(k)}(\boldsymbol{x}^{(k)}) = 2 \arctan \left(\frac{\lambda_1^r}{\lambda_0^r} \right), \quad (\text{B.14a})$$

$$\text{bending: } \varepsilon_2^{(k)} = \mathcal{D}_2^{(k)}(\boldsymbol{x}^{(k)}) = 2(\lambda_0^r \lambda_2^r - \lambda_1^r \lambda_3^r), \quad (\text{B.14b})$$

$$\varepsilon_3^{(k)} = \mathcal{D}_3^{(k)}(\boldsymbol{x}^{(k)}) = 2(\lambda_1^r \lambda_2^r + \lambda_0^r \lambda_3^r), \quad (\text{B.14c})$$

where $e_1^{(k)}$ refers to large relative rotations around the main axis and $\varepsilon_2^{(k)}$ and $\varepsilon_3^{(k)}$ to the bending deformations.

B.4 Spatial beam element

Figure B.3 shows a spatial beam element in an x - y - z inertial coordinate system. The configuration of the beam element is determined by the

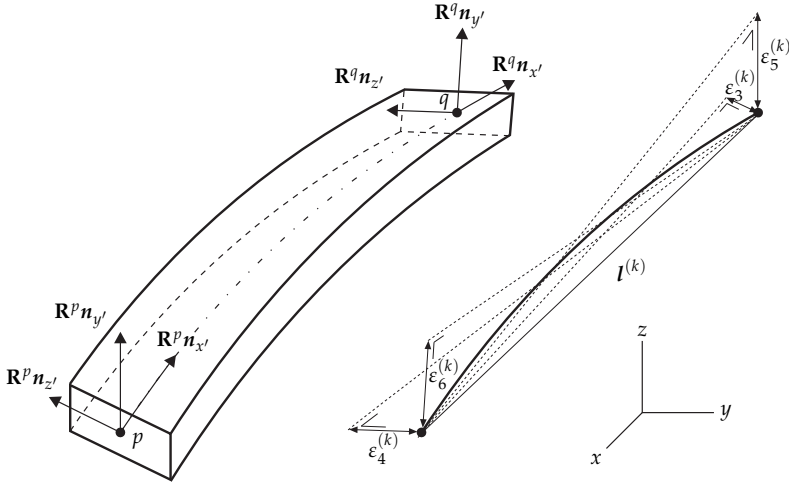


Figure B.3: The spatial beam element in a deformed state.

position vectors \mathbf{x}^p and \mathbf{x}^q of the end nodes and the angular orientation of the triads $(\mathbf{R}^p \mathbf{n}_{x'}, \mathbf{R}^p \mathbf{n}_{y'}, \mathbf{R}^p \mathbf{n}_{z'})$ and $(\mathbf{R}^q \mathbf{n}_{x'}, \mathbf{R}^q \mathbf{n}_{y'}, \mathbf{R}^q \mathbf{n}_{z'})$ rigidly attached to the end nodes. In the undeformed state, the triads coincide with the axis p - q and the principle axes of its cross section.

The nodal coordinates for the beam element are the two sets of Cartesian coordinates \mathbf{x}^p and \mathbf{x}^q and two sets of Euler parameters λ^p and λ^q at the nodes p and q . Consequently, the vector of nodal coordinates for the beam element is written as

$$\mathbf{x}^{(k)} = [x^p \ y^p \ z^p \ \lambda_0^p \ \lambda_1^p \ \lambda_2^p \ \lambda_3^p \ x^q \ y^q \ z^q \ \lambda_0^q \ \lambda_1^q \ \lambda_2^q \ \lambda_3^q]^T. \quad (\text{B.15})$$

The beam element has a total of fourteen nodal coordinates. The number of degrees of freedom of the element as a rigid body is six. With two constraint deformation modes for the Euler parameters (equation (B.7)), this leaves a total of six deformation modes. The deformation modes are defined as (Jonker, 2002):

$$\text{elongation: } \varepsilon_1^{(k)} = \mathcal{D}_1^{(k)}(\mathbf{x}^{(k)}) = \|\mathbf{l}^{(k)}\| - l_0^{(k)}, \quad (\text{B.16a})$$

$$\begin{aligned} \text{torsion: } \varepsilon_2^{(k)} &= \mathcal{D}_2^{(k)}(\mathbf{x}^{(k)}) \\ &= \frac{1}{2} l_0^{(k)} [(\mathbf{R}^p \mathbf{n}_{z'}, \mathbf{R}^q \mathbf{n}_{z'}) - (\mathbf{R}^p \mathbf{n}_{y'}, \mathbf{R}^q \mathbf{n}_{y'})], \end{aligned} \quad (\text{B.16b})$$

$$\text{bending: } \varepsilon_3^{(k)} = \mathcal{D}_3^{(k)}(\mathbf{x}^{(k)}) = - \left(\mathbf{R}^p \mathbf{n}_{z'}, \mathbf{l}^{(k)} \right), \quad (\text{B.16c})$$

$$\varepsilon_4^{(k)} = \mathcal{D}_4^{(k)}(\mathbf{x}^{(k)}) = \left(\mathbf{R}^q \mathbf{n}_{z'}, \mathbf{l}^{(k)} \right), \quad (\text{B.16d})$$

$$\varepsilon_5^{(k)} = \mathcal{D}_5^{(k)}(\mathbf{x}^{(k)}) = \left(\mathbf{R}^p \mathbf{n}_{y'}, \mathbf{l}^{(k)} \right), \quad (\text{B.16e})$$

$$\varepsilon_6^{(k)} = \mathcal{D}_6^{(k)}(\mathbf{x}^{(k)}) = - \left(\mathbf{R}^q \mathbf{n}_{y'}, \mathbf{l}^{(k)} \right), \quad (\text{B.16f})$$

where $l_0^{(k)}$ is the reference length of the element and the vector $\mathbf{l}^{(k)}$ is defined by

$$\mathbf{l}^{(k)} = \mathbf{x}^q - \mathbf{x}^p. \quad (\text{B.17})$$

The operator (\mathbf{a}, \mathbf{b}) denotes the inner product of vectors \mathbf{a} and \mathbf{b} . The first deformation mode represents the element's elongation. The second deformation mode represents the torsion of the element. The third to sixth deformation modes are associated with the bending of the element.

Appendix C

Simulation results

C.1 Straight line motion

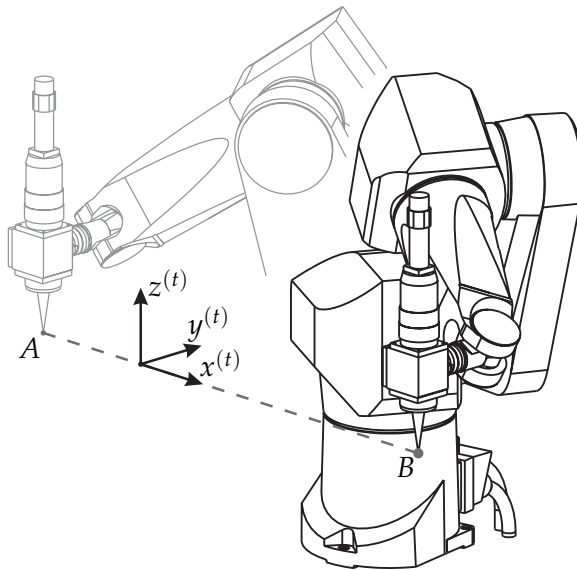
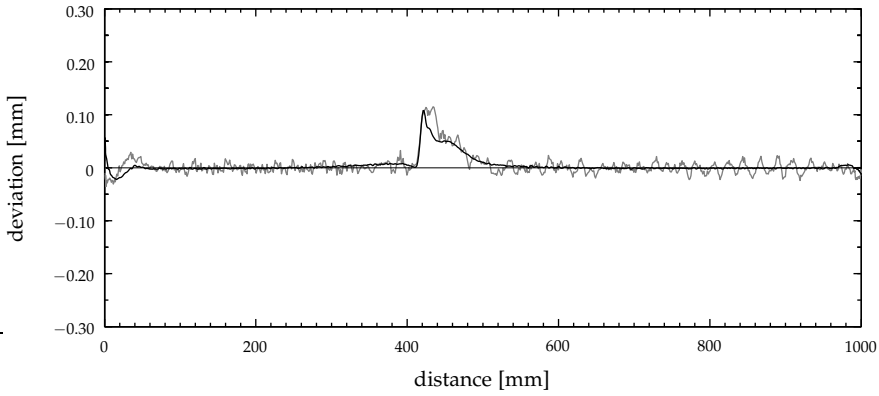
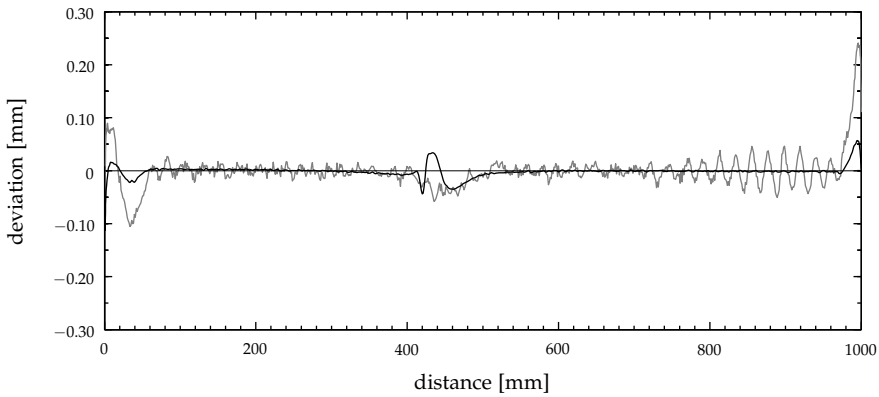


Figure C.1: Motion experiment: the robot tip (the focal point of the laser beam) moves along a straight line from A to B at a constant velocity while keeping the orientation of the laser welding head aligned with the coordinate system $(x^{(t)}, y^{(t)}, z^{(t)})$ of the trajectory.

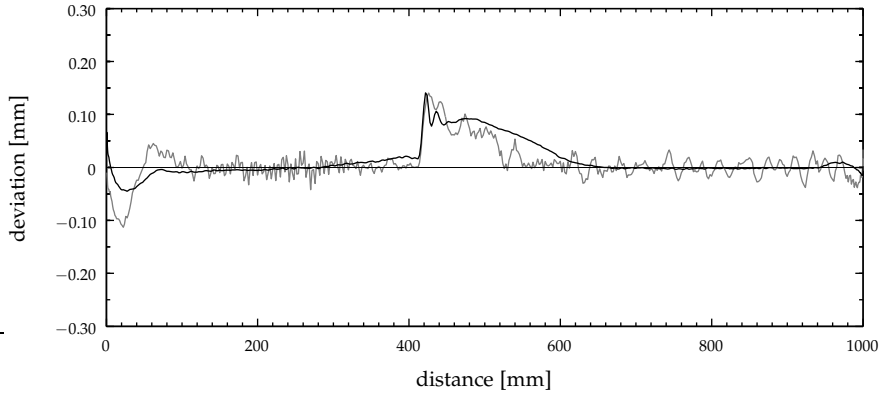


(a) Deviation in y-direction at 300 mm/s.

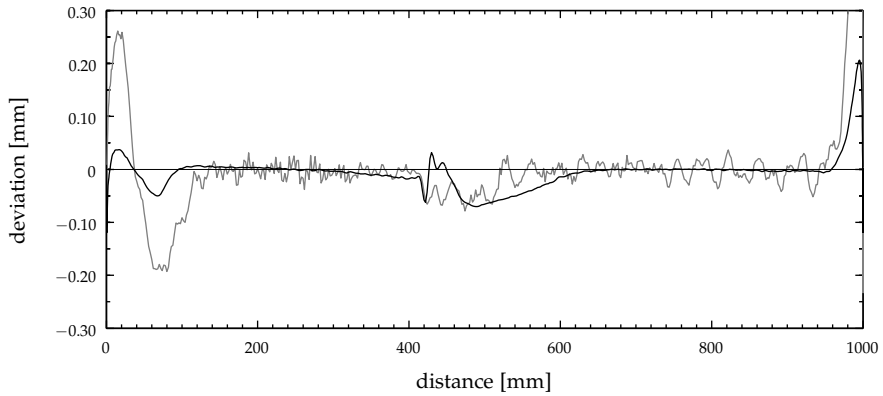


(b) Deviation in z-direction at 300 mm/s.

Figure C.2: The simulated — and measured — path tracking errors of the laser welding head in the straight line motion experiment at 300 mm/s.



(a) Deviation in y-direction at 500 mm/s.



(b) Deviation in z-direction at 500 mm/s.

Figure C.3: The simulated — and measured — path tracking errors of the laser welding head in the straight line motion experiment at 500 mm/s. At these high velocities, the simulated path tracking errors at the start and end of the trajectory deviate somewhat from the measured ones. These are caused by unmodelled behaviour, such as drive nonlinearities and flexibilities that are excited by the acceleration and deceleration phases.

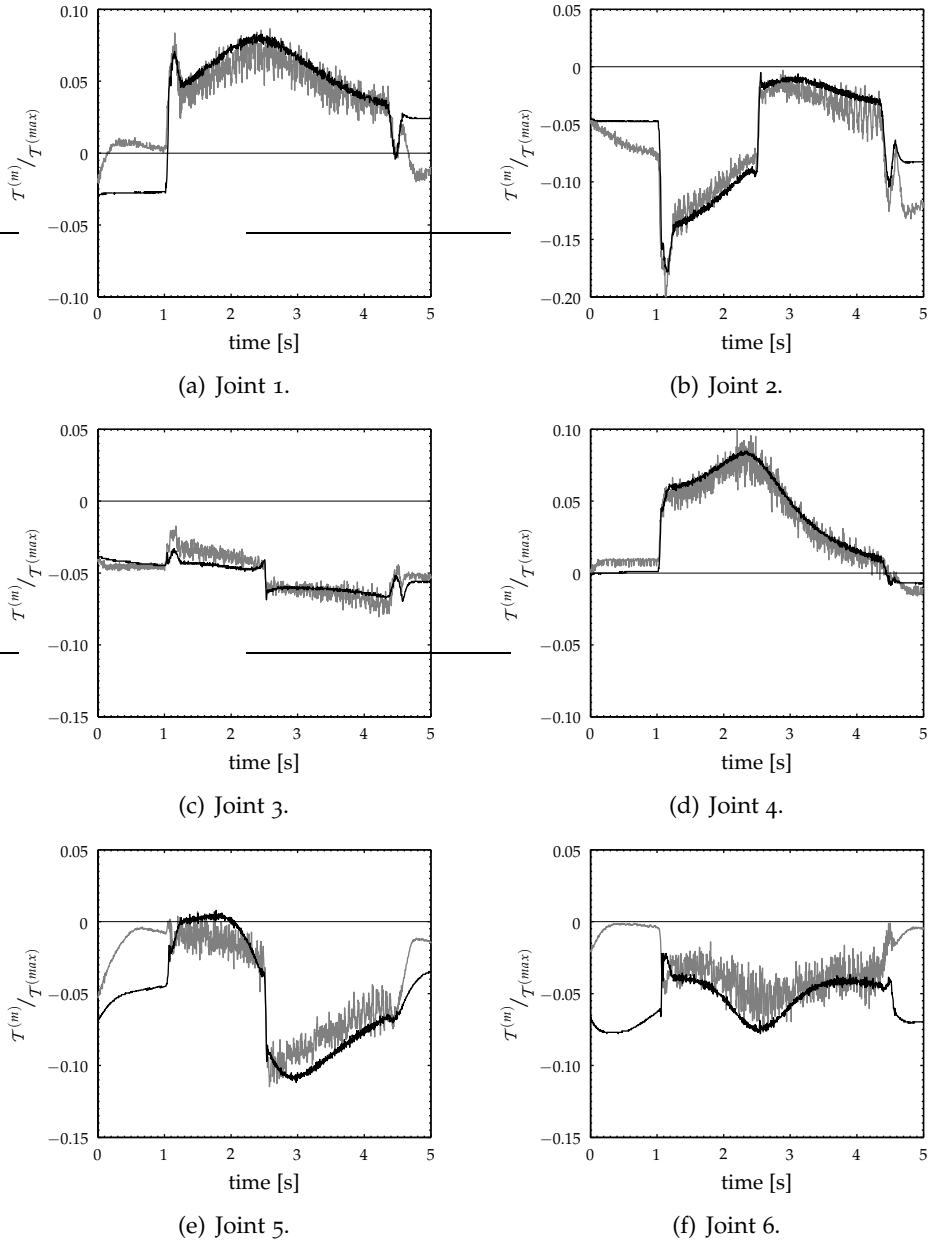


Figure C.4: The simulated — and measured — joint torques along the straight line trajectory at 300 mm/s as a function of time.

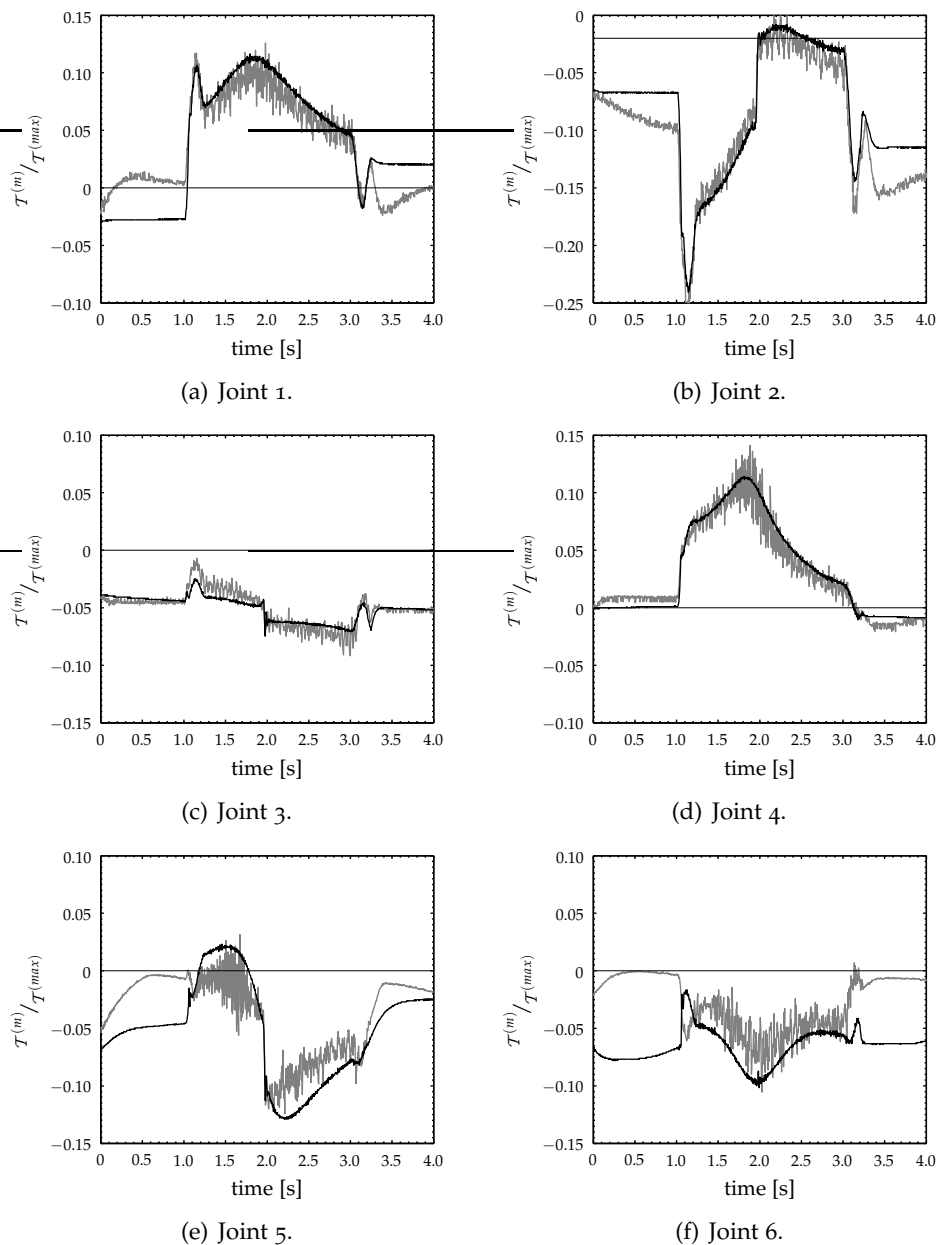


Figure C.5: The simulated — and measured — joint torques along the straight line trajectory at 500 mm/s as a function of time.

C.2 90° corner, welding head orientation follows the seam

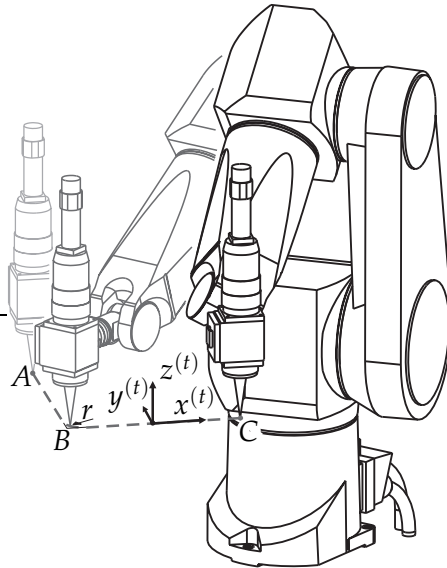
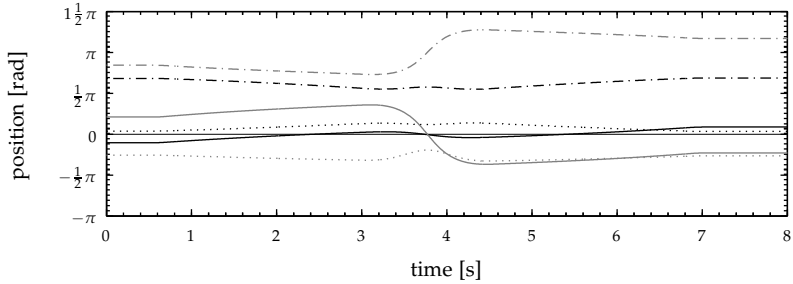
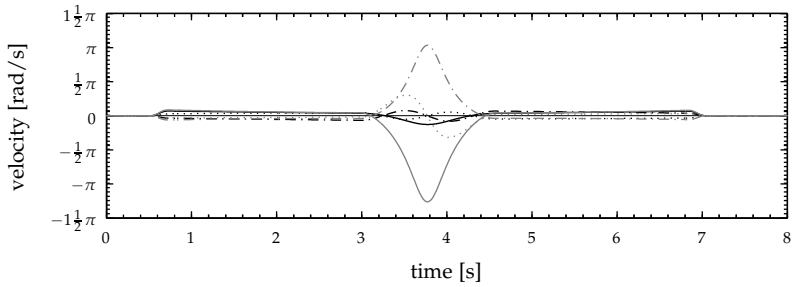


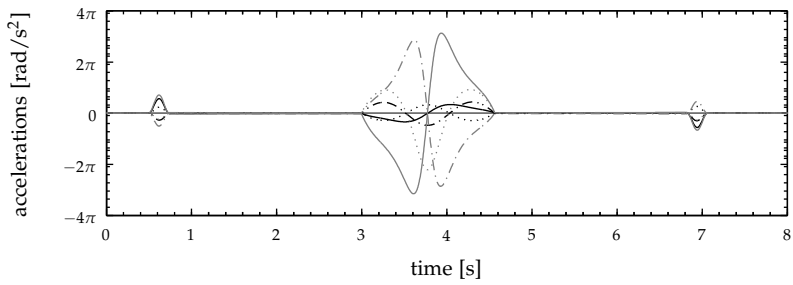
Figure C.6: Motion experiment: the robot moves through a corner from A to B to C at a constant velocity with a smooth acceleration and deceleration profile while keeping the orientation of the laser welding head aligned with the coordinate system $(x^{(t)}, y^{(t)}, z^{(t)})$ of the trajectory. The corner has a radius r .



(a) Joint angles.



(b) Joint angle velocities.



(c) Joint angle accelerations.

Figure C.7: Joint angles and velocity as a function of time in the corner motion experiment with a welding speed of 100 mm/s and a radius $r = 100$ mm. Note that all joints now have velocity reversals. The six joints are denoted by — q_1 , q_2 , - - - q_3 , — — — q_4 , - · - · - q_5 , - - - q_6 .

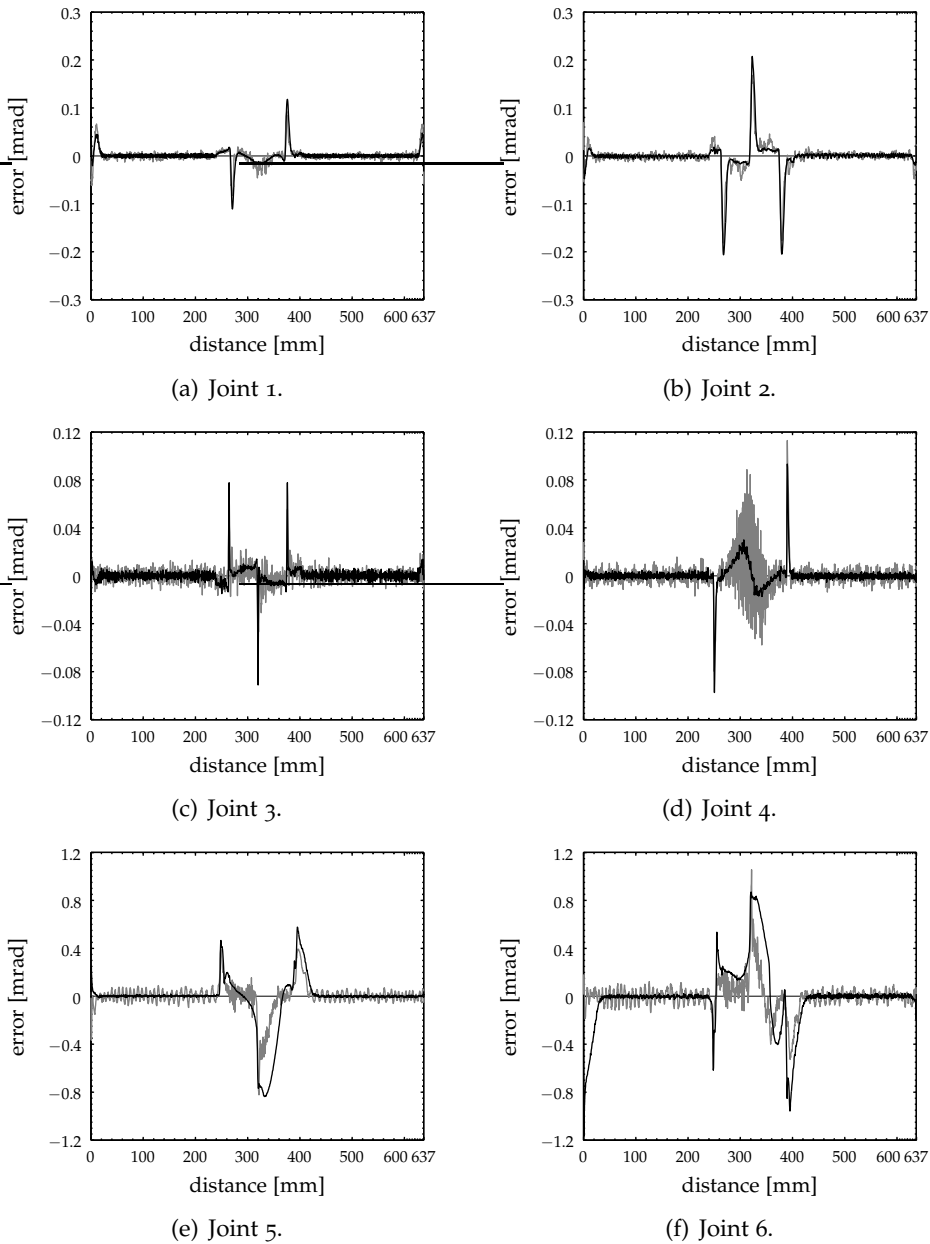


Figure C.8: The simulated — and measured — joint angular position errors along the corner trajectory at 100 mm/s with $r = 100$ mm as a function of the travelled distance along the trajectory.

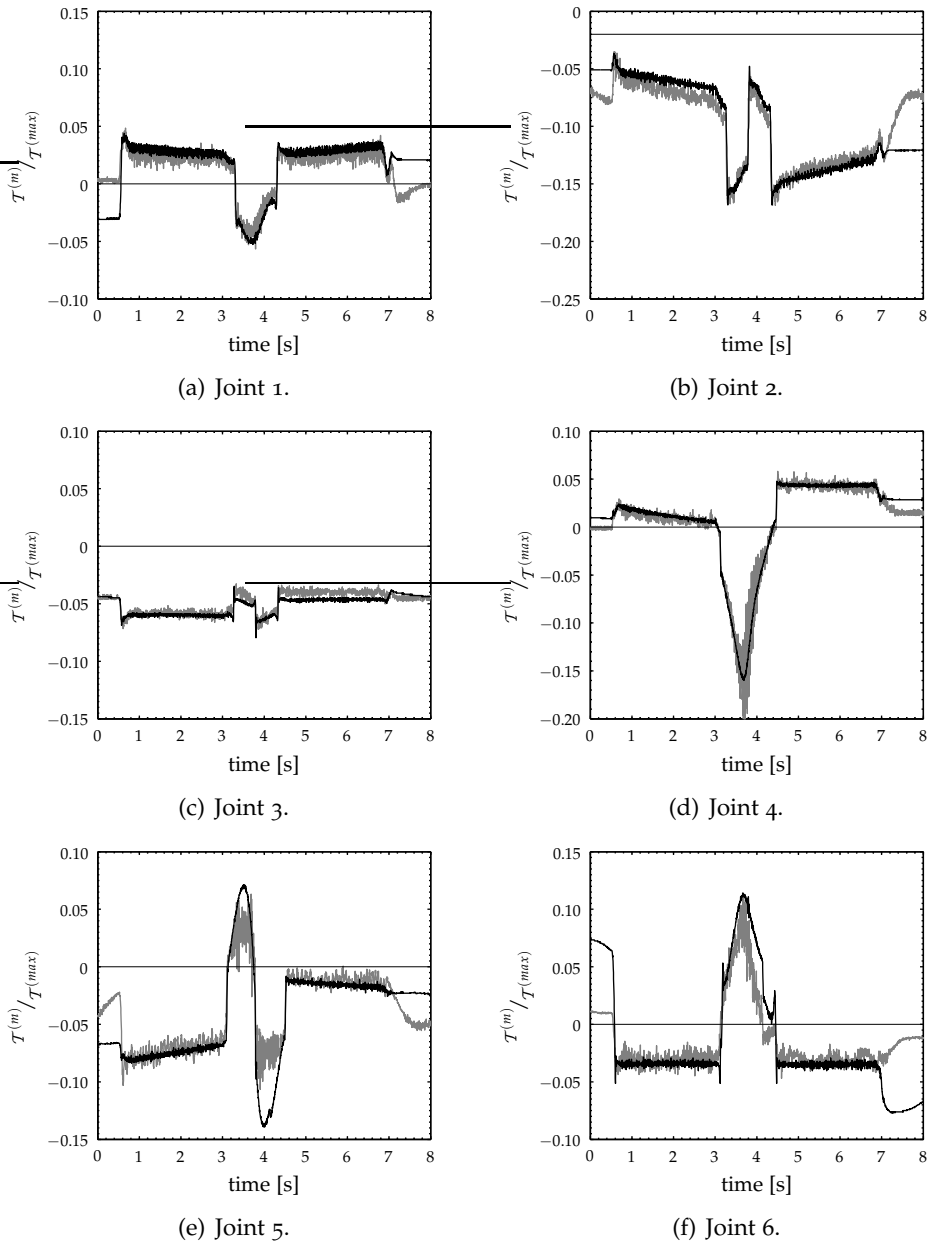


Figure C.9: The simulated — and measured — joint torques along the corner trajectory at 100 mm/s with $r = 100$ mm as a function of time.

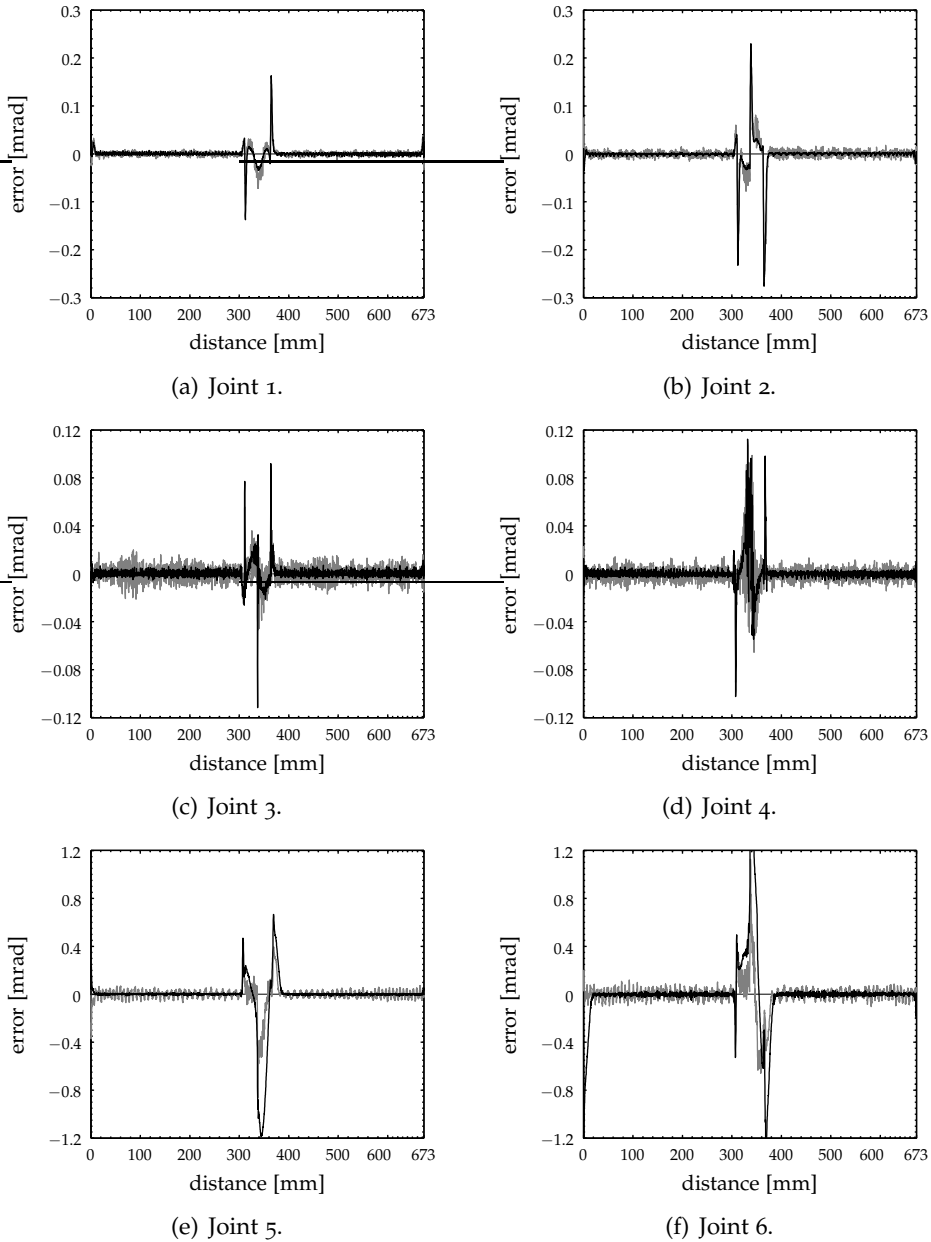


Figure C.10: The simulated — and measured — joint angular position errors along the corner trajectory at 50 mm/s with $r = 40$ mm as a function of the travelled distance along the trajectory.

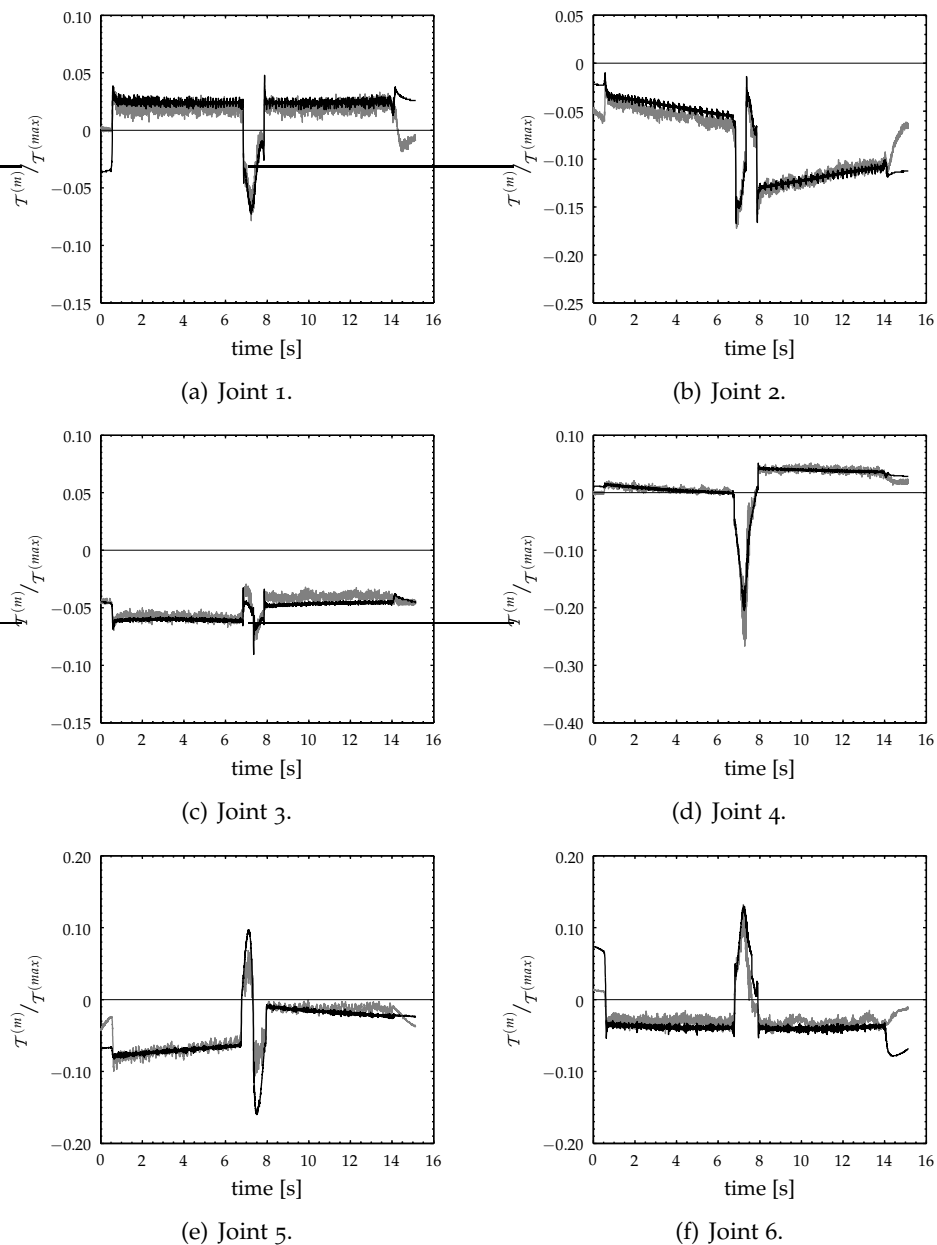


Figure C.11: The simulated — and measured — joint torques along the corner trajectory at 50 mm/s with $r = 40$ mm as a function of time.

C.3 90° corner, constant welding head orientation

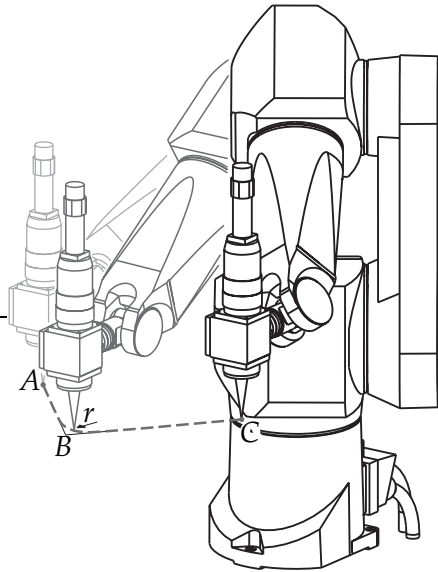
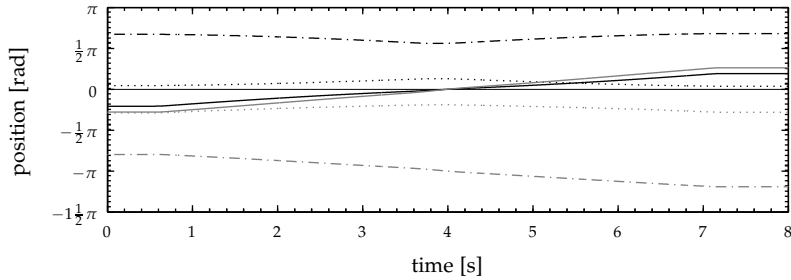
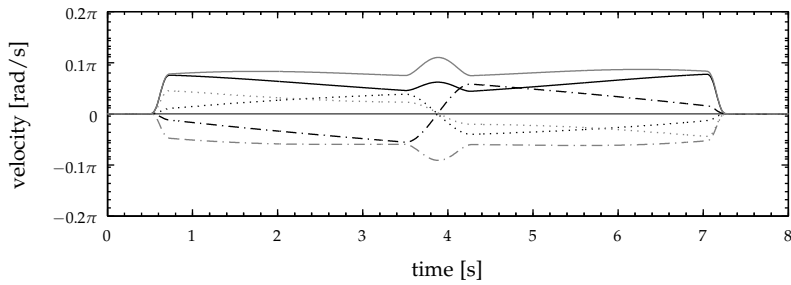


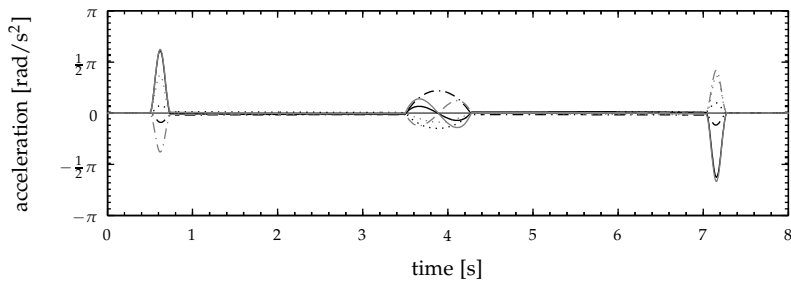
Figure C.12: Motion experiment: the robot moves through a corner from A to B to C at a constant velocity with a smooth acceleration and deceleration profile while keeping a fixed orientation of the laser welding head with respect to the global coordinate system. The corner has a radius r .



(a) Joint angles.

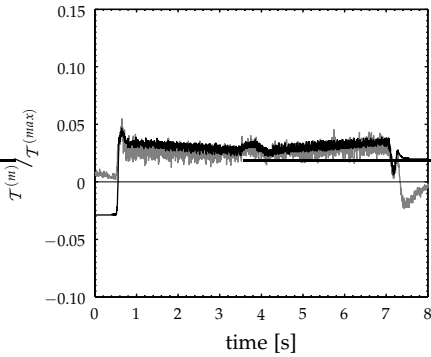


(b) Joint angle velocities.

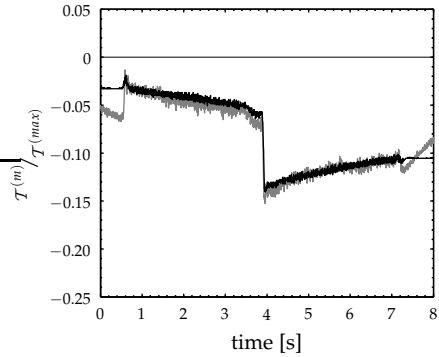


(c) Joint angle accelerations.

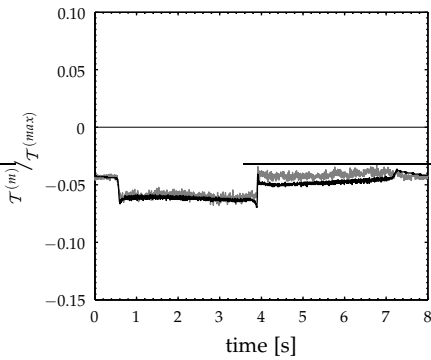
Figure C.13: Joint angles and velocity as a function of time in the corner motion experiment. The corner radius is 50 mm and the welding speed is 100 mm/s. Note that joints 2, 3 and 5 have a velocity reversal at about 3.9s. The six joints are denoted by — q_1 , q_2 , -.- q_3 , — q_4 , q_5 , -.- q_6 .



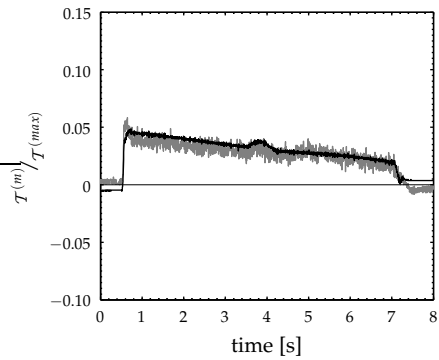
(a) Joint 1.



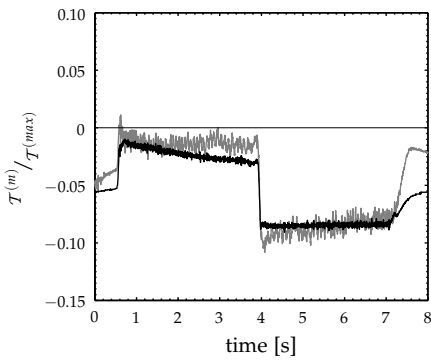
(b) Joint 2.



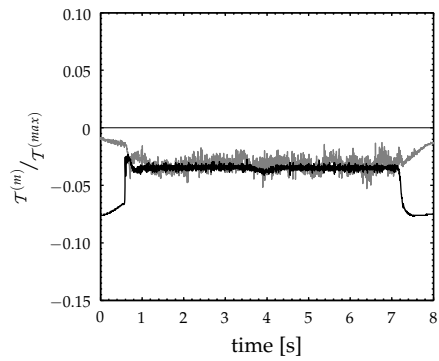
(c) Joint 3.



(d) Joint 4.



(e) Joint 5.



(f) Joint 6.

Figure C.14: The simulated — and measured — joint torques along the corner trajectory at 100 mm/s with $r = 50$ mm as a function of time.

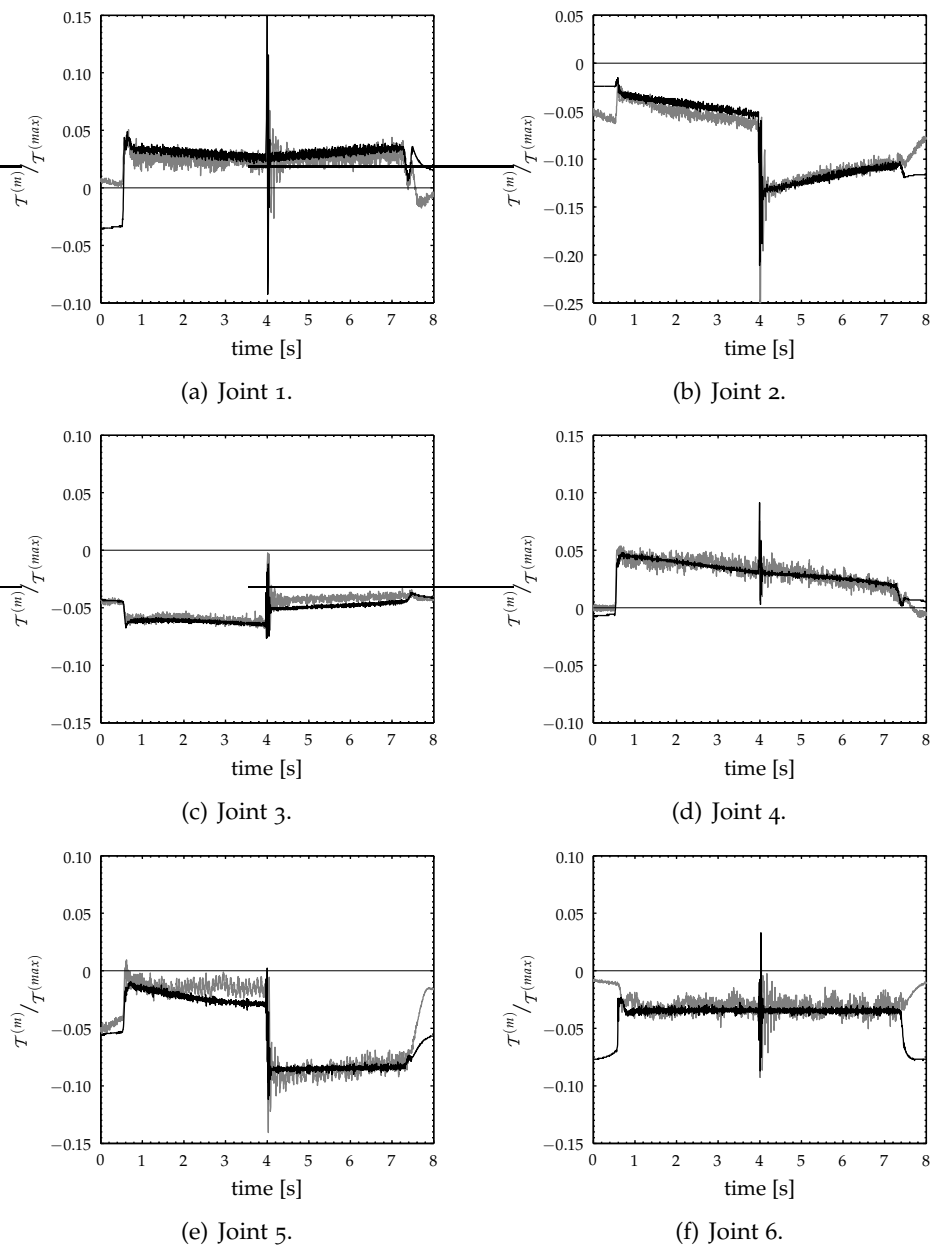


Figure C.15: The simulated — and measured — joint torques along the corner trajectory at 100 mm/s with $r = 2.5$ mm as a function of time.

Publications

- Aarts, R.G.K.M. , Jonker, J.B. , and Waiboer, R.R. (2001). Modelling and efficient dynamic simulation of flexible link manipulators. In Amerongen, J. van, editor, *Proceedings of the 3rd Workshop on European Scientific and Industrial Colaboration*, pages 413–422, Enschede, The Netherlands. University of Twente.
- Aarts, R.G.K.M. , Jonker, J.B. , and Waiboer, R.R. (2006). *Informatics in Control, Automation and Robotics*, chapter Realistic Dynamic Simulation of an Industrial Robot with Joint Friction, pages 187–194. Springer.
- Jonker, J.B. , Aarts, R.G.K.M. , and Waiboer, R.R. (2007). *Multibody Dynamics - Computational Methods and Applications*, volume 4 of *Computational Methods in Applied Sciences*, chapter Modelling of Joint Friction in Robotic Manipulators with Gear Transmissions. Springer.
- Waiboer, R.R. , Aarts, R.G.K.M. , and Jonker, J.B. (2003a). Closed-loop dynamic robot simulation for laser welding. In *Fourth International Conference on Industrial Automation*, Montréal, Canada.
- Waiboer, R.R. , Aarts, R.G.K.M. , and Jonker, J.B. (2003b). Closed-loop dynamic simulation of robotic manipulators with joint friction using a perturbation method. In *ECCOMAS Thematic Conference Multibody 2003 - Advances in Multibody Dynamics*, Lisbon, Portugal.
- Waiboer, R.R. , Aarts, R.G.K.M. , and Jonker, J.B. (2005a). Application of a perturbation method for realistic dynamic simulation of industrial robots. *Multibody System Dynamics*, 13(3):323 – 338.
- Waiboer, R.R. , Aarts, R.G.K.M. , and Jonker, J.B. (2005b). Modelling and identification of a six axes industrial robot. In *ASME International Design Engineering Technical Conferences IDETC/CIE*, pages 1–10 CDROM, Long Beach (CA), USA. ASME.

- Waiboer, R.R. , Aarts, R.G.K.M. , and Jonker, J.B. (2005c). Velocity dependence of joint friction in robotic manipulators with gear transmissions. In *ECCOMAS Thematic Conference Multibody Dynamics 2005, Advances in Computational Multibody Dynamics*, pages 1–19 CDROM, Madrid, Spain.
- Waiboer, R.R. , Vermeij, I. , Aarts, R.G.K.M. , and Jonker, J.B. (2002). Three degree of freedom robot identification for dynamic simulation. In Amerongen, J. van, Jonker, J.B. , Regtien, P.P.L. , and Stramigioli, S. , editors, *Proceedings of the 8th Mechatronics Forum International Conference Mechatronics 2002*, pages 534–543. Drexel Institute for Mechatronics.

Bibliography

- Amontons, G. (1699). De le résistance causée dans les machines. *Mémoires de l'Académie des Sciences*, pages 203–222.
- An, C.H. , Atkeson, C.G. , and Hollerbach, J.M. (1988). *Model-Based Control of Robotic Manipulators*. MIT Press, Cambridge.
- Antonelli, G , Caccavale, F , and Chiacchio, P (1999). A systematic procedure for the identification of dynamic parameters of robot manipulator. *Robotica*, 17(4):427–435.
- Armstrong, B. (1987). On finding exciting trajectories for identification experiments involving systems with non-linear dynamics. In *IEEE International Conference on Robotics and Automation*, pages 1131–1139. IEEE.
- Armstrong-Hélouvry, B. (1991). *Control of Machines with Friction*. Kluwer Academic Publishers.
- Armstrong-Hélouvry, B. , Dupont, P. , and Canudas De Wit, C. (1994). A survey of models, analysis tools and compensation methods for the control of machines with friction. *Automatica*, 30(7):1083–1138.
- Atkeson, C. , An, C. , and Hollerbach, J. (1986). Estimation of inertial parameters of manipulator loads and links. *The International Journal of Robotics Research*, 5(3):101–119.
- Backes, F. (1999). Technology oriented off-line programming for 3D laser machines. *Manufacturing Systems*, 28(2):139–143.
- Bair, S. and Winer, W.O. (1979a). A rheological model for elastohydrodynamic contacts based on primary laboratory data. *ASME Journal of Lubrication Technology*, 101:258–265.

- Bair, S. and Winer, W.O. (1979b). Shear strength measurements of lubricants at high pressure. *ASME Journal of Lubrication Technology*, 101:251–257.
- Bhushan, B. (1999). *Principles and Applications of Tribology*. John Wiley & Sons, New York.
- Bo, L.C. and Pavelescu, D. (1982). The friction–speed relation and its influence on the critical velocity of the stick–slip motion. *Wear*, 82(3):277–289.
- Calafiore, G. and Indri, M. (1998). Experiment design for robot dynamic calibration. In *IEEE International Conference on Robotics and Automation*, pages 3303–3309. IEEE.
- Calafiore, G. , Indri, M. , and Bona, B. (2001). Robot dynamic calibration: Optimal excitation trajectories and experimental parameter estimation. *Journal of Robotic Systems*, 18(2):55–68.
- Canudas De Wit, C. , Olsson, P. , Aström, K. , and Lischinsky, P. (1995). A new model for control of systems with friction. *IEEE Transactions on Automatic Control*, 40(3):419–425.
- Corke, P.I. (1996). *Visual Control of Robots: High-Performance Visual Servoing*. Research Studies Press Ltd., Taunton, Somerset, England.
- Coulomb, C.A. (1785). Théorie des machines simples. *Mémoires de Mathématique et de Physique de l'Académie des Sciences*, pages 161–331.
- Crook, A.W. (1961). The lubrication of rollers II. Film thickness with relation to viscosity and speed. *Philosophical Transactions of the Royal Society of London. Series A, Mathematical and Physical Sciences*, 254(1040):223–236.
- Dahl, P.R. (1968). A solid friction model. Technical Report TOR-158(3107–18), The Aerospace Corporation, El Segundo, CA.
- Dahl, P.R. (1977). Measurement of solid friction parameters of ball bearings. In *Proceedings of the 6th Annual Symposium on Incremental Motion, Control Systems and Devices*, pages 49–60. University of Illinois.
- Dowson, D. (1995). Elastohydrodynamic and micro-elastohydrodynamic lubrication. *Wear*, 190(2):125–138.

- Dowson, D. (1998). *History of Tribology*. Professional Engineering Publishing, London.
- Dowson, D. and Higginson, G.R. (1977). *Elasto-Hydrodynamic Lubrication*. Pergamon Press Ltd., Oxford.
- Evans, C.R. (1983). *Measurement and Mapping of the Rheological Properties of Elastohydrodynamic Lubricants*. PhD thesis, University of Cambridge.
- Gautier, M. (1990). Numerical calculation of the base inertial parameters of robots. In *Proceedings of the 1990 IEEE Conference on Robotics and Automation*, pages 1020–1025, Cincinnati, OH.
- Gautier, M. and Khalil, W. (1988). A direct determination of minimum inertial parameters of robots. In *IEEE Conference on Robotics and Automation*, pages 1682–1687, Philadelphia.
- Gautier, M. and Khalil, W. (1992). Exciting trajectories for the identification of base inertial parameters of robots. *The International Journal of Robotics Research*, 11(4):362–375.
- Geest, J.W. van de (2003). Implementation and validation of joint flexibility in SPACAR and identification on the Stäubli RX90 robot. Master's thesis, University of Twente, Enschede, The Netherlands. Report: WA0895.
- Gelinck, E.R.M. (1999). *Mixed Lubrication of Line Contacts*. PhD thesis, University of Twente, Enschede, The Netherlands.
- Gelinck, E.R.M. and Schipper, D.J. (2000). Calculation of stiction curves for line contacts. *Tribology International*, 33:175–181.
- Geradin, M. , Robert, G. , and Buchet, P. (1986). Kinematic and dynamic analysis of mechanisms, a finite element approach based on Euler parameters. In Bergan, P. G. , Bathe, K. J. , and Wunderlich, W. , editors, *Finite Element Methods for Nonlinear Problems*, pages I.6.1–I.6.20, Berlin. Springer-Verlag.
- Gerat, V. (1994). Speed reducer of the cycloidal type for robots and other industrial manipulators. US Patent 5286235.
- Gerat, V. and Palau, J. (1998). Worm and wheel gear reducer for robot articulation. FR Patent 2752280.

- Golub, G.H. and Loan, C.F. van (1983). *Matrix Computations*. North Oxford Academic Publishers Ltd., Oxford, England.
- Graaf, M.W. de, Aarts, R.G.K.M. , Jonker, J.B. , and Meijer, J. (2006). Real-time trajectory generation for sensor-guided robotic laser welding. In *Submitted to 8th International IFAC Symposium on Robot Control - SYROCO 2006*.
- Greenwood, J.A. and Williamson, J.B.P. (1966). Contact of nominally flat surfaces. *Proceedings of the Royal Society of London. Series A, Mathematical and Physical Sciences*, 295(1442):300–319.
- Grotjahn, M. (2003). *Kompensation Nichtlinearer Dynamischer Effekte Bei Seriellen und Parallelen Robotern Zur Erhöhung der Bahngenauigkeit*. PhD thesis, Universität Hannover.
- Grubin, A.N. and Vinogradova, I.E. (1949). Central scientific research institute for technology & mechanical engineering. Book No. 30 (D.S.I.R Translation No.337).
- Hakvoort, W.B.J. (2004). Identification of inertia and stiffness parameters of the Stäubli RX90 robot. Master's thesis, University of Twente, Enschede, The Netherlands. Report no. WA0920.
- Hakvoort, W.B.J. , Aarts, R.G.K.M. , Dijk, J. van, and Jonker, J.B. (2006). Lifted system iterative learning control applied to an industrial robot. submitted to Control Engineering Practice.
- Hardeman, T. , Aarts, R.G.K.M. , Dijk, J. van, and Jonker, J.B. (2006a). A scanning mirror for robotic laser welding. In Jager, B. de and Meinsma, G. , editors, *Book of Abstracts 25th Benelux Meeting on Systems and Control*, page 143.
- Hardeman, T. , Aarts, R.G.K.M. , and Jonker, J.B. (2006b). A finite element formulation for dynamic parameter identification of robot manipulators. *Multibody System Dynamics*, 16:21–35.
- Hensen, R.H.A. , Molengracht, M.J.G. van de, and Steinbuch, M. (2002). Frequency domain identification of dynamic friction model parameters. *IEEE Transactions on Control Systems Technology*, 10(2):191–195.

- Holterman, W. (2003). Closed loop modelling and validation of the Stäubli RX90 robot. Master's thesis, University of Twente, Enschede, The Netherlands. Report no. WA0898.
- International Iron & Steel Institute (1998). ULSAB: Ultralight steel auto body. <http://www.worldautosteel.org/ulsab/>.
- Jacobson, B. (2003). The stribeck memorial lecture. *Tribology International*, 36:781–789.
- Jonker, J.B. (1988). *A Finite Element Dynamic Analysis of Spatial Mechanisms and Manipulators*. PhD thesis, Delft University of Technology, Delft, The Netherlands.
- Jonker, J.B. (1990). A finite element dynamic analysis of flexible manipulators. *The International Journal of Robotics Research*, 9(4):59–74.
- Jonker, J.B. (2002). *Dynamics of Machines, A Finite Element Approach*. University of Twente, Enschede, The Netherlands.
- Jonker, J.B. and Aarts, R.G.K.M. (1998). Modeling of flexible mechanisms and manipulators for control purposes. In *Proceedings of the Fourth International Conference on Motion and Vibration Control*, pages 291–297, ETH-Zurich. MoViC, Institute of Robotics.
- Jonker, J.B. and Aarts, R.G.K.M. (2001). A perturbation method for dynamic analysis and simulation of flexible manipulators. *Multibody Systems Dynamics*, 6(3):245–266.
- Jonker, J.B. and Aarts, R.G.K.M. (2002). Dynamic simulation of planar flexible link manipulators using adaptive modal integration. *Multibody Systems Dynamics*, 7(1):31–50.
- Jonker, J.B. and Meijaard, J.P. (1990). SPACAR-computer program for dynamic analysis of flexible spatial mechanisms and manipulators. In Schiehlen, W. , editor, *Multibody Systems Handbook*, pages 123–143, Berlin, Germany. Springer-Verlag.
- Khalil, W. and Dombre, E. (2002). *Modeling, Identification and Control of Robots*. Hermes Pelton Science, London.
- Khosla, P. (1989). Categorization of parameters in the dynamic robot model. *IEEE Journal of Robotics and Automation*, 5(3):261–268.

- Khosla, P.K. and Kanade, T. (1985). Parameter identification of robot dynamics. In *Proceedings of the 24th IEEE Conference on Decision and Control*, pages 1754–1760.
- Kollmorgen (2004a). <http://www.motionvillage.com/>.
- Kollmorgen (2004b). *SERCOS IDN Reference Manual*. Kollmorgen.
- Kollmorgen (2004c). *Servostar Installation Manual*. Kollmorgen.
- Kool, A. (2003). Modelling and identification of friction in the Stäubli RX90 robot. Master's thesis, University of Twente, Enschede, The Netherlands. Report no. WA0894.
- Kozlowski, K. (1998). *Modelling and Identification in Robotics*. Springer-Verlag, London.
- Lawson, C.L. and Hanson, R.J. (1974). *Solving Least Squares Problems*. Prentice-Hall, New Jersey.
- Linden, G.W. van der and Weiden, A.J.J. van der (1994). Practical rigid body parameter estimation. In *Proceedings of the 4th IFAC Symposium on Robot Control*, pages 631–636.
- Luh, J.Y.S. , Walker, M.W. , and Paul, R.P.C. (1980). On-line computation scheme for mechanical manipulators. *ASME Journal of Dynamic Systems, Measurement and Control*, 102:69–76.
- Mayeda, H. , Yoshida, K. , and Osuka, K. (1998). Base parameters of manipulator dynamics. In *Proceedings of the IEEE Conference on Robotics and Automation*, pages 1367–1372.
- Mebitec (2006). TopLas3D. Meerbuscher Informationstechnik GmbH, <http://www.mebitec.de>.
- Meijaard, J.P. (1991). Direct determination of periodic solutions of the dynamical equations of flexible mechanisms and manipulators. *Int. Num. Methods in Engineering*, 32:1691–1710.
- Olsen, M.M. and Petersen, H.G. (2001). A new method for estimating parameters of a dynamic robot model. *IEEE Transactions on Robotics and Automation*, 17(1):95–100.

- Olsen, M.M. , Swevers, J. , and Verdonck, W. (2002). Maximum likelihood identification of a dynamic robot model: Implementation issues. *The International Journal of Robotics Research*, 21(2):89–96.
- Olsson, H. , Åström, K.J. , Canudas de Wit, C. , Gäfvert, M. , and Lischinsky, P. (1998). Friction models and friction compensation. *European Journal of Control*, 4(3):176–195.
- Porsche Engineering Services Inc. (1998). ULSAB: Ultralight steel auto body. Technical report, Porsche Engineering Services Inc., <http://www.worldautosteel.org/ulsab/>.
- Ransijn, H.J.C. (2005). Adaptive feed-forward control based on friction identification for the Stäubli RX90 robot. Master's thesis, University of Twente, Enschede, The Netherlands. Report no. WA0990.
- Römer, G.R.B.E. (2002). *Hoogvermogen Lasers Voor Het Bewerken Van Metalen*. Vereniging FME-CWM.
- Roo, S. de (2003). Testing the trajectory performance of the Stäubli RX90 robot for laser welding. Master's thesis, University of Twente, Enschede, The Netherlands. Report no. WA0889.
- Schipper, D.J. (1988). *Transitions in the Lubrication of Concentrated Contacts*. PhD thesis, University of Twente, Enschede, The Netherlands.
- SERCOS (1998). Sercos interface. <http://www.sercos.org>. European standard EN 61491.
- Sheu, S.Y. and Walker, M.W. (1991). Identifying the independent inertial parameter space of robot manipulators. *The International Journal of Robotics Research*, 10(6):668–680.
- Shome, S.S. , Beale, D.G. , and Wang, D. (1998). A general method for estimating dynamic parameters of spatial mechanisms. *Nonlinear Dynamics*, 16:349–368.
- Spikes, H.A. (1999). Thin films in elastohydrodynamic lubrication: The contribution of experiment. *Proceedings of the Institution of Mechanical Engineers - J*, 213(5):335–352.
- Spikes, H. (2001). Tribology research in the twenty-first century. *Tribology International*, 34(12):789–799.

- Stribeck, R (1902). Die wesentlichen eigenschaften der gleit- und rollenlager. *Zeitschrift Des Vereines Deutcher Ingenieure*, 46(38, 39):1342–1348,1432–1437.
- Su, Y (2000). Laser welding of stainless steels. Technical report, Netherlands Institute for Metals Research.
- Swevers, J. , Al Bender, F. , Ganseman, C.G. , and Prajogo, T. (2000). Integrated friction model structure with improved presliding behavior for accurate friction compensation. *IEEE Transactions on Automatic Control*, 45(4):675–686.
- Swevers, J. , Ganseman, C. , Schutter, J. de, and Brussel, H. van (1996). Experimental robot identification using optimised periodic trajectories. *Mechanical Systems and Signal Processing*, 10(5):561–577.
- Swevers, J. , Ganseman, C. , Tükel, D.B. , Schutter, J. de, and Brussel, H. van (1997). Optimal robot excitation and identification. *IEEE Transactions on Robotics and Automation*, 13(5):730–740.
- MATLAB (2004). *MATLAB Manual*. The MathWorks, Natick (MA), 5th edition.
- SIMULINK (2004). *SIMULINK Manual*. The MathWorks, Natick (MA), 5th edition.
- Vermeij, I. (2001). Modelling and identification of the Stäubli RX90 robot: Two and three degree of freedom models. Master's thesis, University of Twente, Enschede, The Netherlands. Report no. WA0806.
- Waiboer, R.R. (1999). A superposition method for the dynamic analysis and simulation of flexible mechanisms and manipulators. Master's thesis, University of Twente.
- Waiboer, R.R. (2000). Inventory of off-line programming software for laser welding. Technical Report P.00.8.043, Netherlands Institute for Metals Research, Delft, The Netherlands.
- Werff, K. van der and Jonker, J.B. (1984). Dynamics of flexible mechanisms. In Haug, E.J. , editor, *Computer Aided Analysis and Optimization of Mechanical System Dynamics*, pages 381–400, Berlin, Germany. Springer-Verlag.
- WindRiver (2004). <http://www.windriver.com/>.

Summary

Robotised laser welding is an innovative joining technique which is increasingly finding applications, especially in the automotive industry. In order to reduce the time needed to prepare and program the laser welding robot, off-line programming systems are used. The off-line programming systems currently available only allow kinematic simulations of the robot motion, which are insufficient for a proper *a priori* prediction of the ability to weld the seam as dynamic effects in the path tracking accuracy are not taken into account. Combining off-line programming systems and dynamic simulations of the robot motion makes it possible to predict the path tracking errors in advance.

Dynamic simulations require accurate robot models. Furthermore, it is desirable that the simulation is sufficiently time efficient to make the off-line programming process effective and fast. This thesis discusses the dynamic modelling, identification and simulation of a Stäubli RX90B industrial robot to be used for off-line programming for robotised laser welding.

In this thesis, a finite element formulation has been used for the modelling of the robot arm. The model is extended with models of the robot controller and the driving system, including joint friction caused by bearings and gears. At first, phenomenological friction models from the robotics literature were applied. These models included simple Coulomb and viscous friction descriptions. Measurements have pointed out, however, that these models are insufficient to describe the friction behaviour of the robot at the required level of accuracy.

Therefore, a new friction model has been formulated that relies on insights from sophisticated tribological models. The friction model accurately describes the friction behaviour in the full velocity range with a minimal and physically sound parametrisation. The model has been ex-

tended in such a way that it is able to predict the joint friction behaviour in the pre-sliding regime during reversals of the joint velocity.

Accurate robot models require model parameters that are known with sufficient accuracy. The model parameters have been found either from information supplied by the manufacturer or by means of identification techniques. For the modelling and identification of the robot controller the information of the manufacturer has been used. The model parameters associated with the inertia properties of the robot arm, the parameters of the gravity compensating spring, the motor inertias and the friction parameters have been found by means of experimental parameter identification.

Using linear least squares estimation techniques the unknown model parameters have been acquired. The problem of parameter identifiability in the presence of unmodelled dynamics and disturbances has been solved using singular value decomposition. Furthermore, scaling techniques have been applied in a way so that all parameters are estimated with the same relative accuracy.

The robot model has been validated by means of closed-loop dynamic simulations. The simulated path tracking errors correspond well with the measured path tracking errors. Furthermore, the measured joint torques correspond with the simulated joint torques. In order to reduce the amount of time needed for the dynamic simulations, a perturbation method has been applied. In this perturbation method, deviations from the nominal motion due to joint friction and limitations of the control system are modelled as first-order perturbations of the nominal motion.

The application of dynamic simulations in off-line programming has been demonstrated by means of three typical welding trajectories. It has been shown that it is possible to *a priori* detect path tracking errors and to identify trajectory configurations that are too demanding for the robot.

Samenvatting

Gerobotiseerd laserlassen is een innovatieve verbindingstechniek die, met name in de automobieliindustrie, steeds vaker wordt toegepast. Om de omstel- en programmeertijden te verkorten en om op voorhand te kunnen bepalen of een bepaald product met laser gelast kan worden, wordt er gebruik gemaakt van off-line programmeersystemen. Bestaande systemen omvatten slechts het kinematisch simuleren van een robotbeweging hetgeen onvoldoende is om een goede voorspelling te doen over de laser lasbaarheid. Het toevoegen van een dynamische simulatie van de robotbeweging maakt het mogelijk om lasnaad-volgfouten op voorhand te voorspellen. Het proces van het modelleren, identificeren en simuleren van een Stäubli RX90B industriële robot ten bate van het off-line programmeren voor gerobotiseerd laserlassen is in dit proefschrift beschreven.

Dynamische simulaties vereisen een nauwkeurig robotmodel. Ook is het van belang dat de simulatietijd voldoende kort is. Om dit te realiseren is gebruik gemaakt van een eindige elementen modelleermethode om de robotarm mee te modelleren. Dit model is verder uitgebreid met modellen van de regelaar en van de aandrijving, inclusief wrijving van de robotassen.

De lagers en de tandwieloverbrengingen in het aandrijfsysteem van de robot veroorzaken wrijving. In eerste instantie zijn wrijvingsmodellen uit de robotliteratuur gebruikt welke gebaseerd zijn op wrijvingsfenomenen, zoals Coulombse en viskeuzewrijving. Metingen hebben echter uitgewezen dat deze wrijvingsmodellen het werkelijke wrijvingsgedrag van de robot onvoldoende nauwkeurig beschrijven. Aangezien wrijving een significante bijdrage levert aan de asmomenten tijdens het bewegen, is een verbeterd wrijvingsmodel noodzakelijk.

Op basis van inzichten vanuit de tribologieliteratuur is een nieuw wrijvingsmodel ontwikkeld dat de wrijving in het volledige snelheidsregime beschrijft met een minimaal aantal modelparameters. Met dit

wrijvingsmodel is een consistente schatting van de modelparameters mogelijk. Het wrijvingsmodel is vervolgens uitgebreid met een beschrijving die ook het gedrag beschrijft tijdens het omkeren van de bewegingsrichting van de robotas.

Voor een nauwkeurig robotmodel is het noodzakelijk dat de modelparameters met hoge precisie bekend zijn. Deze kunnen op een tweetal manieren bekend zijn; enerzijds vanuit het ontwerp van de fabrikant van de robot en anderzijds door middel van parameteridentificatie. De modelstructuur en de modelparameters voor het model van de regelaar zijn verkregen vanuit informatie van de fabrikant Stäubli. De modelparameters gerelateerd aan de inertiaeigenschappen van de robotarm, de zwaartekracht compensatieveer, de rotortraagheden en de wrijvingsparameters zijn verkregen door middel van experimentele parameteridentificatie.

De parameteridentificatie is uitgevoerd met behulp van een lineaire kleinste kwadratenmethode. Het probleem van parameter identificeerbaarheid onder invloed van niet-gemodelleerde dynamica en andere verstoringen is opgelost door gebruik te maken van een singuliere waarden decompositie. Verder is het noodzakelijk om het lineaire kleinste kwadraten probleem te schalen opdat alle parameters met een gelijke relatieve nauwkeurigheid worden geschat.

Het robotmodel is gevalideerd aan de hand van gesloten-lus simulaties. De gesimuleerde lasnaad volgfouten komen goed overeen met de op de robot gemeten volgfouten. Ook de gesimuleerde motorkoppels laten grote gelijkheid zien met de metingen. Om de simulatietijd te verkorten is een perturbatiemethode toegepast. Hierin worden de nominale, niet-lineaire, beweging en de kleine variaties op de beweging als gevolg van verstoringen apart uitgerekend. De variaties worden berekend door middel van gelineariseerde bewegingsvergelijkingen wat een factor tien aan reductie van de simulatietijd oplevert.

Simulaties van typische trajecten die voorkomen tijdens het laserlassen geven aan dat het op voorhand bepalen van de lasbaarheid via off-line programmeren in combinatie met dynamische simulaties zeer goed haalbaar is.